Valgus Fatigue and Damage Accretion of the Anterior Bundle of the Ulnar Collateral Ligament: a Finite Element Evaluation

by

David Bernard Jordan

BSME, Louisiana State University, 2016

MS, University of Pittsburgh, 2018

Submitted to the Graduate Faculty of the

Swanson School of Engineering in partial fulfillment

of the requirements for the degree of

Doctor of Philosophy

University of Pittsburgh

2021

UNIVERSITY OF PITTSBURGH

SWANSON SCHOOL OF ENGINEERING

This dissertation was presented

by

David Bernard Jordan

It was defended on

March 4, 2021

and approved by

Dr. Anne Robertson, PhD, Professor, Mechanical Engineering & Materials Science

Dr. Patrick Smolinski, PhD, Associate Professor, Mechanical Engineering & Materials Science

Dr. Steven Abramowitch, PhD, Associate Professor, Bioengineering

Dissertation Director: Dr. Mark Miller, PhD, Mechanical Engineering & Materials Science

Valgus Fatigue and Damage Accretion of the Anterior Bundle of the Ulnar Collateral Ligament: a Finite Element Evaluation

David Bernard Jordan, PhD

University of Pittsburgh, 2021

The pitching of a baseball is a strenuous action that applies exaggerated kinematic and kinetic influences at the elbow of the athlete. The repeated application of these influences can gradually degrade the mechanical integrity of the native biological support structures over time and eventually lead to failure by fatigue. One such structure is the anterior bundle of the ulnar collateral ligament (AMCL).

The fatigue properties of a material are often characterized by its respective fatigue life, where the amount of repetitive loading possible for a given load state before failure is defined. It is also important to predict how the damage is progressing throughout the material for cycles which are less than the predicted failure life. This study seeks to determine these properties of fatigue for the elbow AMCL and implement them into the execution of a Finite Element (FE) simulation for the purpose of predicting the magnitude and location of damage to the AMCL, per magnitude of pitching action performed. For applicability to the general pitching athlete, these results will be formulated using a non-dimensional material model.

Twenty-two cadaveric elbow specimens were used for this study. Eleven were tested in vertical elongation to make measurement of the AMCL elastic mechanical properties and subsequently tested to failure. Eleven contralateral specimens were tested in valgus fatigue to make measurement of the AMCL fatigue properties. These results were incorporated into a transversely isotropic hyperelastic constitutive equation and used to define the material properties

of a 3D elbow model within a FE environment. Simulated displacements mimicking pitching-induced joint opening were applied and both the stress and strain outputs were analyzed.

The average tensile failure load was $595.25\ \text{N} \pm 201.93\ \text{N}$. For specimens tested at 90% and 80% of their estimated one-cycle failure moment, the average cycles to failure were 3211 ± 4721.33 and 25063 ± 30487.58, respectively. The middle band of the AMCL increased in maximum stretch by an average margin of $0.89\% \pm 1.46\%$, with an average failure stretch of 1.077 ± 0.019. The FE fatigue simulation utilizing the nonlinear damage accretion function produced fatigue-induced stretch increase results that agreed with experimental observation to within 1%.

Table of Contents

List of Tables

List of Figures

Preface

A special thanks is given to everyone at the Biomechanics Laboratory at Allegheny General Hospital who contributed to the completion of this work. This includes Dr. Alexander Kharlamov, Patrick Schimoler, Dr. Mark Miller; any orthopedic residents; and any/all PITT students and graduate students. Special recognition is also given to the various senior design students at PITT who designed and built the necessary fixtures and testing devices. Without these individuals, this work would not have been possible.

I also give special thanks to my committee members and advisor for their cooperation and guidance. The technical and research knowledge that I learned in their respective courses and throughout this process was invaluable and greatly appreciated.

I also want to give a special thanks to the PITT STRIVE community. It was the graciousness of Dr. Wosu and Mrs. Sussan Olaore that allowed me the opportunity to pursue a PhD and it was the camaraderie of my peers which provided motivation and support.

I would like to thank my family who supported my move from Louisiana to Pittsburgh. Their well wishes and love throughout this five-year journey made the separation that much easier.

Finally, I would like to dedicate this dissertation to my late Father, Mr. Lynn Bernard Jordan.

1.0 Introduction

In sporting activities, a particular action is often repeated several times in succession. In baseball, a commonly repeated action is a pitch, which can be executed in excess of one-hundred times per game by a single pitcher. Each pitch applies forces and moments to the upper extremity. One particular region, the elbow, is held together by a complex of ligaments. On the medial, or inside of the arm, the joint is supported by the ulnar collateral ligament. The anterior, or uppermost, bundle of the ulnar collateral ligament (AMCL) plays a primary role in resisting the valgus torques applied to the elbow during every pitch. The repeated application of this loading can gradually degrade the mechanical properties of the ligament, and eventually cause failure by fatigue.

In mechanics, fatigue failure is especially hazardous because it can occur at loads which are typically less than the ultimate failure load of the material. The accumulation of fatigue effects is thought to be one of the many contributors that can lead to ligament failure. Mitigation of ligament fatigue failure can possibly be achieved through the development of a predictive model that can be used to assess how the degradation is progressing throughout the ligament per level of pitching action performed. In the study of material behavior, one such tool is known as a pseudo-elastic constitutive damage model. These models are phenomenologically formulated to represent the load-deformation response of a particular body. The pseudo-elastic extension arises from the use of several parameters that act to degrade the mechanical response of the material as the body undergoes a prescribed loading condition. Several damage models have been formulated for different biological tissues.

In this study, we seek to propose a fatigue-damage model for the elbow AMCL. The model will be phenomenologically developed from experimental data taken from vertical elongation and valgus fatigue loading tests. The model will use the principles of continuum mechanics to construct the stress-deformation constitutive response of the ligament. The damage accretion in the ligament will be determined using the principles of continuum damage mechanics. Because the model will be developed under valgus rotational loads, it has particular applicability to the pitching of a baseball. All of these factors will be taken into account within the model and implemented into a finite element simulation.

The goal of the study is to present a computational model that can predict the fatigue life of the AMCL corresponding to a given level of pitching, how much fatigue damage the AMCL might sustain per number of pitches thrown, where the greatest fatigue damage will amass and how the distribution of the fatigue damage will relate to the observed experimental failure characteristics.

1.1 Modeling Significance

The constitutive modeling of biological structures is a broad topic with wide ranging applicability to a variety of tissue types and loading scenarios. These models provide a means to estimate the given mechanical response of a biological structure without any need for further physical testing. This is especially convenient for those models which are derived for very specific tissues, subjected to very specific loadings. It is almost invaluable for those models that extend toward more general circumstances. The presentation of the proposed fatigue model of this paper will add to this knowledge.

1.2 Clinical and Athletic Significance

The modeling and simulation of the elbow AMCL fatigue behavior will contribute to the clinical understanding of the ligament. Having an estimate of the number of pitches necessary to damage the ligament can inform athletic coaching decisions. Knowing the level of predicted damage to the ligament, based on the knowledge of pitches thrown, can possibly inform rehabilitation exercises for athletes who experience pain but no rupture. For ligaments that have ruptured, having estimates of the nature of the rupture could inform pre and post-operative decisions. The information added to these respective areas could improve overall athletic performance and clinical treatment.

2.0 Background

The elbow is vital to daily human activity. These activities include both athletic and non-athletic endeavors. In the athletic realm, nearly every sport requires the use of a fully functional elbow to execute the demands of the respective activity. The biological constructs of the elbow which allow this execution are assembled in an intricate fashion which will be described below.

2.1 Anatomy

2.1.1 Bone Structure

There are three bones at the elbow joint. These are the humerus, the radius and the ulna (Figure 1). With the terms distal and proximal referring to the terminal locations of the bones with respect to the head of the body, the distal humerus is comprised of the trochlea and the capitellum. The radial head of the proximal radius moves along the capitellum. The trochlear notch of the ulna moves along the trochlea. The radial notch of the ulna supports the radial head, as they are constrained to move together.

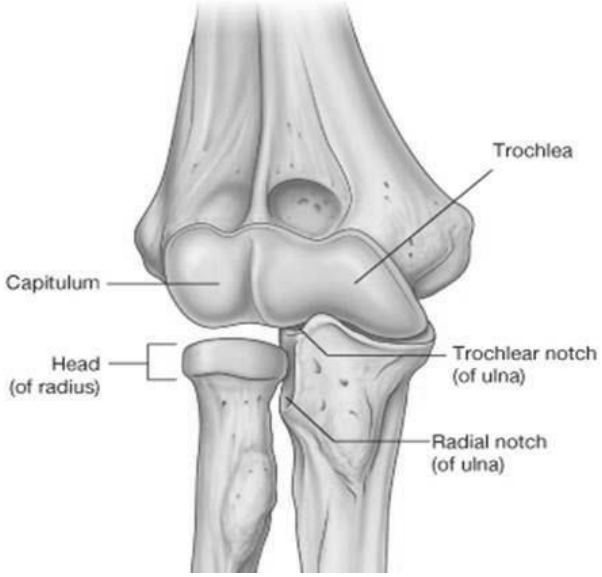

Figure 1: Bone Structure of the Elbow Joint [boneandspine.co.com]

2.1.2 Ligaments

The elbow joint is stabilized by two main ligament constructs. On the outside (lateral) of the elbow, this is the lateral collateral ligament (LCL). On the inside (medial) of the elbow, this is the ulnar collateral ligament (UCL). These ligaments are composed of triple helix chains of collagen molecules, called tropocollagen, which assemble together to form collagen fibrils[1, 2] and elastin fibrils. The collagen fibrils further assemble to form larger diameter collagen fibers (Figure 2) which are embedded in a ground substance of water and proteoglycans[3, 4]. Mechanically, the collagen fibers are the primary load bearing structures of the ligament in tension and the elastin contributes substantially in shear and transverse tensile loading[5]. Previous studies have been performed which document the strength of collagen fibers[6] in tension.

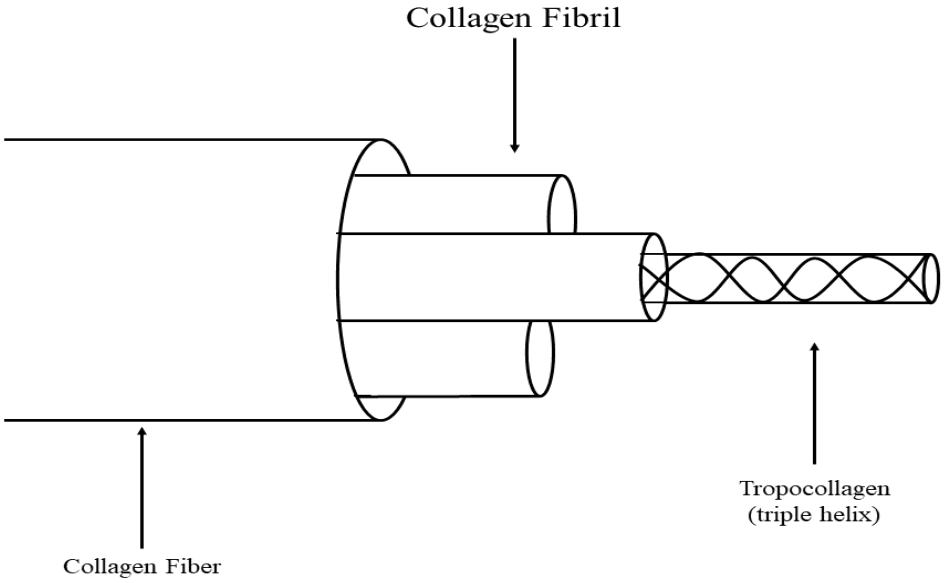

Figure 2: Collagen Fiber Structure

The UCL has its origin and insertion points at the far end (distal) humerus and near end (proximal) ulna, respectively. The ligament consists of three bundles. These are the posterior bundle, transverse bundle and anterior bundle (Figure 3). Each bundle plays a respective role in maintaining the structural stability of the elbow joint.

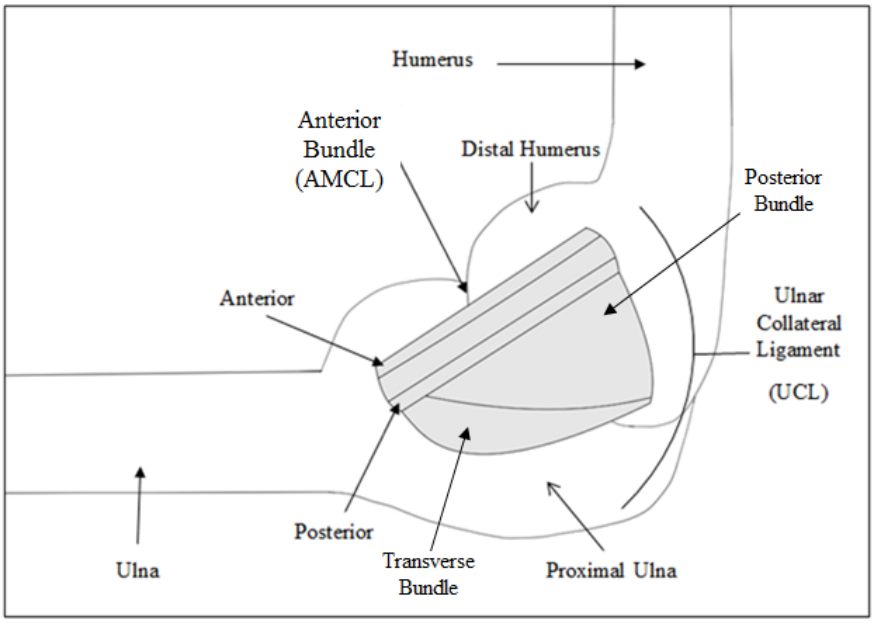

Figure 3: Ulnar Collateral Ligament Complex at the Medial Elbow

2.2 Overhand Throwing (Baseball Pitching)

The action of overhand throwing occurs in a variety of athletics. In these sports, the overhand throwing motion must be executed many times. This is especially true for baseball pitchers, where upwards of one hundred pitches per game may be executed. This section provides a breakdown of the fundamentals of baseball pitching and the perceived implications.

2.2.1 Mechanics

The complete pitching motion is comprised of a series of phases that all occur within the time frame of milliseconds to achieve the goal of launching a baseball. Six phases have been

identified and described by several authors[7, 8]. These phases are the wind-up, stride, arm cocking, arm acceleration, arm deceleration and follow-through.

The wind-up phase begins with a shift in body weight into a prepared stance, followed by a rotation of the torso and a static, flexed elbow[8, 9]. The wind-up is followed by the stride phase where velocity in the targeted direction is generated.

The arm cocking phase follows the stride phase and is denoted by extreme rotation of the elbow and shoulder, which can generate high magnitudes of torque. The mean maximum inward (varus)/outward (valgus) torque at the elbow has been measured to be as high as 120 Nm[10]. Arm acceleration follows arm cocking, where the elbow is internally rotated from a position of maximum flexion, to a position of full extension at rotational rates as high as 2600 deg/sec[11]. These magnitudes are extreme and the consistent measurement of these peak kinematics have been shown to vary in relation to ball speed and various upper kinematic variables[12].

Arm deceleration follows arm acceleration and is initiated by the release of the ball. The mean minimum elbow flexion during this phase has been measured to be 24°[13]. The follow-through phase succeeds the deceleration of the arm and is identified by the continued deceleration of the throwing arm and trunk[8]. The completion of the follow-through marks the end of the completed pitching motion.

2.2.2 Affecting Parameters

The motion described in the previous section is the fundamental pitching action. This layout applies to the general pitcher, regardless of age, experience or competition level. However, other factors can influence the kinematics observed throughout the pitching cycle.

The factor of age has been studied in relation to a variety of pitching variables. Older pitchers have been shown to have higher external elbow rotation and greater elbow flexion during the early and late cocking phases[14]. Studies in youth pitchers have shown that lower reduced rotation can result from proper execution of pitching mechanics[15].

The effect of pitch type has also been studied. Intuitively it seems reasonable that different pitch types should generate different effects on the upper extremity. This was quantitatively shown in youth pitchers where fastballs and curveballs were shown to produce the highest elbow torque and arm speed, respectively[16]. The investigation of these parameters show that the kinematic and dynamic effects developed throughout the pitching motion, at the upper extremity, can be affected by both the mechanics and biology of the performing athlete.

2.2.3 Valgus Stress

Near the end of the arm cocking phase, the centroidal ulnar axis rotates laterally with respect to the centroidal humeral axis. This motion is known as a valgus rotation and creates a valgus rotation angle θ, between the two axes (Figure 4).

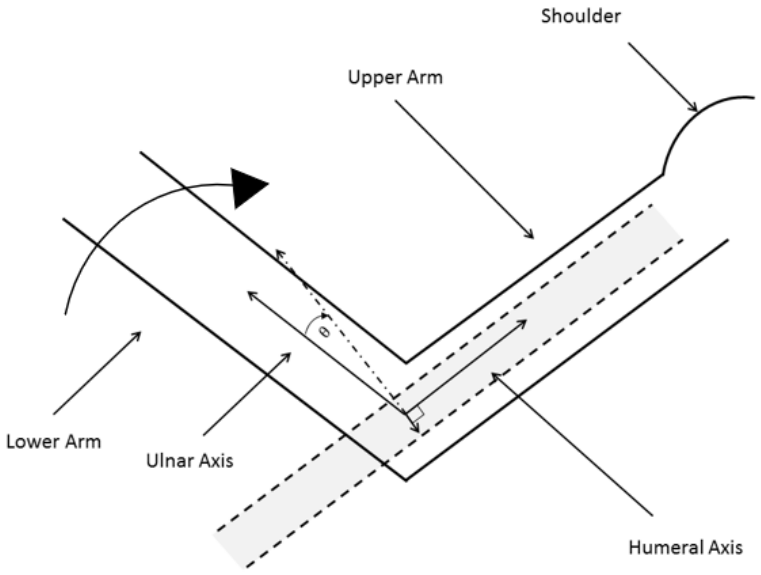

Figure 4: Valgus Elbow Motion

The valgus load is generated by both muscular and non-muscular torque effects, with the torque from the internal rotation of the shoulder being the primary influencer[17]. A natural gap exists between the ulna and the humerus. This opening is referred to as the ulnohumeral joint space. Increases in the magnitude of this spacing have been reported to occur in successive repetitions of twenty pitches[18]. The ulnar collateral ligament at the medial elbow is susceptible to the highest brunt of these valgus effects, especially with the anterior bundle being the primary valgus support structure[19].

2.3 Clinical Implications

The presence of this valgus load at the elbow creates a potentially hazardous situation. It is not only the magnitude of the valgus loads, but the repeated application, which presents potential

damaging effects at the UCL complex. The implications of these effects can impact the required performance of the athlete and the rehabilitation/repair responsibilities of the physician/clinician.

2.3.1 UCL Rupture

Because baseball pitching requires successive repetition, the ligaments that support the elbow, especially the UCL are at risk of injury by fatigue. Performance of a high number of pitches throughout a season can cause elbow pain in the athlete[20]. The incidence of pain can be a result of different factors. In the worst case, it could be the indicator of significant ligament injury.

Depending on the level of performance, pitchers can throw between 60-100, or more, per game. This is directly correlated to the dominant risk factors for injury, which include pitches per game and innings pitched, citing repetitive pitching as the primary cause for the majority of elbow injuries[21]. In addition, radiographic studies have shown that pitchers can develop degenerative changes in the elbow of their pitching arm, such as radial head osteophytes, as a result of these repetitive actions[22].

2.3.2 Repair and Rehabilitation

Ruptures of the UCL are commonly treated with one of two techniques, although others exist. These techniques are either reconstruction with the docking method or repair with internal bracing. Reconstruction with the docking technique (Figure 5) involves creation of an ulnar tunnel through the sublime tubercle through which a graft is passed while the opposite end is docked into holes drilled at the medial epicondyle using sutures[23, 24]. Repair with internal bracing involves

fixing suture tape to the torn ligament which is held together at two ends by threaded anchors set into two tapped holes drilled in the ulna and humerus[25, 26].

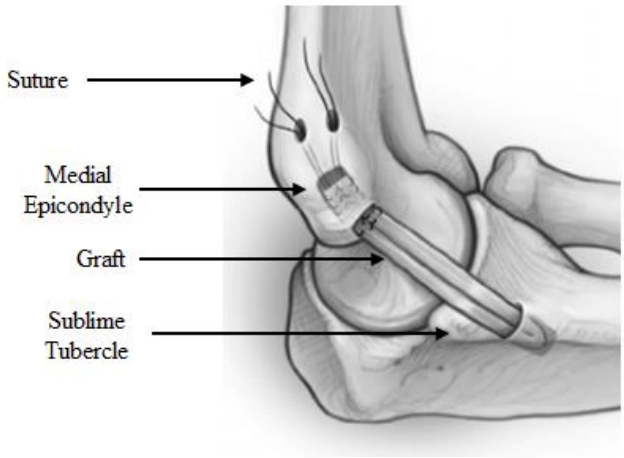

Figure 5: UCL Repair (Docking Technique) [researchgate.com]

In a survey posed to the members of the ASES (American Shoulder and Elbow Surgeons), 66% of surgeons cited the docking technique as the preferred reconstruction method for cases where surgery was deemed appropriate[27]. Although reconstruction is the preferred surgical option, studies have shown that repair can be just as viable. In a study on valgus fatigue, the repaired elbow with internal bracing was shown to have less gap formation between the ulna and humerus[28]. At 90º of elbow flexion, load to failure, gapping and valgus opening angle were shown to be similar for reconstruction, repair and the native ligament[25, 26]. A systematic review on the biomechanical outcomes of patients who underwent UCL repair showed that performance return rates were comparable to those for reconstruction[29]. These studies show that UCL reconstruction and UCL repair can both be viable options for surgical treatment of the torn UCL.

After surgical treatment, the concern shifts to the time required for the athlete to return to competition. For athletes who undergo UCL reconstruction, the return rate can depend on the type

of graft used, the tear type and the tear location[30]. In a retrospective study involving 942 patients, surveys showed an average of 4.4 months was needed to initiate throwing after reconstruction[31]. In adolescent pitchers (less than 19 years old), an average of 11.6 months was needed for a complete return to sport after reconstruction[32]. This time is critical for the youth pitcher who may be aspiring for collegiate entry through athletic performance. For pitchers in the MLB, an average of 20.5 months was required for return after reconstruction, with an average subsequent career length of 3.9 years[33]. Once the athlete is able to return to competition, the pitching performance has been observed to decrease, with respect to earned run average and fast ball velocity, in the first year and then gradually improve in the following years[34].

These studies show that the issue of UCL damage is of high concern when considering how many athletes suffer from it, how long they could be out of action and the degree to which their respective post-performance levels may be impaired. For amateur pitchers, an injury sustained to the UCL can significantly hinder potential prospects for collegiate or professional careers. For professional pitchers, the injury presents a huge financial burden for the athlete, where average MLB pitcher contracts can be on the order of millions of dollars. Given these considerations, it is evident that the concern of damage to the UCL is a substantial problem.

3.0 Relevant Literature

The elbow joint undergoes a variety of motions. When considering athletics, some of these motions can be super-physiological, exceeding the normal performance of the elbow in regard to the degree of motion and magnitude of loading. The repeated application of such motions of the extremities can be potentially damaging to the ligaments which support the joints. Because ligaments are surrounded by layers of muscle and other supportive tissue, which help to support the load, the ligaments are not subjected to the full magnitude of the loading. However, the loading magnitudes that the ligaments do experience can gradually wear down the mechanical strength of the ligament in a mechanical process known as fatigue.

3.1 Fatigue of Biological Tissue

3.1.1 Anterior Cruciate Ligament

The effects of fatigue loading have been studied for a variety of ligaments. Because the constituents of ligaments located at different joints in the body are roughly similar, analogous inferences about the UCL can be made from observations of the behavior of other ligaments. One such ligament is the anterior cruciate ligament (ACL) of the knee[35]. The ACL connects the femur to the tibia (Figure 6) and is one of the primary stabilizers of the knee joint.

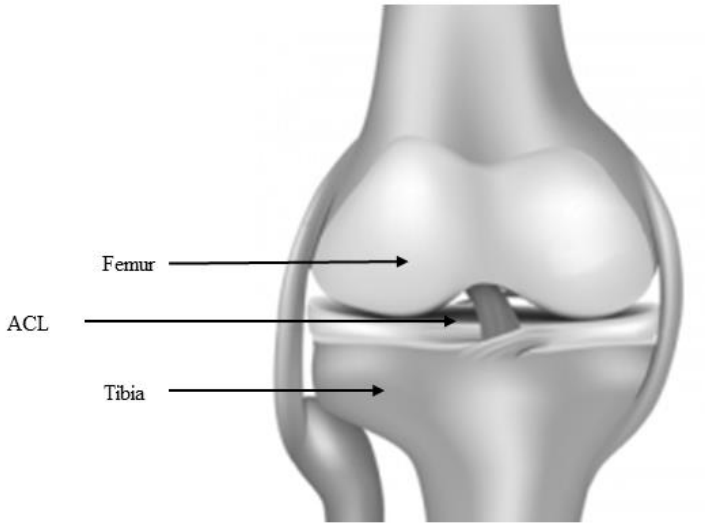

Figure 6: ACL and Knee Joint Bone Structure [stoneclinic.com]

In golfers, the target side knee is repeatedly loaded in adduction and abduction during each golf swing. Similar to pitching, the moments at the knee during the golf swing have been shown to be much higher than the moments associated with normal living activities such as walking[36]. A multibody simulation of the knee, utilizing tracking data taken from actual golfers, produced results suggesting that repeated application of these moments at the knee could be a factor of ACL fatigue failure[37].

Jumps are a common action repeated by athletes in a multitude of sports. It is routinely required by basketball players attempting a shot, track athletes attempting to clear a hurdle and wide receivers leaping for a football reception, among others. When landing, the knee joint involves a pivot in the tibiofemoral joint. In the absence of outside effects, the load maintained by the knee upon landing is some multiple of the individual body weight (BW) of the athlete. In a cadaveric study of knee joints, it was shown that the ACL could fail after an average of 52 cycles at a load of 3BW and 21 cycles for a load of 4BW[38].

These studies show that repetitive application of athletic motions at the knee can lead to ACL fatigue failure. The knee joint is similar to the elbow joint, in that they are both a prime actuator of athletic motion across a wide expanse of sports. With the ACL at such risk of fatigue failure, it is understandable that the UCL would be at similar risk.

3.1.2 Tendons

Tendons are connective tissues composed of collagen fiber bundles that connect muscle to bone. The primary function of a tendon is to move the bone to which it is attached. The bones of the arms and legs are maneuvered in complex ways throughout the routine movements of daily and athletic activity. Because of their usage, it is reasonable to expect tendons to be susceptible to similar effects of fatigue as is observed in ligaments.

Cyclic tensile tests performed on flexor digitorum profundus (FDP) tendons of chicken feet showed that specimens loaded at higher magnitudes for longer periods of time displayed significantly lower strength compared to specimens with either no loading or loading with lesser magnitude and frequency[39]. This observed decrease in strength could be due to a multitude of factors. One such factor could be the formation of defects within the tissue. This has been observed in cyclic stimulation tests performed on FDP tendons of rabbit forearms, where the mean micro-tear area made up approximately 0.8% - 4.5% of the total tendon area and the overall density of tears was greater for loaded tendons than unloaded tendons[40, 41].

The Achilles tendon connects the muscles of the calf to the calcaneus bone of the heel (Figure 7). The tendon is largely responsible for application of the necessary forces to the calf which allow actions like running, jumping and normal ambulation. Because of its function, the Achilles tendon is one of the more commonly injured tendons in the body and the injury has a very

complex etiology[42]. In cyclic tensile testing of the human Achilles tendon, stress-strain load curves were observed to become less steep as the cyclic loading progressed, indicating a reduction in stiffness and increased energy dissipation[43]. This is very hazardous because a tendon with reduced stiffness can suffer greater deformation, increasing the likelihood of eventual failure.

Figure 7: Achilles Tendon and Foot Anatomy [footvitals.com]

These studies performed on the different tendons of human and animal specimens show evidence of an existing problem associated with the cyclic loading that these structures naturally encounter and support.

3.2 Constitutive Modeling

Experimental load-deformation data gathered from biological tissues has been used to develop computational models which can effectively capture the mechanical response. These models are known as phenomenological constitutive models and are derived from hyperelastic strain energy functions. A variety of these strain energy functions have been developed to model

the behavior of numerous biological tissues[44]. The contents of sections 3.2.1 through 3.2.5 give a summary of the fundamental concepts of constitutive modeling as referenced from two textbooks on the subject[45, 46].

3.2.1 Deformation

The deformation of a soft biological tissue is typically given in terms of the stretch. The stretch is obtained through observation of the path taken by a material point, p, from a position $\vec{\mathbf{X}}$, in the reference configuration k_o, to a new position $\vec{\mathbf{x}}$, in the current configuration k. The relationship between the two position vectors is defined through the deformation gradient tensor **F** (Figure 8).

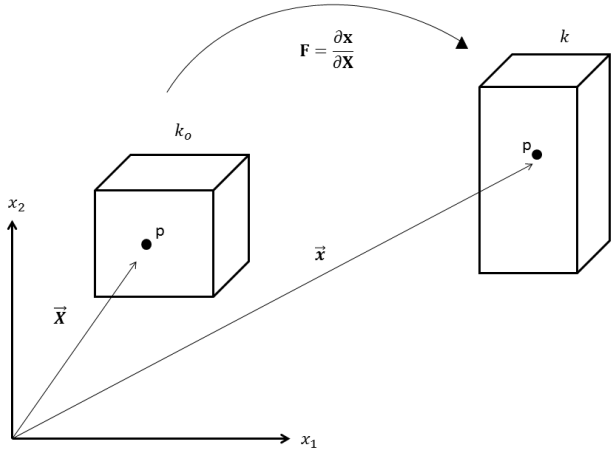

Figure 8: Deformation from Reference Configuration to Current Configuration

The manner in which **F** relates the current configuration to the reference configuration is given by Equation (3-1). Equation (3-1) represents a one-to-one linear mapping from points across

the respective configurations. There are many classical forms of **F** representing well-known 1-D deformation cases, including simple tension with a tensile load $\vec{\mathbf{F}}_{\mathbf{T}}$ (Figure 9a) and pure shear with a shear load $\vec{\mathbf{F}}_{\mathbf{S}}$ (Figure 9b). Two dimensional testing, such as biaxial tension[47], can also be represented. The diagonal components of **F** are the principal stretches. Application of Equation (3-1) for these special deformation cases makes the identification of the stretch variable apparent.

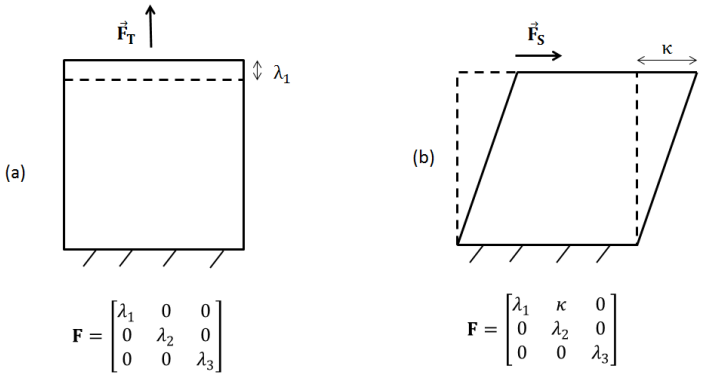

Figure 9: Deformation Gradients for Simple Tension (a) and Pure Shear (b)

The stretches are then taken from the principal components of the right Cauchy-Green stretch tensor **C**, and the left Cauchy-Green stretch tensor **B**, given by Equations (3-2) and (3-3).

$$\mathbf{F} = \frac{\partial \mathbf{x}}{\partial \mathbf{X}} \quad \text{[3-1]}$$

$$\mathbf{C} = \mathbf{F}^{\mathbf{T}}\mathbf{F} \quad \text{[3-2]}$$

$$\mathbf{B} = \mathbf{F}\mathbf{F}^{\mathbf{T}} \quad \text{[3-3]}$$

3.2.2 Hyperelastic Materials

Hyperelastic is a specific classification of materials that are able to undergo large deformations while maintaining their elastic properties. Typical materials that fall into this category are rubbers, various types of polymers and some biological tissues. For these materials, it is assumed that there exists a strain energy density W, which characterizes how strain energy is stored in the material when it is deformed. For agreement with the restrictions of material frame indifference and invariance under superposed rigid body motions, W is often written with a dependence on **C** (Equation 3-4).

$$W=W(\mathbf{C}) \quad \text{[3-4]}$$

3.2.3 Isotropic Incompressible Hyperelastic Materials

Isotropic materials are those for which the material properties remain independent of the direction within the material. Modeling materials of this nature require strain energy densities with similar directional independence. For this purpose, W is often written as a function of the principal strain invariants (Equation 3-5). These invariants (Equations 3-6 - 3-8) have the same value independent of the choice of mutually orthogonal basis vectors.

$$W = W(I_1,I_2,I_3) \quad \text{[3-5]}$$

$$I_1 = \mathrm{tr}(\mathbf{C}) \quad \text{[3-6]}$$

$$I_2 = \frac{1}{2}[\mathrm{tr}(\mathbf{C})^2 - \mathrm{tr}(\mathbf{CC})] \quad [3\text{-}7]$$

$$I_3 = \det(\mathbf{C}) \quad [3\text{-}8]$$

Because these materials are capable of large deformations, they can also undergo large changes in shape. However, this shape change is assumed to occur in such a way that the overall volume of the material remains nearly constant. This condition is termed incompressibility, and it is assumed to hold for this hyperelastic class of materials. This condition is represented through the third strain invariant I_3, or the Jacobian J, which is taken to be equal to one. For this assumption, I_3 is omitted from inclusion in any further formulation.

3.2.4 Anisotropic Hyperelastic Materials

For materials that do have some directional dependence in their mechanical properties, an anisotropic strain energy density is needed to represent the behavior[48]. This directional dependence is typically included with the addition of another strain invariant, I_4. For biological tissues, the anisotropy is represented by the mean preferred fiber direction vector **a**, of any number of fiber families k. I_4 is then given as the tensor product of **C** with the dyadic product of **a** with itself (Equation 3-9).

$$I_4 = \mathbf{C}: \mathbf{a}^{(k)} \otimes \mathbf{a}^{(k)} \quad [3\text{-}9]$$

This additional strain invariant contributes only to the anisotropic portion of W, while the isotropic portion of W maintains a dependence only on I_1 and I_2. An additive decomposition of W is often utilized, given by Equation (3-10).

$$W = W_{\text{isotropic}}(I_1, I_2) + W_{\text{anisotropic}}(I_4) \quad \text{[3-10]}$$

In the literature, $W_{\text{isotropic}}$ is typically taken to represent the strain energy of the matrix and $W_{\text{anisotropic}}$ is taken to represent the strain energy of the fibers. Decoupling of the strain energies of additional constituents such as elastin has also been used[49].

3.2.5 Fiber Dispersion

In many collagenous tissues, not only do the collagen fibers have a mean preferred direction, as discussed in section 3.2.4, but the fibers also display some dispersion about this mean direction. That is, the fibers are not all perfectly aligned. This has been shown for collagen fibers in the major coronary artery of human hearts[50] and in the multiple layers of human aortas[51].

Many contributions have been made on the subject of modeling this fiber dispersion, with most being done on the basis of probability[52]. With respect to a Cartesian system, for a mean preferred fiber direction **a**, the probability of finding a single fiber in that direction is given by the probability density function, $\rho(\mathbf{a})$. Because **a** is a 1-D vector in 3-D space, it can be decomposed into in-plane and out-of-plane components (Figure 10), where the probability of finding a single fiber through searching the entire domain would be 100% (Equation 3-11), where ρ_{ip} and ρ_{op} are the in-plane and out-of-plane probability density functions, respectively[53].

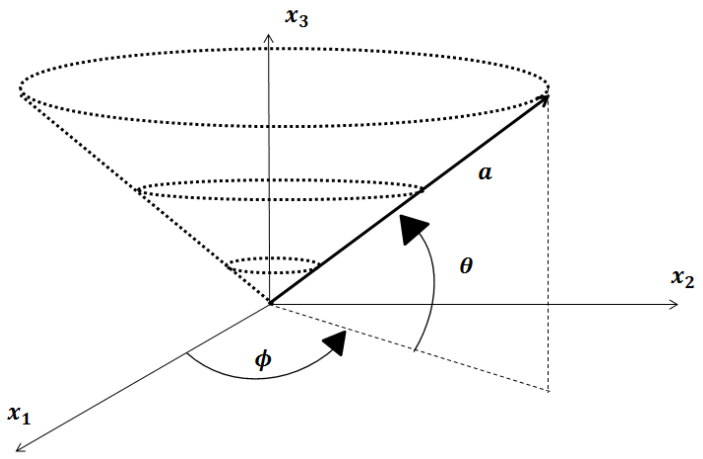

Figure 10: In-Plane and Out-of-Plane Components of the Mean Fiber Direction Vector (a)

$$\frac{1}{4\pi}\int_0^{2\pi}\rho_{ip}(\phi)d\phi\int_{-\frac{\pi}{2}}^{\frac{\pi}{2}}p_{op}(\theta)\cos\theta d\theta = 1 \quad \text{.....[3-11]}$$

The magnitude of the dispersion can be set by assigning a scalar value to ρ_{ip} or ρ_{op} individually. A probability density value of 0 corresponds to no dispersion, while a probability density value of 1 corresponds to isotropic dispersion.

3.2.6 Stress

The first law of thermodynamics is a statement on energy conservation. The second law of thermodynamics states that the entropy for a thermodynamically isolated system must be increasing for all exchanges of energy. In continuum mechanics, this law manifests itself in the form of the Clausius-Duhem inequality, which is a combination of the first and second laws. This principle states that the sum of the entropy generation, internal and external heat generation must

be non-negative (Equation 3-12). where θ is the temperature, s is the specific entropy, e is the specific internal energy, ρ is the density, **σ**:**D** is the stress power and **q** is the heat flux.

$$\rho\dot{s} + \mathrm{div}_x\left[\frac{\mathbf{q}}{\theta}\right] - \frac{1}{\theta}(\rho\dot{e} - \boldsymbol{\sigma}:\mathbf{D} + \mathrm{div}_x\mathbf{q}) \geq 0 \quad \text{[3-12]}$$

Substituting the strain energy density into Equation (3-12) leads to Equation (3-13) where, for a purely mechanical system, i.e. $\{\forall\mathbf{q}, \dot{\theta} = 0\}c$, the relationship between the second Piola-Kirchoff stress **S** and W is determined (Equation 3-14). The Cauchy stress is referenced in the current configuration and is given by Equation (3-15).

$$\boldsymbol{\sigma}:\mathbf{D} - \rho\dot{W} \geq 0 \quad \text{[3-13]}$$

$$\mathbf{S} = 2\frac{\partial W}{\partial \mathbf{C}} \quad \text{[3-14]}$$

$$\boldsymbol{\sigma} = \frac{1}{J}\mathbf{F}\mathbf{S}\mathbf{F}^{\mathbf{T}} \quad \text{[3-15]}$$

3.2.7 Regression and Optimization

With Equation (3-15), and all strain invariants defined in terms of the ligament stretch, a complete representation for the stress in terms of the stretch, **S**(λ) and **σ**(λ), is formed. These formulations may contain a large number of undetermined constants C_i. The values of these constant parameters can be determined using a myriad of regression techniques.

With experimental testing of tissue samples, empirical measurements of stress and stretch can be made against which one can regress the unknown constant parameters. Some commonly used regression methods are linear, polynomial and exponential. Each method can use any number of optimization techniques such as the least squares, Newtonian and Quasi-Newtonian to achieve the best-fit result[54]. The goal of the regression is to minimize the sum of the square of the residuals ε_i, in (Equation 3-16), between the model and empirical stress data.

$$\mathbf{S} = 2\frac{\partial W}{\partial \mathbf{C}} + \varepsilon_i \quad \text{.....[3-16]}$$

The result of the regression leads to a completed model of, $\mathbf{S}(\lambda)$ and $\boldsymbol{\sigma}(\lambda)$, which can be used to represent the mechanical behavior of the material.

3.3 Continuum Damage Mechanics

These hyperelastic models can be modified to include non-recoverable effects, as shown in a field of study known as continuum damage mechanics (CDM). Because the energy input into the material through loading is not all recovered upon unloading, these models are termed pseudo-elastic and the strain energy function is modified to include an effect which accounts for this energy loss. A variety of damage models have been created to model the behavior in engineering materials and soft biological tissues[55].

3.3.1 Stress Softening

Some of the earliest work in modeling stress softening effects was done for engineering materials. In particular, certain classes of rubbers would display softer responses after being loaded to a certain stress level, unloaded and then reloaded to a higher stress level. This phenomenon is known as the Mullins effect (Figure 11).

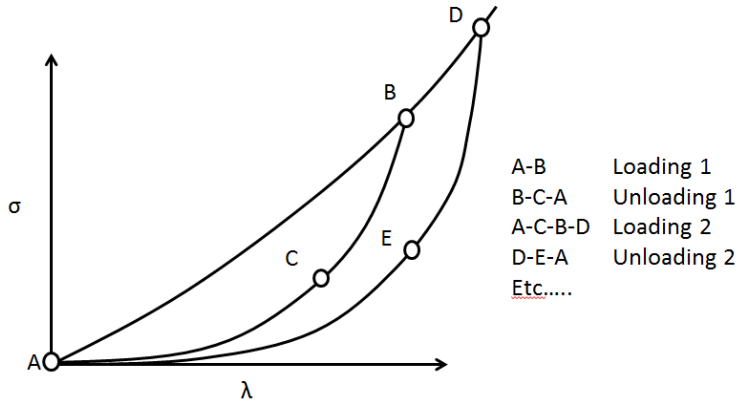

Figure 11: Stress-Stretch Behavior of Material Displaying Mullins Effect

Modeling of this effect was accomplished by introducing a continuous scalar damage parameter η, into the expression for the strain energy density (Equation 3-17), which was made to evolve (Equation 3-18) throughout the course of a prescribed loading cycle and served to lessen the resulting stress response (Equation 3-19)[56], where erf is the error function, r and m are constants, W_m is the strain energy at the point of unloading and $\widetilde{W}(\lambda_1, \lambda_2)$ is the elastic strain energy.

$$W = W(\lambda, \eta) \quad \text{[3-17]}$$

$$\eta = 1 - \frac{1}{r}\mathrm{erf}\left[\frac{1}{m}\left(W_m - \widetilde{W}(\lambda_1, \lambda_2)\right)\right] \quad \text{[3-18]}$$

$$\sigma_{11} = \lambda\eta\mu(\lambda - \lambda^{-3}) \quad \text{[3-19]}$$

Equation (3-19) gives the stress in the primary loading direction for a Neo-Hookean material loaded in simple tension. From this equation, it can be seen that, with $0 \leq \eta \leq 1$, the stress will always be less than or equal to the elastic stress, i.e. $\eta = 1$. It can also be seen that the damage parameter is a function of the strain energy and the choice of how it evolves is chosen subject to a few key constraints. Modifications to this theory have been incorporated for the specifics of the Mullins effect that can account for changes in material symmetry[57] and permanent set[58]. The topic of permanent set is addressed in later sections.

The inclusion of a scalar damage parameter has become a frequent means by which to model the softening effect in many materials. In anisotropic models of fibrous tissues, the damage can be modeled separately between not only the matrix (ground substance) and the fibers, but also between the individual fiber families themselves. The strain energy densities of this form (Equation 3-20) have been termed uncoupled directional damage models[59], where $\mathbf{M} = \mathbf{m}_o \otimes \mathbf{m}_o$ and $\mathbf{N} = \mathbf{n}_o \otimes \mathbf{n}_o$ are the dyadic products of the two unit vectors in the two fiber directions, D_m and D_f are the damage parameters for the matrix and fibers, W_{vol} is the volumetric strain energy density, $\hat{\mathbf{C}}$ is the isochoric left Cauchy-Green stretch tensor and W_o^m and $W_o^{f_i}$ are the elastic strain energy densities for the matrix and fibers.

$$W(\mathbf{C}, \mathbf{M}, \mathbf{N}, D_m D_f) = W_{vol}(J) + (1 - D_m)W_o^m(\hat{\mathbf{C}}) + \sum_{i=1,2}(1 - D_{f_i})W_o^{f_i}(\hat{\mathbf{C}}, \mathbf{M}, \mathbf{N}) \quad \text{[3-20]}$$

Advantages in uncoupling the damage effects of the matrix and respective fiber families lie in the ability to individually monitor how each of the respective constituents is sustaining damage. The means of separating the fiber damage from the matrix damage has also been used in modeling the softening of composite layers of arterial walls[60, 61].

3.3.2 Damage Definition and Evolution

In many of the works aimed at modeling damage in biological tissue, the general form of the strain energy density is relatively similar. The most variability in these models is found in the specific definition of the damage parameter, when the parameter initiates and how the parameter evolves once it has been initiated.

In some works, the initiation of damage is defined by a damage criterion. This criterion represents a threshold that governs when the damage parameter may or may not become active. This criterion is typically dependent on the value of the strain energy and has been given in many functional forms, including a one-to-one and a square root (Equation 3-21)[62], where Ξ_t^m is the maximum equivalent strain of the material defined as the square root of the strain energy density up to the current time t.

$$\varphi(E(t), \Xi_s^m) := \sqrt{2W^o(E(t))} - \Xi_t^m \leq 0 \quad \text{.....[3-21]}$$

Equation (3-21) says that for equivalent strain values less than the previous maximum equivalent strain, i.e. $\varphi \leq 0$, damage cannot occur. If the equivalent strain exceeds the maximum equivalent strain, i.e. $\varphi \geq 0$, damage is allowed to occur.

Once the damage occurs, the evolution of the damage is defined by an arbitrary function subject to the nature of the experimental data. Examples of such functions are the exponential models in Equation (3-22)[66] and Equation (3-23)[63].

$$\bar{g}(x) = \beta + (1-\beta)\frac{1-e^{-\frac{x}{\alpha}}}{x/\alpha} \quad \text{[3-22]}$$

$$g_f(D_f) = \frac{1-\exp(\beta_f f_1(\lambda))}{1-\exp(\beta_f f_2(\lambda))} \quad \text{[3-23]}$$

In Equation (3-22), β and α are assumed given parameters and x represents the strain. In Equation (3-23), which was derived for the cyclic loading of human digitorum longus tendons, β_f is a parameter associated with fiber crimping distribution, $f_1(\lambda)$ and $f_2(\lambda)$ are polynomials in definitions of λ that characterize different stretch-damage relationships. Both Equations (3-22) and (3-23) are continuously differentiable and strictly decreasing, which are fundamental requirements for these damage evolution equations.

3.3.3 Fatigue Modeling

In fatigue experiments, a specimen is typically loaded cyclically for a prescribed or arbitrary number of cycles. The amplitude of the cycling is usually constant and the cycling continues up until failure is achieved. The number of cycles to fail a specimen at certain load levels is termed the fatigue life. If the prescribed amplitude is much less than the ultimate failure load of the material, it is evident that some degradation of the material must have occurred

throughout the cycling for failure to have taken place. This degradation can be similarly modeled using the techniques of CDM.

In a fatigue study on bio-prosthetic heart valves[64, 65], the equivalent strain damage criterion was used and the evolution of the damage parameter was formulated to depend on the number of cycles performed (Equation 3-24). The inelastic portion of the second Piola-Kirchoff stress tensor was given by Equation (3-25) , where ε_n^{peak} is the maximum strain achieved in cycle n, ψ_{min} is the minimum equivalent strain needed to initiate fatigue damage accumulation as dictated by the equivalent strain damage criterion[62], ψ_{max} is the maximum equivalent strain limit of the tissue for which only one cycle is needed to cause failure and n_{tot} is the total number of cycles until failure.

$$D_s\left(\varepsilon_n^{peak}\right) = \begin{cases} 0 & \text{if } \varepsilon_n^{peak} < \psi_{min} \\ \sum_{n=0}^{n} n/n_{tot} & \text{if } \psi_{min} \le \varepsilon_n^{peak} \le \psi_{max} \\ 1 & \text{if } \varepsilon_n^{peak} > \psi_{max} \end{cases} \quad \text{.....[3-24]}$$

$$\mathbf{S} = (1 - D_s)\frac{\partial W^o}{\partial \mathbf{E}} \text{.....[3-25]}$$

The applicability of Equations (3-24) and (3-25) to the cyclic nature of fatigue is apparent. It can be seen that the quantity $(1 - D_s)$ steadily decreases the elastic response of the tissue up until $n \to n_{tot}$, $D_s \to 1$, $\mathbf{S} \to 0$ and failure has occurred. The failure condition of zero stress is universal and has been explicitly modeled in regard to medial collateral ligaments of the knee[66].

3.3.4 Viscoelasticity

Viscoelasticity is a time-dependent phenomenon where the stress carried in a material can decrease over time for a constant value of stretch. This is relevant in the topic of fatigue because both phenomena represent a degradation of strength over a period of time. Experimentally, viscoelastic effects have been observed to occur in the medial collateral ligaments of rats[67] and rabbits[68] subjected to stress relaxation tests. In human ACLs, this stress relaxation effect can affect the fiber alignment in the AM and PM bundles[69].

The time dependent nature of viscoelasticity presents some challenges in the constitutive modeling of such behavior. This is primarily due to the fact that the functional form of the stress must include a dependence on time. This is further complicated for ligaments where viscoelasticity may be present in both the matrix and fibers. Assuming that these constituents have different viscoelastic behavior, convolution integrals (Equation 3-26) have been used to represent the time dependence of the stress in the constitutive modeling of ligaments displaying viscoelastic characteristics[70], where $G^f(t)$ and $G^m(t)$ are different relaxation functions for the matrix and fibers, respectively. Because Equation (26) involves integration, a closed form solution is difficult to obtain and therefore, numerical software is the preferred method of solution.

$$S_{ij}(t) = p(t)C_{ij}^{-1}(t) + \int_0^t G^f(t-\tau)\frac{d\left(S_{ij}^{dev_f}\right)}{d\tau}d\tau + \int_0^t G^m(t-\tau)\frac{d\left(S_{ij}^{dev_m}\right)}{d\tau}d\tau \text{.....[3-26]}$$

Numerous software packages that utilize finite element techniques operate using implicit integration where the solution at the current time step is updated based on the solution at the

previous time step. The topic of implementing constitutive modeling for finite element simulation is discussed in section 3.4.

3.3.5 Permanent Set / Residual Stress

Permanent set is a condition observed in the behavior of biological tissues where, after unloading, residual strains remain present in the unloaded tissue. Ideally, when completely unloaded the strain in the tissue would be zero, however, with permanent set there can be non-zero strain values for stress levels of zero. Several constitutive models have been developed which can account for this effect.

The existence of residual strains prevents the material from completely returning to the undeformed state upon complete removal of load. In terms of continuum mechanics, this prescribes the existence of residual stresses that will change the reference configuration of the body. This asserts that materials which display permanent set effects are inelastic and can thus be modeled by pseudo-elastic constitutive damage models. Similar to stress softening, permanent set effects have been incorporated into these models through the inclusion of a scalar parameter that evolves throughout the loading and does so independently of the stress softening (Equation 3-27)[58], where the parameter $\eta_2 \in [0,1]$ is the residual strain variable, $\widehat{\mathrm{N}}$ is an equation which characterizes the residual strains and ϕ is a dissipation function.

$$\mathrm{W}(\lambda_1, \lambda_2, \eta_1, \eta_2) = \eta_1 \widehat{\mathrm{W}}_{\mathrm{o}}(\lambda_1, \lambda_2) + (1 - \eta_2)\widehat{\mathrm{N}}(\lambda_1, \lambda_2) + \phi(\eta_1, \eta_2) \ldots\ldots\ldots [3\text{-}27]$$

It can be seen in Equation (3-27), that the damage parameters η_1 and η_2 operate independently. Similar to the formulation of η_1[56], the functional form of η_2 depends only on the strain energy.

Because the permanent set can represent a value of stretch at zero stress, it is somewhat related to the observations of fiber crimping. It is known that fibers in biological tissues are crimped[71] up until some level of stretch where they become straightened and can now bear load (Figure 12).

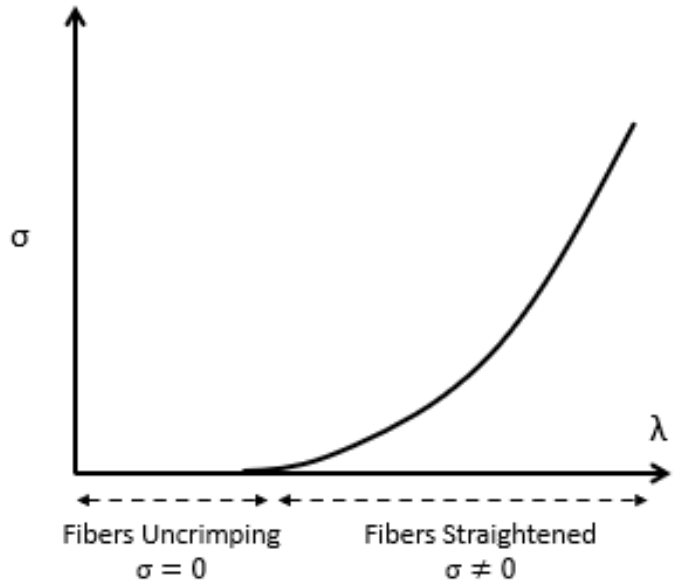

Figure 12: Stress-Stretch Behavior of Ligaments Displaying Fiber Crimping

A permanent set would offset this 'straightening stretch' value to some degree. This was represented in constitutive form (Equation 3-28) for an anisotropic damage model with the inclusion of a dimensionless parameter $\bar{I}_{i_o}$, representing the fiber crimp, and a weighting factor w_i, that can alter the value of this fiber crimp as the structural changes occur[72].

$$W(\mathbf{C}, \mathbf{M}, D_m, D_{f_4}, w_4) = \mu[1 - D_m][\bar{I}_1 - 3] + \left[1 - D_{f_i}\right]\frac{c_1}{c_2} e^{c_1[\bar{I}_i - w_i\bar{I}_{i_o}] - c_2[\bar{I}_i - w_i\bar{I}_{i_o}] - 1} \text{..[3-28]}$$

3.4 Finite Element

The finite element method (FE) is a computational technique developed for the mechanical simulation of a variety of physical systems including solid, fluid, thermal and wave-like systems. It is a numerical tool used to simulate the aggregate effect of a series of small perturbations. The contents of section 3.4.1 present an overview of the FE method[73, 74], necessary to provide a foundation for the FE modeling of biological tissues.

3.4.1 The Finite Element Method

The FE method begins with the presentation of a physical system subjected to any number of influences. These can be external loads such as forces $\vec{\mathbf{F}}$, moments $\vec{\mathbf{M}}$; boundary conditions such as prescribed displacements, rotations or velocities $\vec{\mathbf{v}}$; external fields and internal fields such as pressures $\vec{\mathbf{P}}$, and body forces $\vec{\mathbf{b}}$; or energy fluxes such as heat $\vec{\mathbf{q}}$ or electricity (Figure 13).

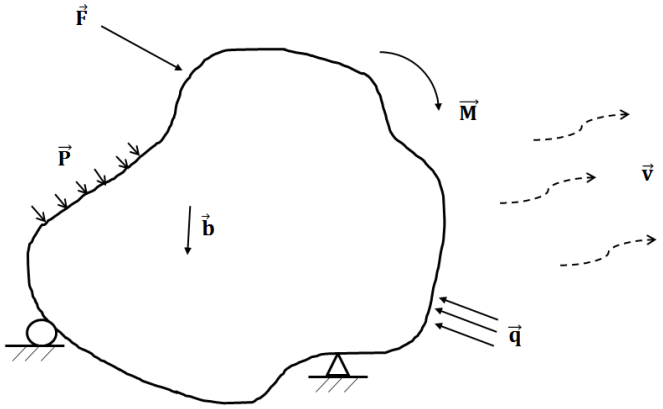

Figure 13: Arbitrary Body Subjected to Various External and Internal Influences

Using the principles of mathematics and physics, a partial differential equation (PDE) can be constructed to represent the behavior of the system (Equation 3-29). Solution of this PDE would provide information on how the system responds to the imposed conditions. Depending on the nature of the problem, this solution could be in terms of the resulting displacement, strain, stress, energy etc. This PDE, with the associated boundary conditions, is termed the strong form.

$$\frac{\partial^n}{\partial x^n}[u(x)] + \frac{\partial^{n-1}}{\partial x^{n-1}}[u(x)] + \ldots\ldots + u(x) = f(x) \ldots\ldots\ldots\ldots\ldots\ldots [3\text{-}29]$$

The PDE can be converted into an integral form (Equation 3-30), termed the weak form, by multiplying the PDE by a weighted residual $w(x)$ and integrating over the domain. By balancing the derivatives on $u(x)$ and $w(x)$, the weak form of the weighted residual can be obtained.

$$\int \left[\frac{\partial^n}{\partial x^n}[u(x)] + \frac{\partial^{n-1}}{\partial x^{n-1}}[u(x)] + \ldots\ldots + u(x)\right] w(x) = \int f(x) w(x) \ldots\ldots [3\text{-}30]$$

The weak form then must be converted into a form that is suitable for numeric solution. For this, the weak form is discretized into a summation involving matrices. This process starts with the discretization of the domain into a series of elements (Figure 14). These elements have a number of nodes where the desired output variables are approximated as the product of the individual nodal output u_i, and a shape function N_i.

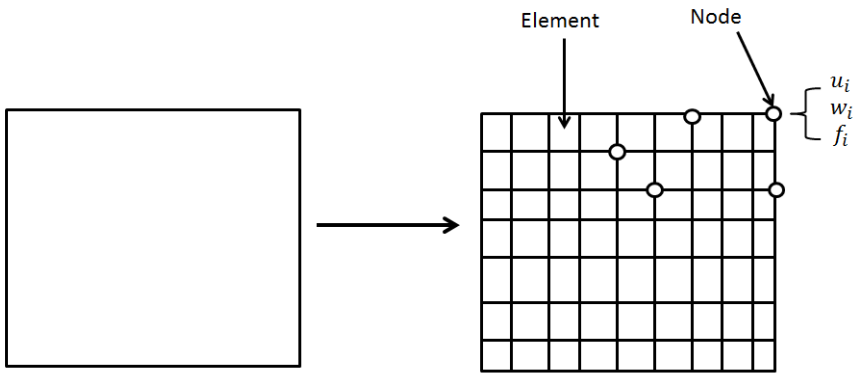

Figure 14: Discretization of Problem Domain into Elements and Nodes

The shape function is a ratio of polynomials whose order depends on the type of element. This approximation is applied to each term in the weak form and summed over the entire number of nodes, n (Equation 3-31).

$$\int \left[\frac{\partial^{n}}{\partial x^{n}}(\sum N_i u_i) + \frac{\partial^{n-1}}{\partial x^{n-1}}(\sum N_i u_i) + \ldots\ldots + (\sum N_i u_i)\right](\sum N_i w_i) - \int(\sum N_i f_i)(\sum N_i w_i) = 0 \ldots [3\text{-}31]$$

Equation (3-31) can be further reduced into a single matrix equation where $\sum N_i u_i = [N]\{u\}$. Reducing Equation (3-31) to the form of Equation (3-32) allows for the elimination of the weighed residual term w_i and presents the problem in a form that can be solved using the standard techniques of matrix algebra.

$$\int \left[\frac{\partial^{n}}{\partial x^{n}}[N]^{T} + \frac{\partial^{n-1}}{\partial x^{n-1}}[N]^{T} + \ldots\ldots + [N]^{T}\right][N]\{u\} - \int [N]^{T}[N]\{f\} = 0 \ldots\ldots [3\text{-}32]$$

In Equation (3-32), the term that multiples the displacement vector {u}, is termed the stiffness matrix [K]. The second term is called the residual {R}. These matrices are formed for

every element and assembled into global matrices for the entire body. If the global stiffness matrix $[K]_{global}$ is invertible, then the solution for the global output variable $\{u\}_{global}$, can be determined (Equation 3-33).

$$\left(\{u\}_{nx1} = [K]_{nxn}{}^{-1}\{R\}_{nx1}\right)_{global} \quad \text{[3-33]}$$

The external conditions applied to the system are typically enforced quasi-statically, where the full magnitude of the external perturbation is approached incrementally over a series of time steps, t_n. With this, Equation (3-33) is solved at each time increment and updated over the course of the analysis, taking the solution for $\{u\}$ at the previous step, t_{n-1} , as the input conditions for the current step. This allows for the visualization of how the solution evolves over the course of the simulation.

3.4.2 Application to Constitutive Modeling

The constitutive modeling principles discussed in the previous section exist in explicit form in most software packages and can be readily applied to the problem of choice. However, when the nature of the problem requires the definition of some behavior that is not represented in these available models, unique models can be implemented as user defined materials. In ABAQUS (Dassault Systèmes Simulia Corp, Providence, Rhode Island) these user defined materials are implemented using the UMAT subroutine[75]. This subroutine has been used by various authors to implement their desired material models.

In the definition of the material it is necessary to present a closed formed expression for both the Cauchy stress **σ**,and elasticity tensor $\mathbb{C}$. For an anisotropic, hyperelastic, incompressible material with one preferred material direction **a**, the 2nd Piola-Kirchoff stress is given by Equation (3-34). The Cauchy stress is the push-forward representation of **S** (Equation 3-35).

$$\mathbf{S} = 2\left[\left(\frac{\partial \mathrm{W}}{\partial \mathrm{I}_1} + \mathbf{I}\frac{\partial \mathrm{W}}{\partial \mathrm{I}_2}\right)\mathbf{I} - \frac{\partial \mathrm{W}}{\partial \mathrm{I}_2}\mathbf{C} + \frac{\partial \mathrm{W}}{\partial \mathrm{I}_4}\mathbf{a}\otimes\mathbf{a}\right] + \mathrm{p}\mathbf{C}^{-1} \quad \text{[3-34]}$$

$$\boldsymbol{\sigma} = 2\left[\left(\frac{\partial \mathrm{W}}{\partial \mathrm{I}_1} + \mathbf{I}\frac{\partial \mathrm{W}}{\partial \mathrm{I}_2}\right)\mathbf{B} - \frac{\partial \mathrm{W}}{\partial \mathrm{I}_2}\mathbf{B^2} + \mathrm{I}_4\frac{\partial \mathrm{W}}{\partial \mathrm{I}_4}\mathbf{a}\otimes\mathbf{a}\right] + \mathrm{p}\mathbf{I} \quad \text{[3-35]}$$

The elasticity tensor (i.e. stiffness matrix) is given, in material form, by Equation (3-36). Applying Equation (3-36) to the expression for **S**, gives the closed form for the material version of $\mathbb{C}$ (Equation 3-37)[76]. By applying the push-forward of $\mathbb{C}$ one can derive the spatial version of the elasticity tensor.

$$\mathbb{C} = 2\frac{\partial \mathbf{S}}{\partial \mathbf{C}} \quad \text{[3-36]}$$

$$\mathbb{C} = 4\left[\mathbf{I}\otimes\frac{\partial}{\partial \mathbf{C}}\frac{\partial \mathrm{W}}{\partial \mathrm{I}_1} + \mathbf{I}\otimes\frac{\partial \mathrm{W}}{\partial \mathrm{I}_2}\frac{\partial \mathrm{I}_1}{\partial \mathbf{C}} + \mathrm{I}\otimes\mathrm{I}_1\frac{\partial}{\partial \mathbf{C}}\frac{\partial \mathrm{W}}{\partial \mathrm{I}_2} - \mathrm{C}\otimes\frac{\partial}{\partial \mathbf{C}}\frac{\partial \mathrm{W}}{\partial \mathrm{I}_2} - \frac{\partial \mathrm{W}}{\partial \mathrm{I}_2}\frac{\partial \mathbf{C}}{\partial \mathbf{C}} + \mathbf{a}\otimes\mathbf{a}\otimes\frac{\partial}{\partial \mathbf{C}}\frac{\partial \mathrm{W}}{\partial \mathrm{I}_4}\right] \quad \text{[3-37]}$$

Equations (3-34)-(3-37), can be written in indicial notation for ease of expression in the finite element script. Once these respective tensors have been defined, the finite element solution is then approached in an iterative fashion[77]. Based on the prescribed loading and boundary conditions, the deformation gradient, along with the Jacobian, is calculated at the current time step.

The deformation gradient is then used to calculate the respective Cauchy-Green stretch tensors, which are then used to calculate the stress. The stress is then used to calculate the stiffness. An appropriate equilibrium check is used to check the convergence conditions for the current time step. If the conditions are met, the solver moves to the next time step, taking the parameters from the previous time step as inputs. This process continues until the final time increment has been reached.

For the finite element simulation of damage, the damage variables have to be defined as internal variables in the material definition. As discussed in the previous sections, these parameters are often written with a dependence on the strain energy. The strain energy at each time step can be calculated based on the value of the strain invariants. The internal variable at the current time step is then updated based on the strain energy of the previous time step[78] and modifies the stress response as prescribed by the user.

3.4.3 Convergence

With the modeling of complicated problems, it is expected that a confident solution should not only be feasible, but also stable. Convergence of the finite element solution is a critical aspect of achieving a stable and reliable result. It ensures that the obtained solution is uninfluenced by the parameters of the model. Most commonly, convergence can be sought in terms of the changing mesh size and element order. If the desired solution remains relatively unchanged with the changing properties of the mesh, then the solution can be considered to have good mesh convergence.

For the modeling of hyper-elastic material, the issue of volumetric locking can affect convergence. Because these materials are typically assumed to be incompressible (i.e. infinite

bulk modulus) they are volume preserving and, depending on the type of element, can cause problems with finding a solution. To avoid these problems, it is best to use quadratic elements that have more degrees of freedom, allowing the elements to deform as needed to preserve the volume of the structure.

On the administrative side of the simulation, convergence problems can be encountered with the prescribed solution settings. With approaching the solution iteratively at prescribed time steps, the rate at which the solution is approached depends on the size of the step. If the step is too large, convergence can possibly be missed. In this case, a cutback is performed where the solver moves progressively to smaller time steps until a converged solution is found. For each problem, there is a critical time step, t_{crit} , that can be calculated, beyond which the solution may become unbounded. A generalized eigenvalue problem (Equation 38) can be derived for each element by solving the homogenous PDE with arbitrary stiffness and capacitance matrices, **k** an **m**. Solving Equation (3-38) for each element, t_{crit} is then proportional to the maximum eigenvalue of all the elements λ^{e}_{max} (Equation 3-39).

$$\mathbf{k}^{e}\mathbf{x}^{e} = \boldsymbol{\lambda}^{e}\mathbf{m}^{e}\mathbf{x}^{e} \quad \text{[3-38]}$$

$$t_{crit} \leq \frac{2}{\lambda^{e}_{max}} \quad \text{[3-39]}$$

3.4.4 Validation

Validation of a finite element model can be inferred from the relative agreement of the model with experimental findings. The experimental findings used for validation can be numerous, as seen in an FE simulated knee model where tibiofemoral kinematics, pressures and ACL/MCL strains were all used[79]. It is expected that the simulated ligament stress-stretch response will agree with the empirical response to within some degree of error. The magnitude of this agreement can be measured with an error term which compares the numerical result to the analytical value (Equation 3-40).

$$\%\text{error} = \frac{|\sigma(\varepsilon_i)_{\text{analytical}} - \sigma(\varepsilon_i)_{\text{numeric}}|}{\sigma(\varepsilon_i)_{\text{analytical}}} \text{x} 100 \ldots\ldots\ldots\ldots\ldots [3\text{-}40]$$

In Equation (3-40), $\sigma(\varepsilon_i)$ is the value of the stress at a given value of strain. The value of %error needed to infer validation is up to the discretion of the simulator and is more stringently dictated by the needs of the problem.

4.0 Methodology

The objective of this work was to predict the amount of damage the AMCL will sustain as a result of repetitive overhand throwing. This will be done through the construction of a predictive computational model. All physical testing will be done using cadaveric specimens. Testing will be conducted to acquire data on the mechanical behavior of the healthy AMCL. Data will also be collected on how the ligament accumulates damage from frequent valgus throwing motions. This data will then be used to inform a constitutive model which will be incorporated into a finite element material model. This material model will then be applied to an anatomical geometry of the ligament-bone structure to simulate and predict damage accumulation from overhand throwing induced fatigue.

4.1 Paired Testing

Paired testing involves the use of two elbow specimens from the same donor. The presumption is that both of the AMCL specimens will possess similar mechanical properties. This is critical for the proposed experimental methodology which involved two stages.

The first stage was an elastic mechanical test. In this test, the elbow specimens were elongated to first determine its healthy stress-strain behavior. This behavior will be used to tune the parameters of the elastic portion of a constitutive model suitable for biological, fiber-imbedded tissue. The specimen will then be elongated to failure to determine the absolute failure strength.

The second stage was a fatigue test. In this test, the specimens were repeatedly loaded with a valgus moment for an indefinite number of cycles until failure was achieved. The magnitude of the applied moment was proportional to the failure load determined in the elastic test. The calculation for the moment M_f, in Nm is given by Equation (4-1), where F_f is the determined contralateral failure load, L_{cap} is the distance from the center of the capitellum to the center of the AMCL (measured using calipers) and C is a conversion factor. An illustration of these parameters is presented in Figure (15).

$$M_f = F_f * L_{cap} * C \quad \text{[4-1]}$$

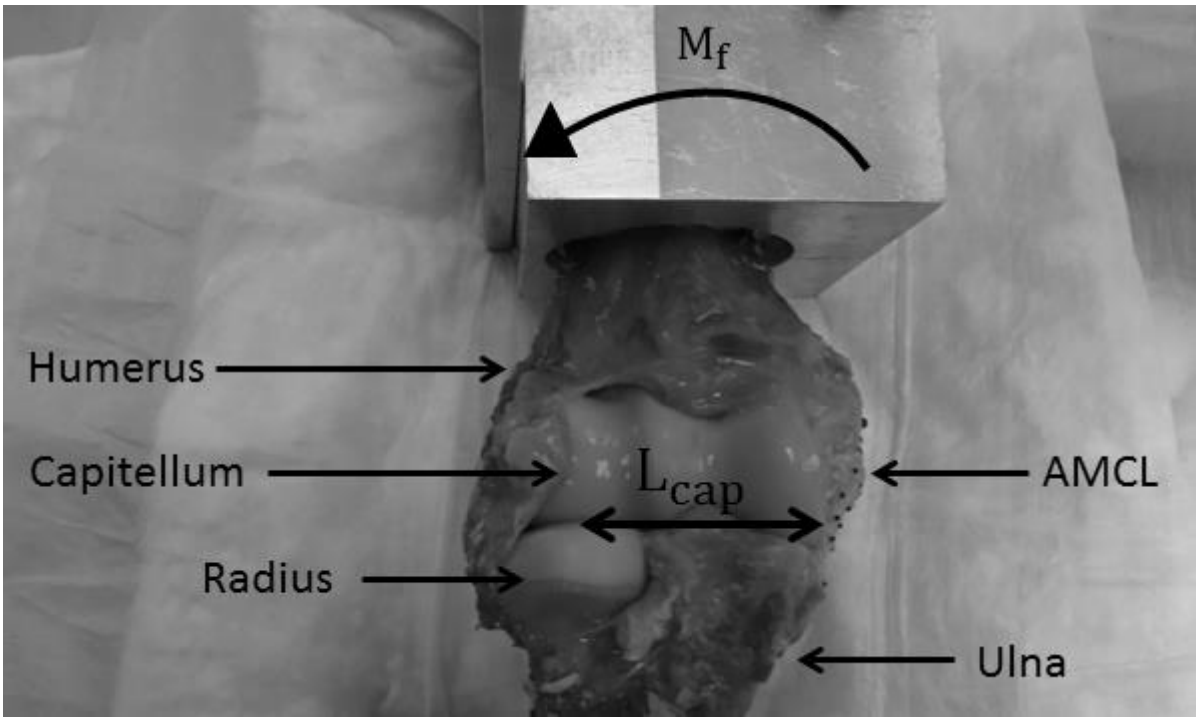

Figure 15: Illustration of Test Specimen and Parameters Used for Valgus Moment Calculation

The results of the fatigue test defined the parameters for the inelastic portion of the constitutive model.

The experimental portion of the work concluded after these two stages and was followed by the computational effort. The computational aspect involved the use of a transversely isotropic hyperelastic material model in conjunction with the experimentally determined nonlinear damage accretion behavior to simulate the testing conditions and predict the resulting behavior. The material model was driven by the tuned constitutive model and the physical specimen geometry was formed from MRI images taken of actual elbow specimens. The details of the work will be expanded upon in the following sections.

4.2 Specimen Preparation

Twenty-two cadaveric elbow specimens were used in two separate stages of the study. In the first stage, the elastic testing, eleven specimens were prepared with the removal of all soft tissue surrounding the UCL. This left only the exposed ulna, humerus, radius and UCL. The radius was subsequently removed. The posterior bundle and transverse bundle of the UCL were both transected away, along with the joint capsule, leaving the anterior bundle of the UCL, the AMCL, as the only connecting tissue between the ulna and humerus.

In order to be mounted in the testing fixture, the shaft of the ulna and humerus were cut to fit the length of two separate PVC pipes. The humerus was placed into the first pipe at a neutral flexion/extension angle and bonded in place by an adhesive polyester resin. With the second PVC section filled with polyester resin, the ulna was set into the second pipe while mounted in an MTS machine. Use of the machine allowed for consistent anatomical alignment of the ulna and

humerus. A set screw was then drilled into both of the PVC holsters through the bone. This process secured the bones to the interior of the PVC holsters (Figure 16).

Figure 16: Prepared Specimen with Humerus and Ulna Secured into PVC Holsters

Optical markers, 0.8 mm black spheres, were then attached to the ligament using a cyanoacrylic adhesive. A single column of markers was placed along the anterior, middle and posterior portions of the ligament with equal spacing between markers and between columns. This placement distinguished between three individual bands of the ligament. A set of three additional 1 mm diameter markers was placed at the humeral and ulnar insertions. These served as points of measure of absolute displacement. A single marker was then placed above and below the joint line, serving as indicators for joint opening. Lastly, the olecranon was removed in order to alleviate any restrictions of the specimen to vertical distraction. The prepared specimen can be seen in Figure (17).

Figure 17: Prepared Specimen Secured into Loading Fixture

The preparation of the specimens used in stage two, the fatigue testing, was similar. The only differences were that the radius and olecranon were not removed. The ulna, radius and humerus were also cut to a longer length, as necessitated by the design of the fatigue apparatus.

4.3 Elastic and Failure Testing Protocol

The prepared specimen was loaded into the testing fixture. The fixture allowed for flexion of the specimen from 0° to 120° and sat within an MTS machine which was capable of applying tensile, compressive and twisting loads controlled through MATLAB (MathWorks, Natick, MA). The action of the test was recorded by two cameras. The range of the cameras was checked as the

specimen was positioned from 0° to 90°. The cameras were then calibrated with the specimen positioned at 45°.

Testing began at 0° of flexion, where the specimen was vertically elongated, upwards with respect to the ulna, to a prescribed displacement value in mm. The value of displacement was iteratively achieved with 0.5 mm increments to reach a load of at least 80 N. This was done to achieve adequate lengthening of the ligament without risking rupture. The recorded displacement was achieved using displacement control for three preconditioning cycles, followed by a fourth cycle which was recorded by the cameras. This was repeated for every angle in 30° increments up to 120°. A sample of the load vs. time plot for specimen 4 can be seen in Figure (18).

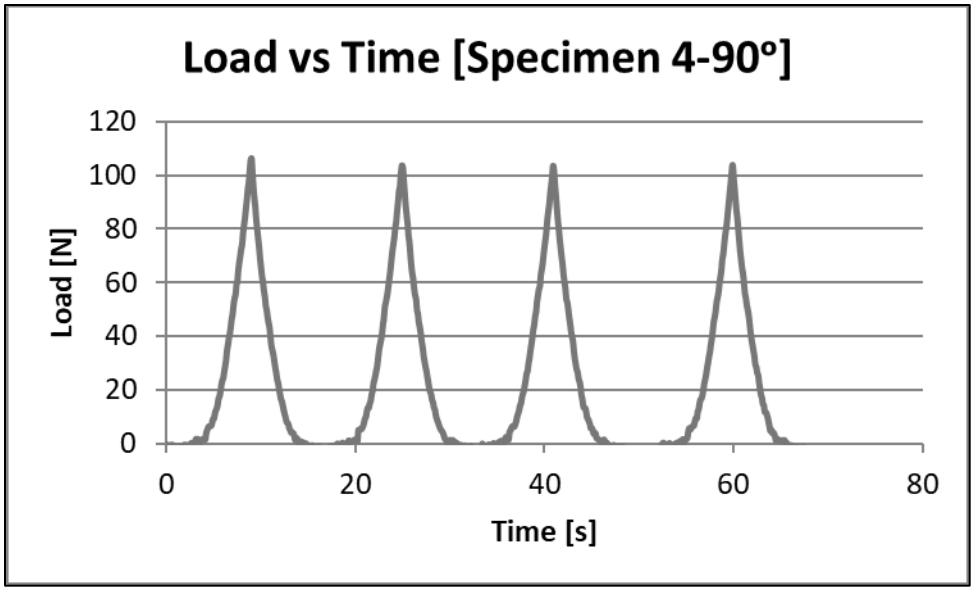

Figure 18: Load vs Time Plot for Arbitrary Specimen in the Elastic Testing Protocol

For the failure test, the specimen was returned to 90°. The displacement value was set to an arbitrarily large magnitude and the specimen was elongated until failure occurred. The failure was signified by a sharp drop in the force vs time plot (Figure 19). The maximum failure load

was recorded. An example from one of the failed specimens (specimen 4) can be seen in Figure (20). All camera and MATLAB data was stored for later processing.

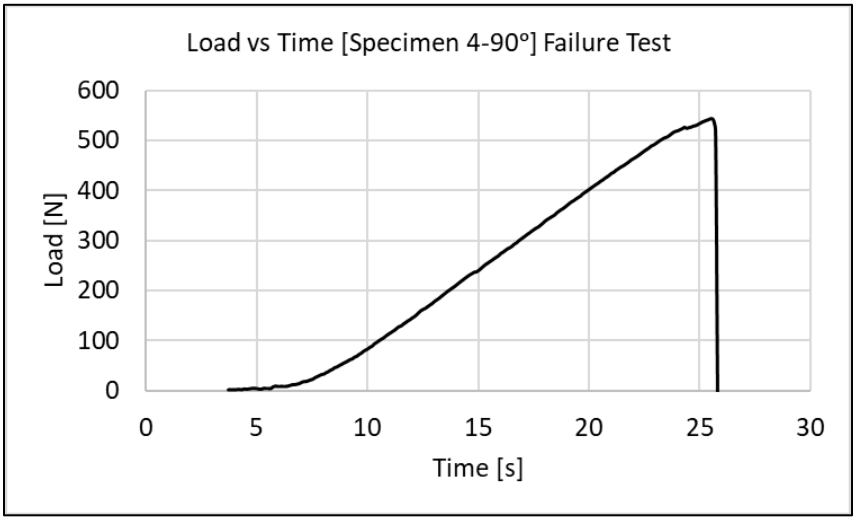

Figure 19: Load vs Time Plot for Specimen 4 Tested to Failure

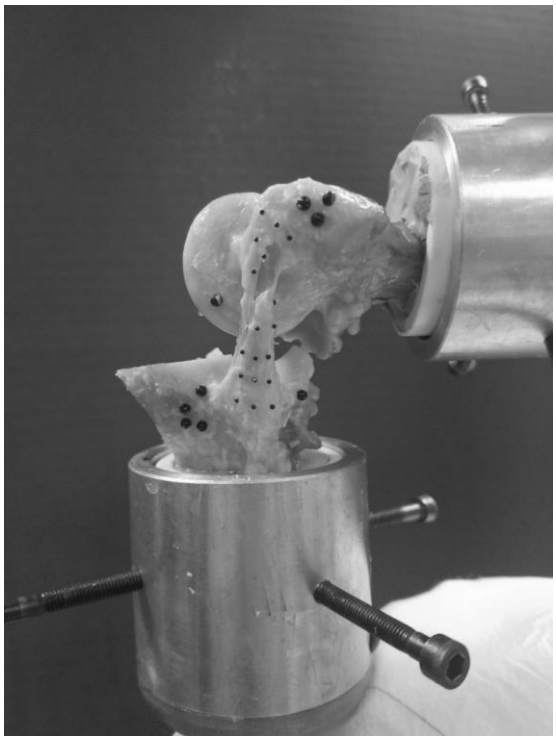

Figure 20: Failure in Vertical Elongation of Specimen 4

4.4 Fatigue Testing Protocol

Once the elastic and failure testing of the specimen concluded, the fatigue testing followed using a specimen from the contralateral side. The device used to perform the test was of a custom design (Figure 21). This design allowed the specimen to be loaded into the device through the use of an aluminum fixture. The interior of each fixture was sized to fit the PVC holsters of the specimen. Once inside, the PVC was tightened to the fixture using screws. The screws ensured that no relative displacement, or sliding, would exist between the contacting surfaces of the PVC and aluminum.

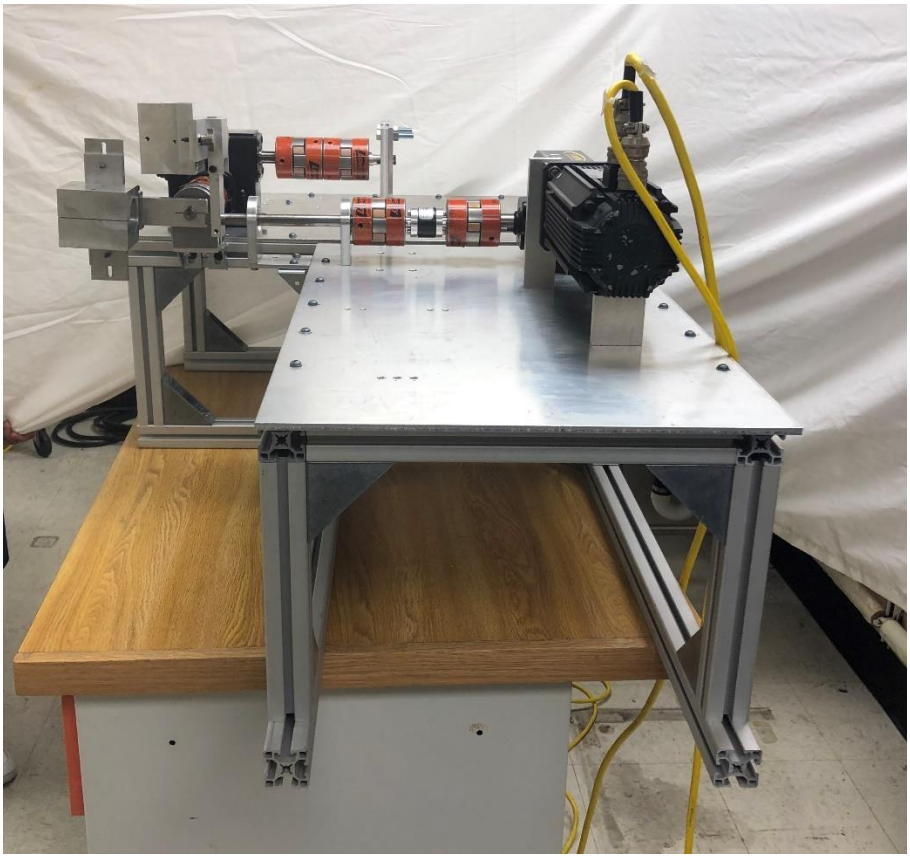

Figure 21: Fatigue Testing Apparatus

The testing device consisted of two swing arms. These were aluminum, t-shaped handles, custom designed to attach the fixtures to the testing device. One swing arm was always stationary. The other swing arm was connected to a 10 Hp, 450 Hz servo motor. The action of the motor was controlled through MATLAB. Depending on the type of elbow specimen, right or left, the orientation of the two swing arms relative to one another, would be altered so that the ulna and radius would always be attached to the arm connected to the motor. This was done so that the radius could rotate on the capitellum, replicating realistic forearm rotation. A labeled diagram of the testing apparatus is presented in Figure (22).

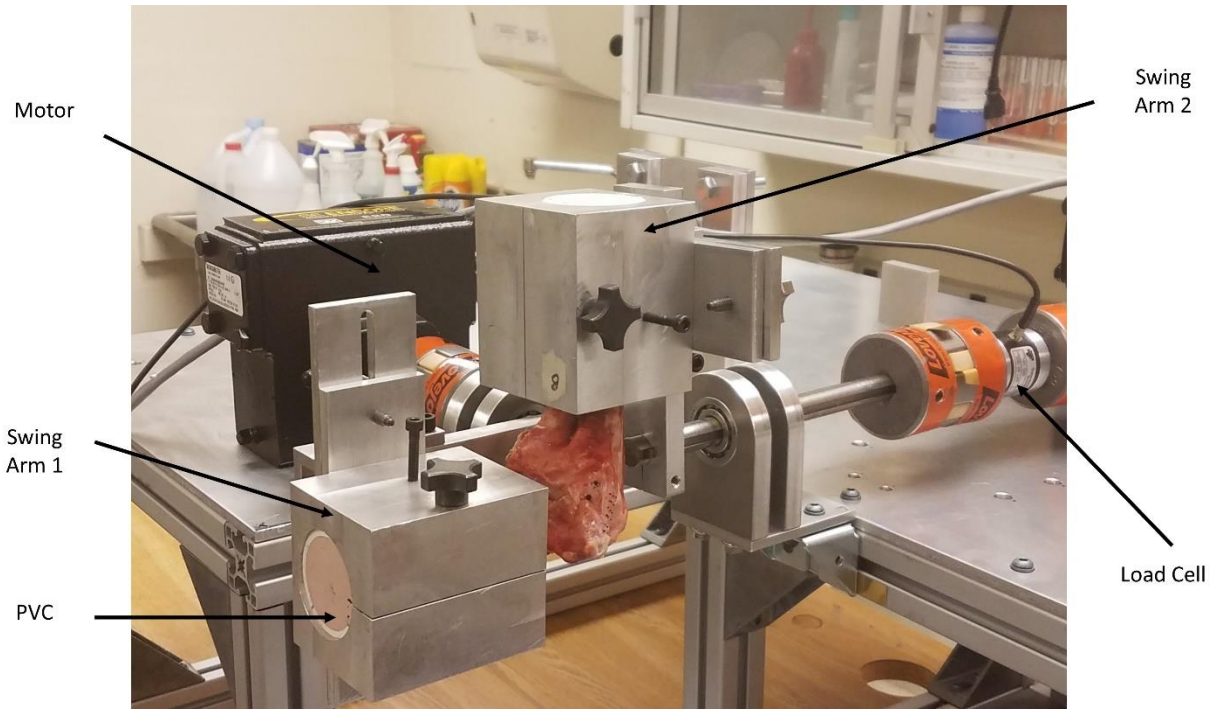

Figure 22: Labeled Schematic of the Fatigue Testing Components

A set of bolts were used to attach the fixture to the swing arms of the fatigue tester. Horizontal and vertical groves in the swing arms allowed the screws to be translated, as needed, to achieve optimum placement of the specimen within the device. Ideally, the specimen was

positioned in a manner which would allow the radius to rotate along the capitellum, with the fulcrum of the rotation aligned with the center of the capitellum. Having this position would most closely mimic the lever motion of the static humerus, with respect to the rotating forearm. The fully prepared specimen mounted into the fatigue tester can be seen in Figure (23).

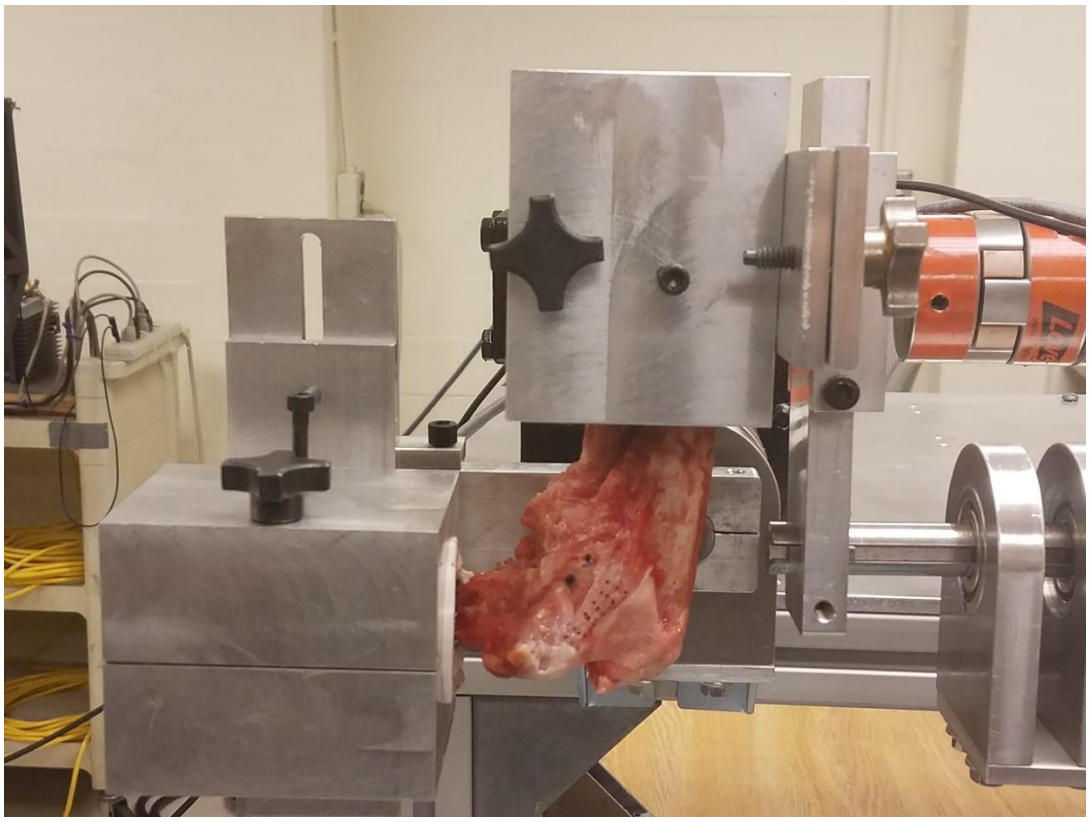

Figure 23: Prepared Specimen Secured within the Fatigue Tester

4.5 Data Acquisition

There were two classes of data being monitored for the tests. The first was the motion data of the optical markers. The motion of the markers throughout the test was captured by two high

resolution Prosilica GC 1350C cameras (Allied Vision Technologies, Exton, PA). The use of two cameras allowed for a higher degree of spatial resolution. The cameras were mounted on two tripods and positioned for the most optimum viewing of the specimen (Figure 24). The second type of data collected was the kinetic and kinematic data recorded through MATLAB. The load cell was connected to the movable swing arm and data on three variables was collected. These variables were torque τ, angular position θ, and elapsed time t.

Figure 24: Positioning of Cameras Used for Specimen Recording

4.6 Fatigue Testing Protocol

With the specimen loaded into the testing apparatus and the means of data acquisition prepared, testing of the specimen was ready to commence. The goal of the fatigue test was to load the specimen with a valgus moment repeatedly until failure of the AMCL was achieved.

4.6.1 Standard Fatigue Properties

The characterization of the fatigue properties of the AMCL included the formation of a general fatigue life curve, as seen in the example of Figure (25), where the cycles to failure n, increase as the stress level σ, decreases.

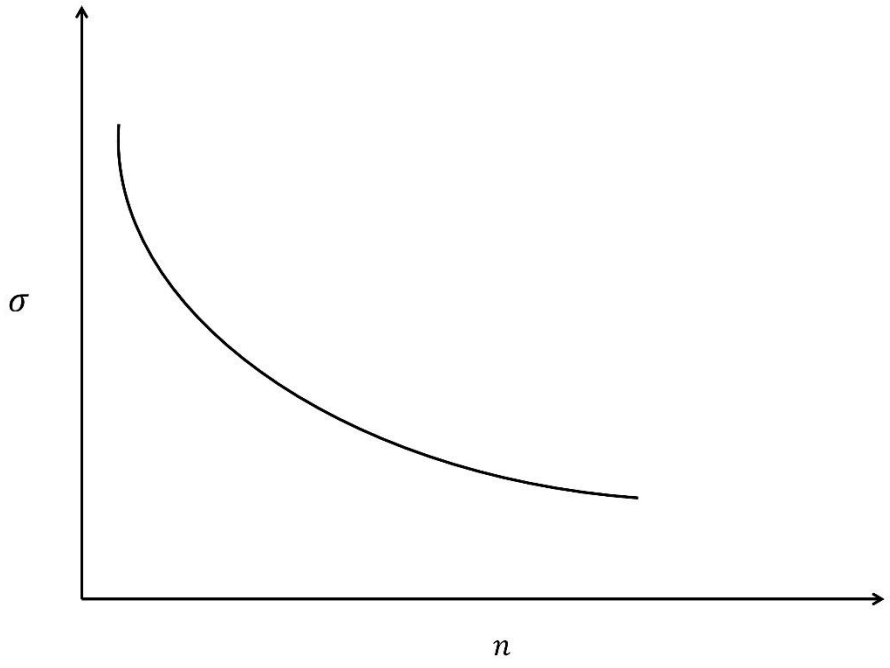

Figure 25: Representation of General Fatigue Life Curve for an Arbitrary Material

The contralateral side for the eleven specimens examined in the elastic test, were tested in valgus fatigue. The magnitude of the applied moment was chosen so that the results could be analyzed in a uniform manner for all specimens and simultaneously reflect fatigue behavior relevant to the individual specimen. For this, the applied moment was chosen to be a multiple of the individual specimen valgus failure moment $\mathbf{M_f}$. As calculated using Equation (41), $\mathbf{M_f}$ is a theoretical failure moment for which failure occurs after 1 cycle. Five specimens were tested with a valgus moment of 90% of their respective $\mathbf{M_f}$ and six were tested at 80% of $\mathbf{M_f}$.

With the load level selected, the specimens were placed into the apparatus. Testing began with a single valgus cycle at half the magnitude of the $\mathbf{M_f}$ to observe the stretch level of the specimen and to ensure that failure did not occur at the first cycle. Three cycles were then applied at a frequency of 0.5 Hz for preconditioning, followed by a fourth cycle which was recorded by the camera system. Testing then proceeded with five hundred uninterrupted cycles at a frequency of 1Hz. At the conclusion of the 500 cycles, the procedure of preconditioning and recording repeated indefinitely until failure was achieved.

During the test, saline was manually applied to the specimens regularly to prevent dehydration of the tissue. In the event that failure was not achieved within a reasonable time frame, the specimen was refrigerated and the testing was resumed the following day. If necessary, the interval of 500 cycles was increased to 2000 cycles to automate the process further for specimens that required extensive testing time.

The total number of cycles to achieve failure at each stress level was recorded using MATLAB and averaged together for each of the specimens at each $\mathbf{M_f}$ multiple of 90% and 80%. A graph showing the intermediate results for 4 specimens, along with the standard deviations in load magnitude and failure cycles, is given in Figure (26).

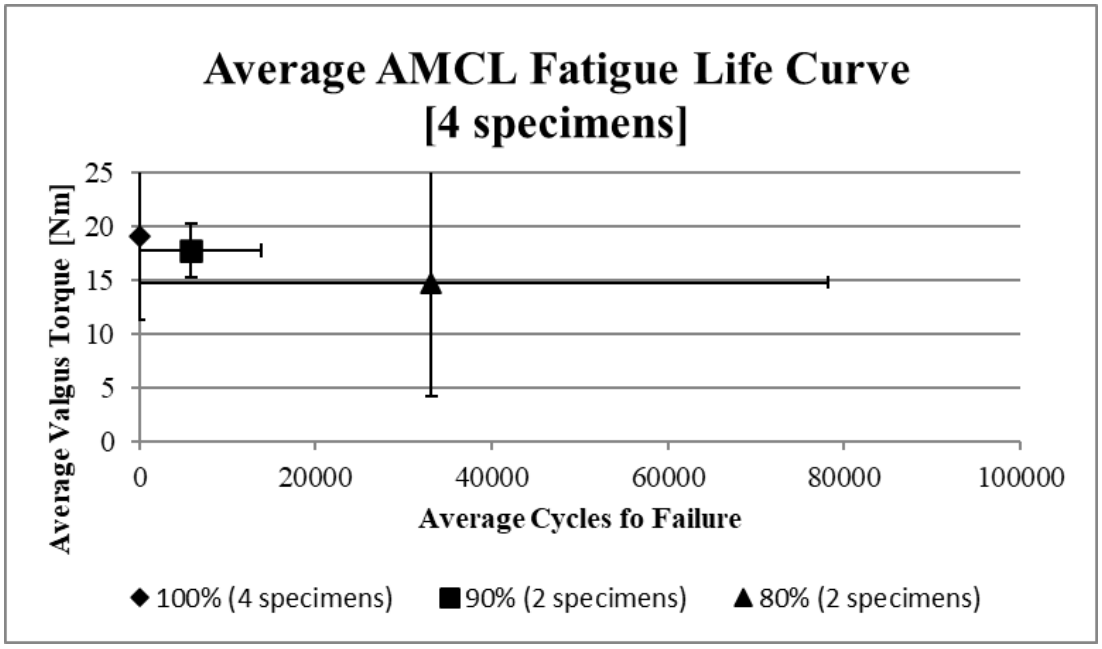

Figure 26: Preliminary Results for the Average Fatigue Life for 4 Specimens Tested at 90% and 80% of M_f

4.6.2 Damage Definition

The fatigue life curve defines how many valgus loading cycles the AMCL can perform at a particular load level until failure occurs. However, it does not describe how the damage is accumulated throughout the loading. For this work, we will utilize a rotational displacement-based damage definition, where the initial valgus angle of the rotating elbow θ_o, gradually increases over the course of indefinite cycling to the maximum angle θ_m, where failure occurs.

To uncover how the rotation angle increases over the loading cycle, the absolute rotational position of the elbow was recorded using MATLAB at a frequency of 100 Hz. An example of a complete plot of the rotational angle θ, vs cycle number n, is given in Figure (27). The plot starts from the initial angular position of the specimen and gradually increases up to the point of failure,

signified by the sudden jump in angular position. The failure of a particular specimen during the cyclic valgus testing is shown in Figure (28).

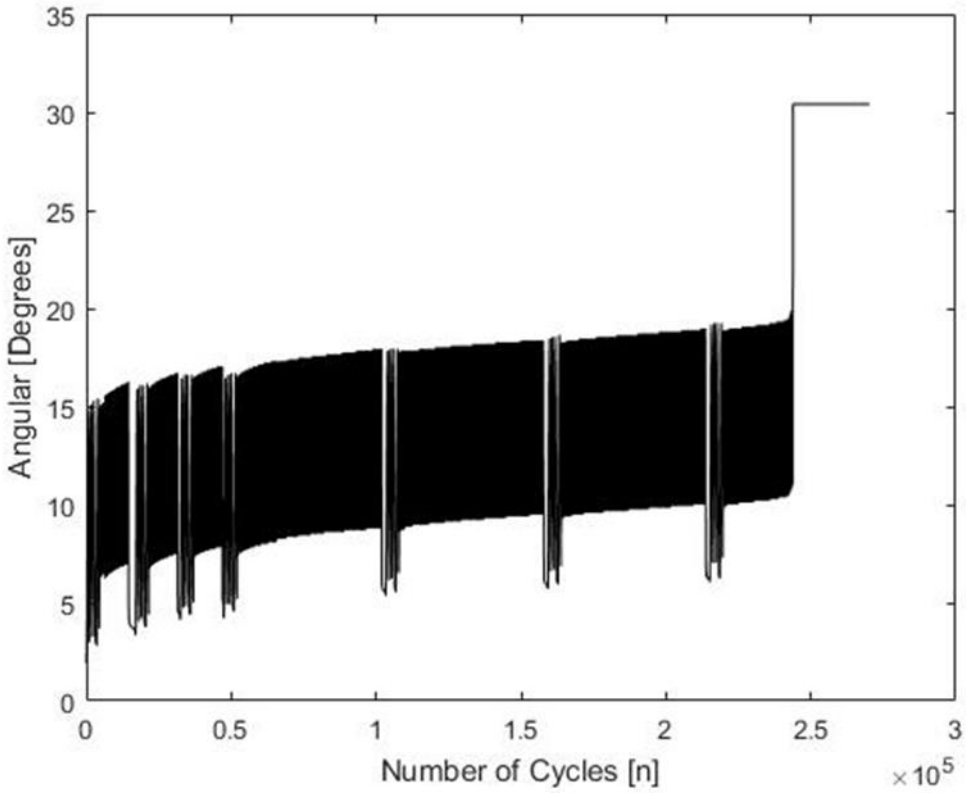

Figure 27: Angular Position vs Time for Representative Specimen

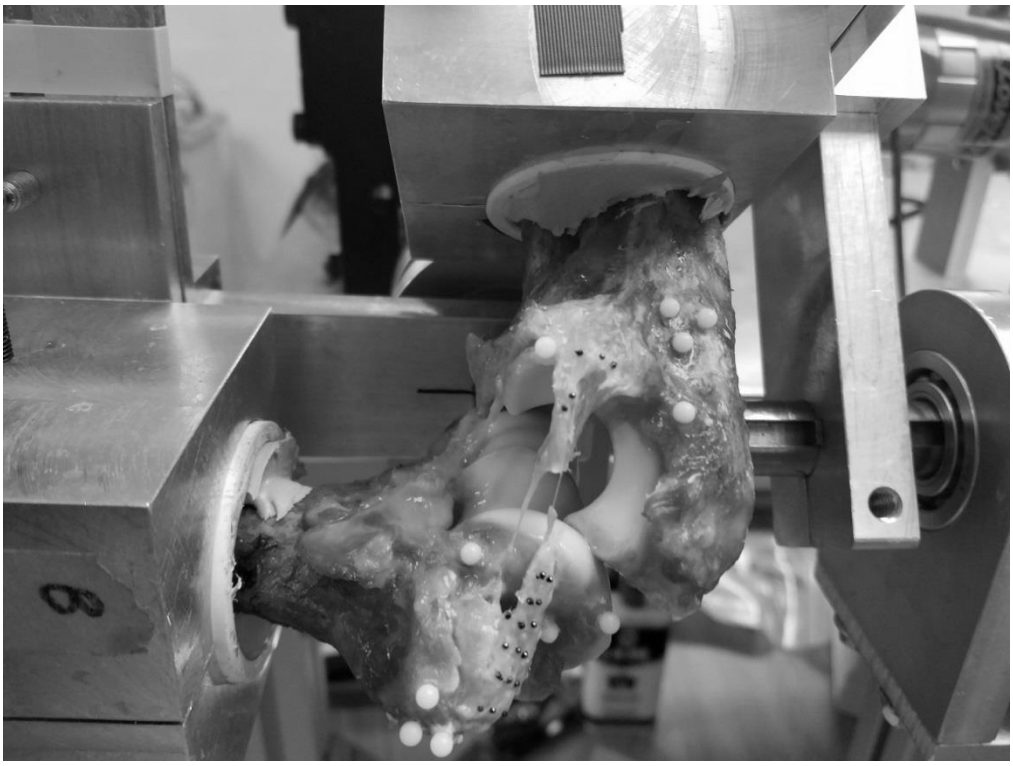

Figure 28: Failure of Arbitrary Specimen Tested in Valgus Cycling

Each specimen was tested following the procedure described in 4.6.1 for the torque levels of 90% and 80% of $\mathbf{M_f}$. To track how the angle increased, a custom MATLAB script extracted the angular position values at the peak of each cycle. These values for the representative specimen are designated by the circular markers shown in Figure (29). Figure (30) shows a singular plot of these maximum values for one specimen tested at 90% and another specimen tested at 80% of their respective $\mathbf{M_f}$ magnitudes.

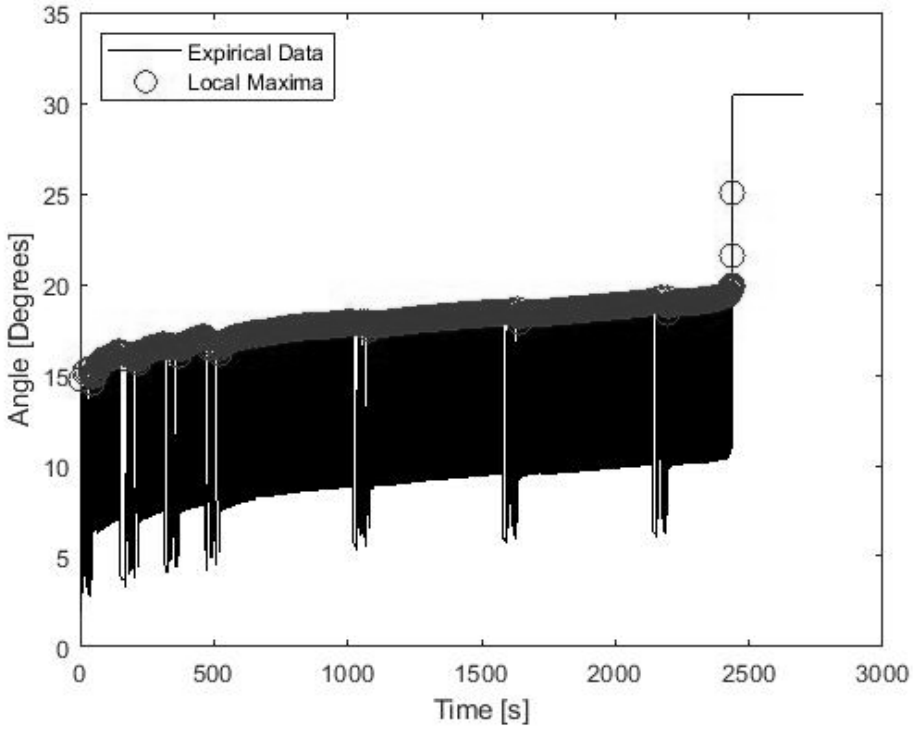

Figure 29: Designation of Peak Angles Achieved During Each Cycle

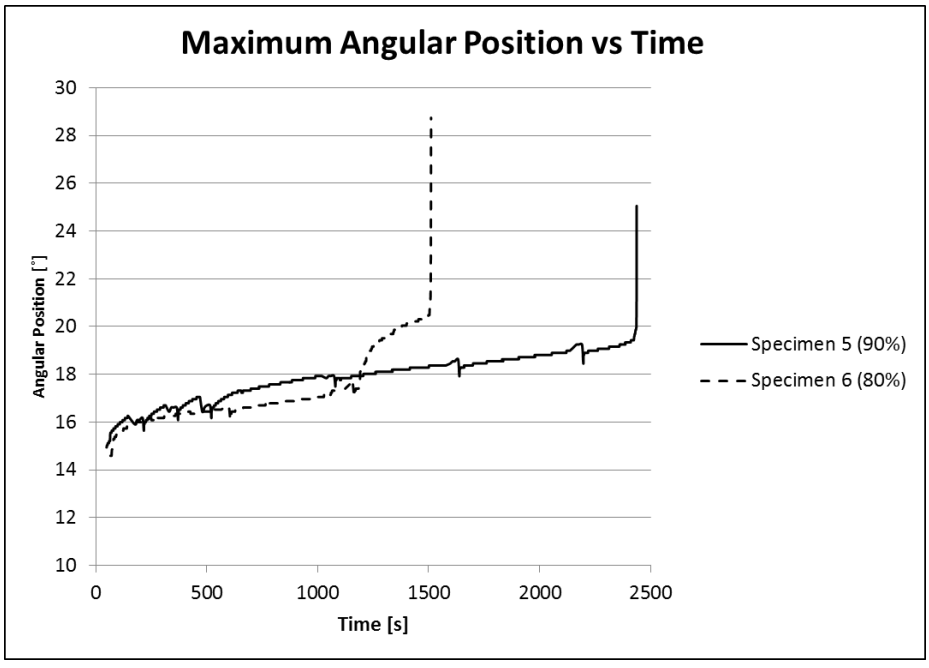

Figure 30: Peak Angular Positions for Representative Specimens Tested at 90% and 80% of M_f

The peak angle values were used to define a vector of m total elements, representing the values of these peak angles for each cycle. The vector was then normalized so that the starting angle was 0°. The amount of damage was then defined as the ratio of these normalized angular position values to the maximum angular position at failure θ_m. This produced a vector of damage values that increased nonlinearly from 0 (no damage) to 1 (failure). This process is depicted in Figure (31).

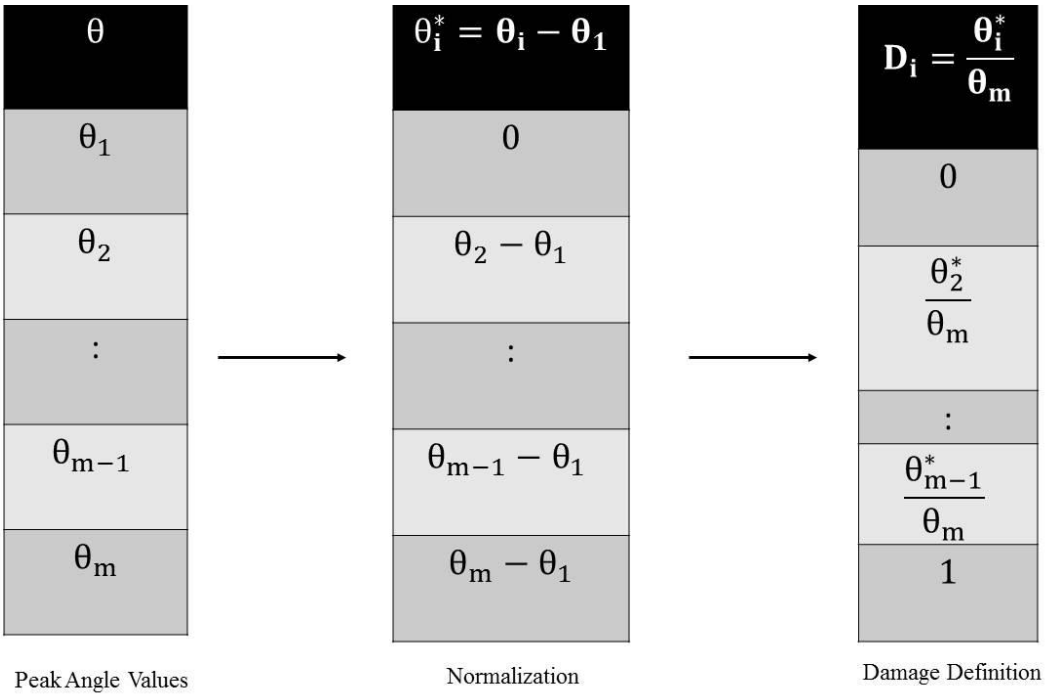

Figure 31: Process for Damage Definition Derived from Peak Angle Measurements

This process was carried out for the angular data set for each of the eleven specimens. For future finite element implementation, it is desired to have a single definition of damage that can

encapsulate a wide range of specimen behavior. For this, a custom MATLAB script was written to look at how the specimens incurred damage in an average sense.

Because each specimen failed at a different total number of cycles, the rate at which damage was incurred was different for each specimen. To normalize this for all specimens, the average damage was defined as the average amount of damage achieved at any designated fraction of the respective specimen-specific cycle life n_f. The percentages were obtained by dividing the current cycles n, by the total number of cycles to failure n_f for each individual specimen.

The results are represented in Figure (32). In Figure (32), every i^{th} value of D represents the average amount of damage incurred for that i^{th} fraction of the loading cycle.

$\frac{n_i}{n_f}$	D_i
$\frac{n_1}{n_f}$	D_1
$\frac{n_2}{n_f}$	D_2
:	:
$\frac{n_{m-1}}{n_f}$	D_{m-1}
$\frac{n_m}{n_f}$	D_m

Figure 32: Average Damage per Fraction of Fatigue Life Cycles

The results for these average damage calculations taken at every 5% of cyclic life completion ($n/n_f = 0.05$) is presented in Figure (33).

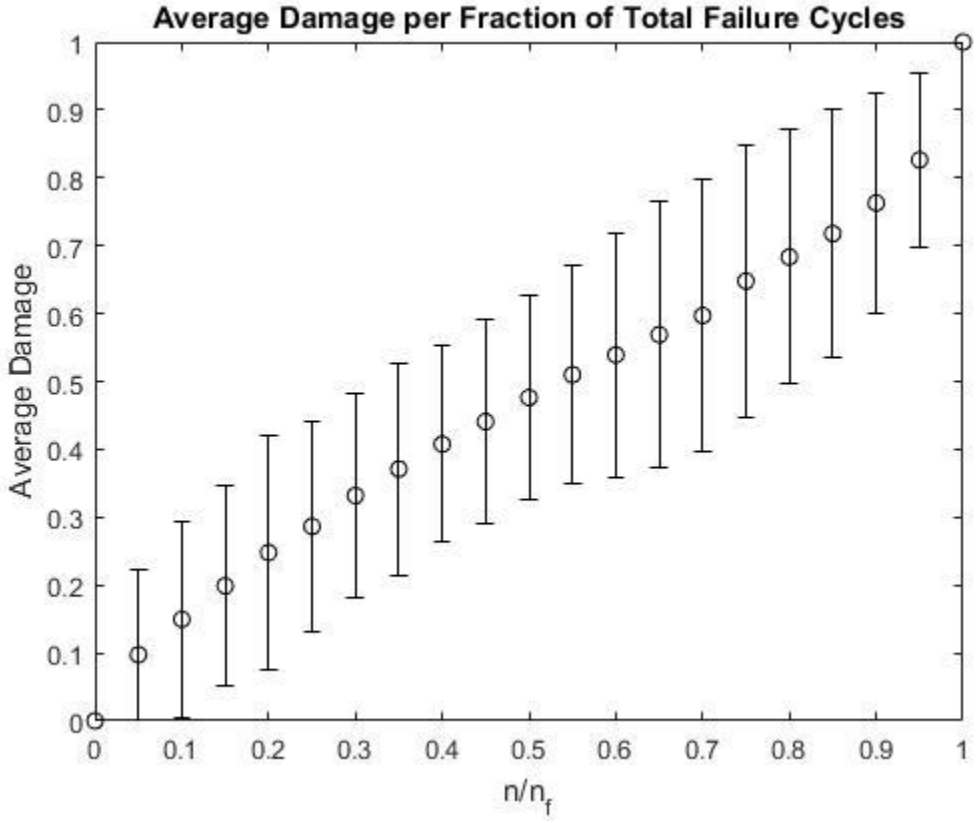

Figure 33: Results for Average Damage Incurred at Every 5% of n_f

A cubic curve fit using nonlinear optimization was applied to gain a functional form for the dependence of average damage on total cycle percentage, $D\left(\frac{n}{n_f}\right)$ (Equation 4-2), where A, B, C and E are constants to be determined. A cubic function was chosen because the damage accretion function is known to be constantly increasing and there may be multiple points of inflection displayed within the data that need to be captured. The optimization was performed with two constraints (Equations 4-3 – 4-4). These enforce that the amount of damage is equal to

zero when no cycles have been performed and is equal to one when 100% of the loading cycle has completed. Figure (34) shows the quality of the fit for the experimental data with the damage accretion function.

$$D\left(\frac{n}{n_f}\right) = A\left(\frac{n}{n_f}\right)^3 + B\left(\frac{n}{n_f^2}\right)^2 + C\left(\frac{n}{n_f}\right) + E \text{.....[4-2]}$$

$$D\left(\frac{n}{n_f} = 0\right) = 0 \text{.....[4-3]}$$

$$D\left(\frac{n}{n_f} = 1\right) = 1 \text{.....[4-4]}$$

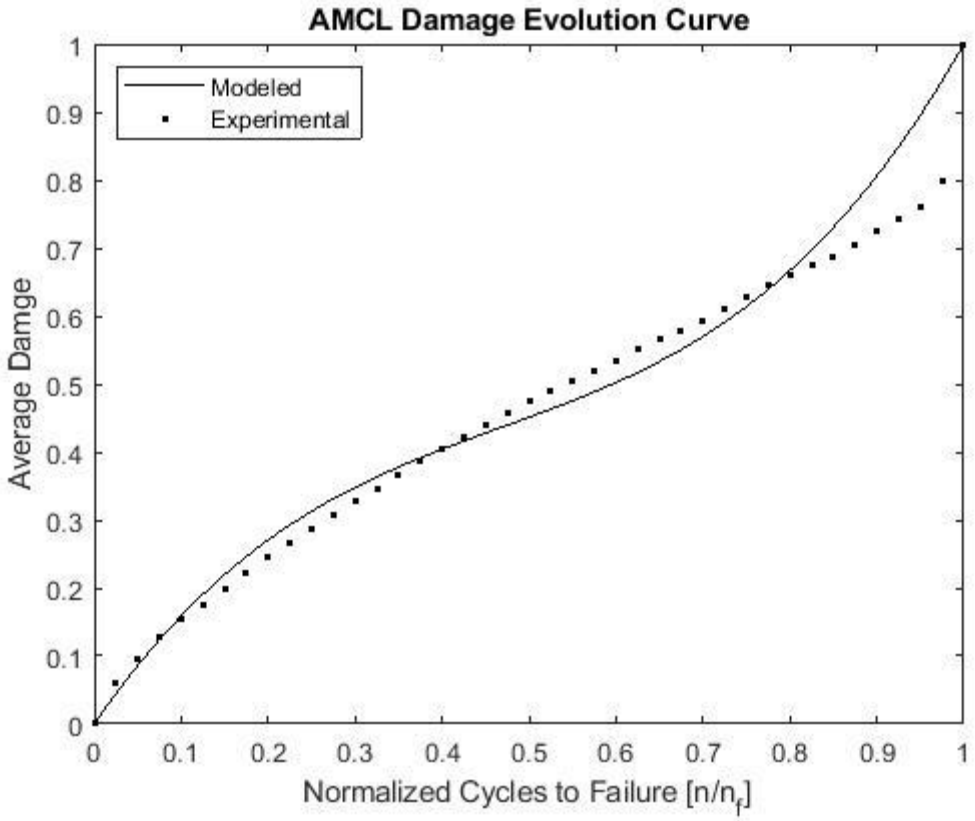

Figure 34: Cubic Curve Fit of Average Damage Data

Because the domain of a cubic function is infinite, a piecewise set of boundary conditions needed to be enforced to ensure that the damage function did not extend beyond the regions of no damage $\left(\frac{n}{n_f} = 0\right)$ and failure $\left(\frac{n}{n_f} = 1\right)$. This resulted in the finalized form of the damage function given by the piecewise relation of Equation (4-5).

$$D\left(\frac{n}{n_f}\right) = \begin{cases} 0 & \frac{n}{n_f} = 0 \\ A\left(\frac{n}{n_f}\right)^3 + B\left(\frac{n}{n_f}\right)^2 + C\left(\frac{n}{n_f}\right) + E & 0 < \frac{n}{n_f} < 1 \\ 1 & \frac{n}{n_f} = 1 \end{cases} \quad \text{.....[4-5]}$$

Figure (35) shows the finalized damage accretion function $D\left(\frac{n}{n_f}\right)$, describing the average damage incurred per fraction of cycle life completed for the eleven tested specimens.

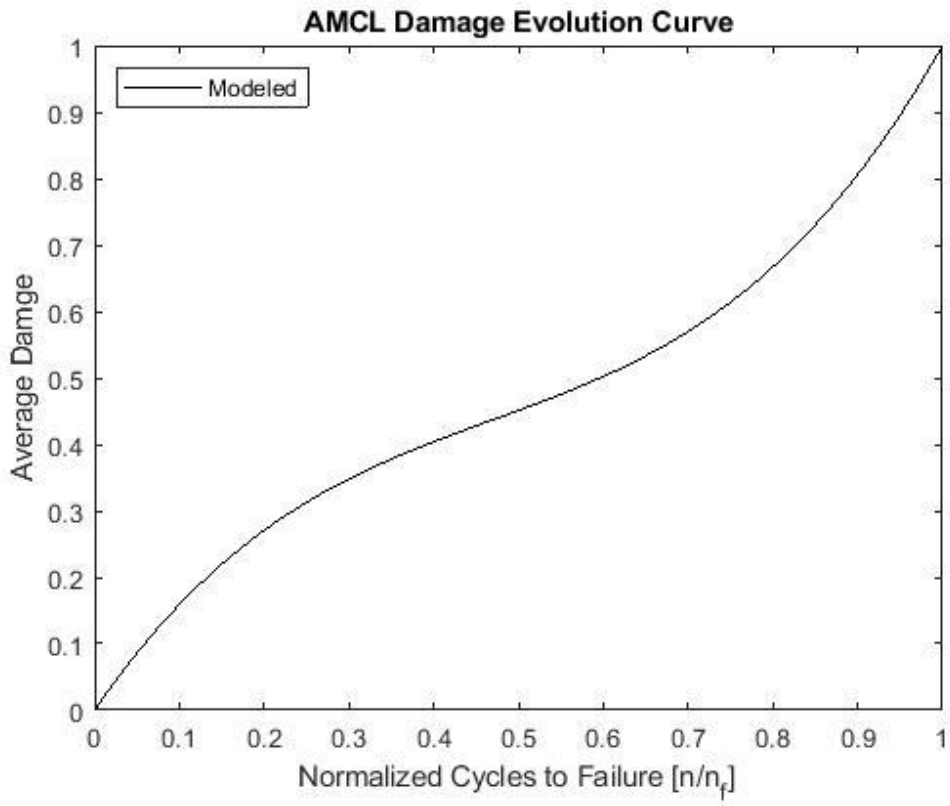

Figure 35: Nonlinear Average Damage Accretion Function for the AMCL Tested in Cyclic Valgus Loading

This was a critical step in the work, as previous damage evolution curves for cyclic fatigue have been assumed linear, as in Equation (3-24), where an equivalent amount of damage is accumulated after each cycle. This is the first nonlinear damage evolution model developed from empirical measurement for the elbow AMCL. With the nonlinear damage characteristic defined, the deformation data of the two experiments needed to be analyzed to define the relationship between ligament stress and stretch.

4.7 Calculation of Stretch (Processing of Elastic Testing Data)

The camera footage for the elastic testing was imported into a motion tracking software package, Spicatech (Spica Technology Corp., Kihei, HI), where the 3D Cartesian coordinates of each marker (mm) were output for each frame of the recording. For each video frame, the distance between each of the markers in a single column (Figure 36), was calculated using the square root of the sum of the squares of the coordinate differences (Equation 4-6). The sum of these values for each pair of adjacent markers gave the total length of the ligament for that frame (Equation 4-7).

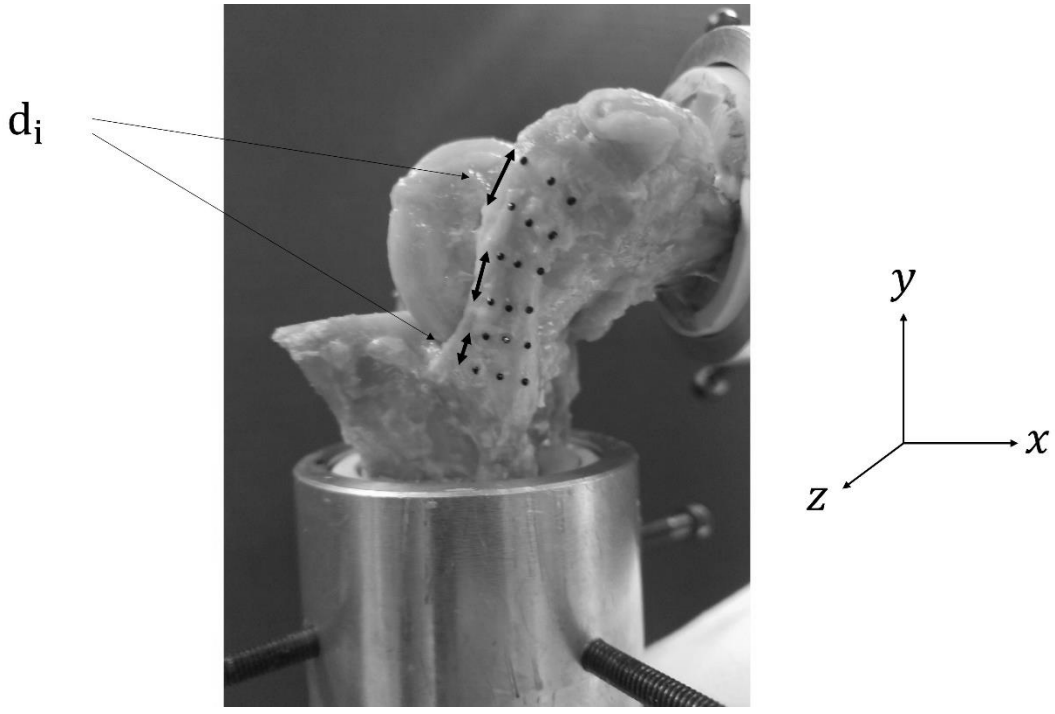

Figure 36: Distance Between Adjacent Markers Along AMCL

$$d_i = \sqrt{(x_i - x_{i-1})^2 + (y_i - y_{i-1})^2 + (z_i - z_{i-1})^2} \text{.....[4-6]}$$

$$L_k = \sum_{i=1}^{n-1} d_i \text{.....[4-7]}$$

In Equation (4-6), d_i was the distance between two adjacent markers; x_i, y_i and z_i were the Cartesian coordinates of the i^{th} marker. In Equation (4-7), L_k was the total length of the ligament for the k^{th} frame and n was the total number of markers along the length of one band. The stretch of the ligament was given by the ratio of the current length to the reference length (Equation 4-8).

$$\lambda_k = \frac{L_k}{L_o} \text{.....[4-8]}$$

In Equation (4-8), λ_k was the current stretch of the ligament, L_k was the current total length of the ligament, L_o was the initial/reference length of the ligament. The ligament slack is a length of the ligament that can bear no load. To incorporate this laxity into the stretch measurements, the magnitude of the slack L_s^{α} , was measured and subtracted from the initial reference length of the ligament. This resulted in an adjusted stretch value (Equation 4-9).

$$\lambda_k' = \frac{L_k}{L_o - L_s^{\alpha}} \text{.....[4-9]}$$

In Equation (4-9), λ_k' was the adjusted stretch level and L_s^{α} was the measured value of slack at flexion angle α.

4.8 Constitutive Modeling of Elastic Behavior

4.8.1 Deformation

Derivation of an appropriate constitutive model depends on the definition of the deformation being studied. In a theoretical framework, this deformation definition can be formed through the deformation gradient, **F**. Classic force-deformation tests of biological tissues are performed uniaxially or biaxially, where at least one component of the applied load is coincident with a principal direction of the material. In this case, the deformation gradient tensor is given by a diagonal matrix (Equation 4-10), where the components are the stretches in the principal directions, λ_j with $j \in (1,2,3)$.

$$\mathbf{F} = \begin{bmatrix} \lambda_1 & 0 & 0 \\ 0 & \lambda_2 & 0 \\ 0 & 0 & \lambda_3 \end{bmatrix} \text{.....[4-10]}$$

The assumption of incompressibility imposes that the determinant of this tensor be equivalent to one. This leads to the requirement of Equation (4-11).

$$\lambda_1\lambda_2\lambda_3=1 \text{.....[4-11]}$$

Using the simplification for the pure uniaxial elongation; $\lambda_1 = \lambda \text{ and } \lambda_2 = \lambda_3$, then **F** is given by Equation (4-12).

$$\mathbf{F} = \begin{bmatrix} \lambda & 0 & 0 \\ 0 & \frac{1}{\sqrt{\lambda}} & 0 \\ 0 & 0 & \frac{1}{\sqrt{\lambda}} \end{bmatrix} \text{.....[4-12]}$$

The right Cauchy-Green stretch tensor, **C**, is then given by Equation (4-13).

$$\mathbf{C} = \mathbf{F^T F} = \begin{bmatrix} \lambda^2 & 0 & 0 \\ 0 & \frac{1}{\lambda} & 0 \\ 0 & 0 & \frac{1}{\lambda} \end{bmatrix} \text{.....[4-13]}$$

The left Cauchy-Green stretch tensor, **B**, is then given by Equation (4-14).

$$\mathbf{B} = \mathbf{F F}^{\mathrm{T}} = \begin{bmatrix} \lambda^2 & 0 & 0 \\ 0 & \frac{1}{\lambda} & 0 \\ 0 & 0 & \frac{1}{\lambda} \end{bmatrix} \text{.....[4-14]}$$

These three second order tensors characterize the deformation of the AMCL. The right and left Cauchy-Green stretch tensors will be used to construct the constitutive model.

4.8.2 Strain Energy Function

The constitutive modeling began with the selection of a hyperelastic constitutive model (summarized in sections 3.2.2 - 3.2.4) that is commonly used for biological tissues. This model would be dependent only on the principal strain invariants.

Choice of which invariants to include in the strain energy function depended on what influences needed to be considered. When considering effects from the ground substance, invariants I_1 and I_2 need to be included. The contribution of the fibers to the mechanical response is accounted for within I_4. I_3 becomes equal to one due to incompressibility. With these factors considered, the strain energy function had a dependence on three invariants. The strain energy for the AMCL would then be represented by Equation (3-10).

The functional forms of $W_{\text{isotropic}}$ and $W_{\text{anisotropic}}$ are typically chosen to be given by well-known strain energy functions. For this work, we employ the transversely isotropic Mooney-Rivlin model (Equation 4-15), where C_1, C_2, C_3 and C_4 are material constants to be determined.

$$W_{\text{AMCL}}(I_1, I_2, I_4) = C_1(I_1 - 3) + C_2(I_2 - 3) + C_3 e^{C_4(I_4-1)^2} \quad \text{.....[4-15]}$$

4.8.3 Stress

The second Piola-Kirchoff stress **S**, is given by Equation (4-16).

$$\mathbf{S} = \frac{\partial W_b}{\partial \mathbf{C}} = \sum_{q=1,2,4} \frac{\partial W_b}{\partial I_q} \frac{\partial I_q}{\partial \mathbf{C}} \text{.....[4-16]}$$

Equation (56), is derived using the chain rule. Forming the second Piola-Kirchoff stress tensor in this manner ensures consistency with the equations of equilibrium and the Clausius-Dunheim inequality. Applying Equation (4-16) to Equation (4-15) gives Equation (4-17).

$$\mathbf{S} = C_1 \frac{\partial I_1}{\partial \mathbf{C}} + C_2 \frac{\partial I_2}{\partial \mathbf{C}} + C_3 C_4 e^{C_4(I_4-1)^2} (I_4 - 1) \frac{\partial I_4}{\partial \mathbf{C}} \text{.....[4-17}$$

Performing the differentiation of Equation (4-17) results in Equation (4-18), where **I** is the second order identity tensor.

$$\mathbf{S} = C_1\mathbf{I} + C_2[2I_1\mathbf{I} + 2\mathbf{C}] + C_3C_4e^{C_4(I_4-1)^2}(I_4 - 1)\mathbf{a} \otimes \mathbf{a} \text{.....[4-18]}$$

For simulation purposes, it is preferred to give the stress in the current configuration. The second Piola-Kirchoff stress, which is defined in the reference configuration, can be converted to the current configuration in the form of the Cauchy stress **σ**, by using a push forward operation (Equation 4-19). This resulted in the final form of the Cauchy stress given by Equation (4-20), where p is a Lagrange multiplier representing a hydrostatic pressure.

$$\boldsymbol{\sigma} = \mathbf{F}\mathbf{S}_\mathbf{b}\mathbf{F}^\mathbf{T} \text{.....[4-19]}$$

$$\boldsymbol{\sigma} = C_1\mathbf{B} + C_2[2I_1\mathbf{B} + 2\mathbf{B}\mathbf{B}] + C_3C_4e^{C_4(I_4-1)^2}(I_4 - 1)\mathbf{F}\mathbf{a} \otimes \mathbf{a}\mathbf{F}^\mathbf{T} - p\mathbf{I} \text{.....[4-20]}$$

4.8.4 Fiber Direction

Previous studies have shown that the direction of the fibers of the AMCL remain relatively straight during loading[80]. For the twenty-two specimens tested, measurements were taken of width and thickness of the distal and proximal ends, as well as the overall length using calipers.

These measurements, presented in Figure (37), show that the average joint line (distal) width is larger than the average proximal width.

In the absence of technology for micro-level fiber visualization, this knowledge was used to presume what the general alignment of the fibers should be. Assuming minimal discontinuities, the fibers would be relatively straight near the mid-substance and parallel to the anterior and posterior boundaries (Figure 38). Near the wider region of the joint line, the fibers would 'fan' out. This assumption assumes no broken fibers at the boundaries.

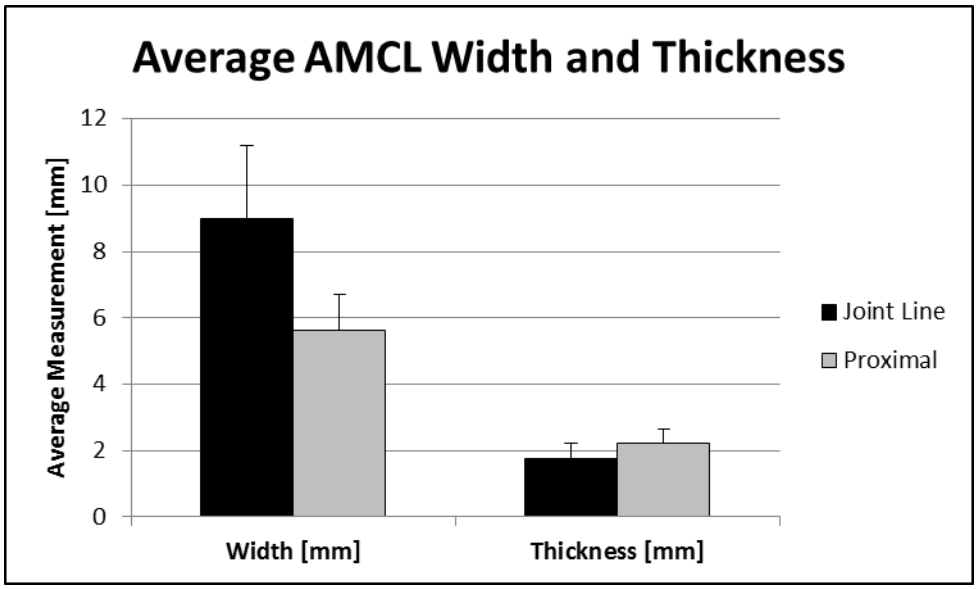

Figure 37: Average Distal and Proximal Width and Thickness Results for the 22 Specimens

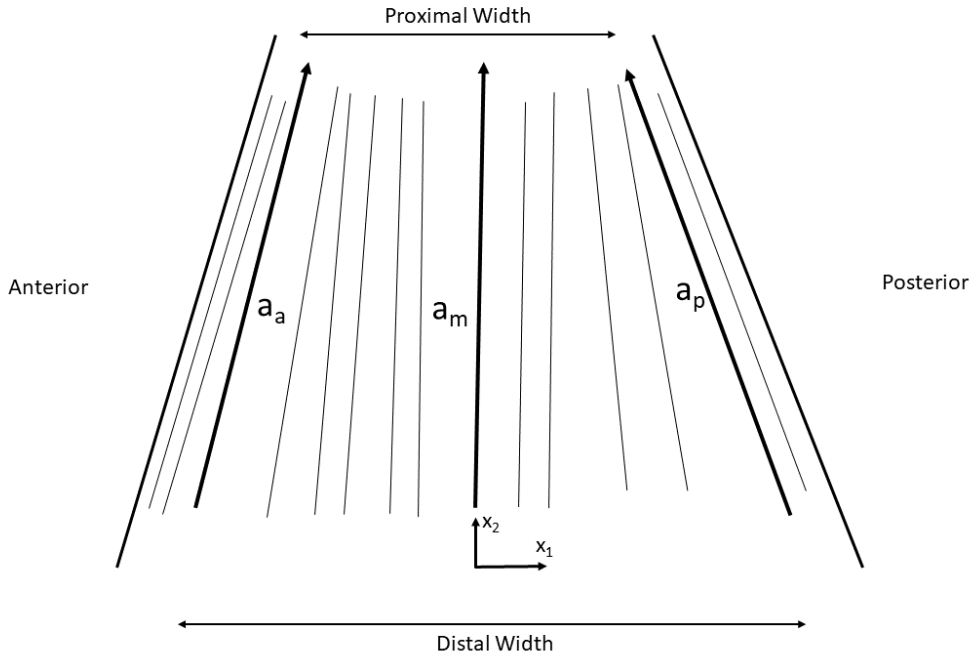

Figure 38: Schemetic of Theoretical Idealized AMCL Fiber Alignment

The visualization of Figure (38) leads to the formulation of some basic direction vectors for the fibers given by Equations (4-21 – 4-23).

$$\mathbf{a_a} = \frac{1}{\sqrt{\frac{(D_w - P_w)^2}{4} + L^2}}\left[\frac{|D_w - P_w|}{2}\mathbf{x_1} + L\mathbf{x_2}\right} \quad \text{[4-21]}$$

$$\mathbf{a_p} = \frac{1}{\sqrt{\frac{(D_w - P_w)^2}{4} + L^2}}\left[-\frac{|D_w - P_w|}{2}\mathbf{x_1} + L\mathbf{x_2}\right} \quad \text{[4-22]}$$

$$\mathbf{a_m} = \mathbf{x_2} \quad \text{[4-23]}$$

In Equations (4-21 – 4-23), D_w is the average distal width, P_w is the average proximal width and L is the average length of the ligament. If $\mathbf{a_b}$ is the mean fiber direction vector for a given band b, and it has components a_b^i, with i = [1,3], then the strain invariant characterizing fiber direction I_4, is given by Equations (4-24 – 4-25).

$$I_4 = \begin{bmatrix} a_b^1 \\ a_b^2 \\ a_b^3 \end{bmatrix}^T \begin{bmatrix} \lambda^2 & 0 & 0 \\ 0 & \frac{1}{\lambda} & 0 \\ 0 & 0 & \frac{1}{\lambda} \end{bmatrix} \begin{bmatrix} a_b^1 \\ a_b^2 \\ a_b^3 \end{bmatrix} \text{.....[4-24]}$$

$$I_4 = a_b^1(a_b^1\lambda^2) + a_b^2\left(a_b^2\frac{1}{\lambda}\right) + a_b^3\left(a_b^3\frac{1}{\lambda}\right) \text{.....[4-25]}$$

It can be seen from Equations (4-24 – 4-25), that if the distal and proximal widths are assumed equivalent, then all fibers will be aligned with the centroidal long axis of the ligament and I_4 would simplify to the form of Equation (4-26). This was the form of I_4 used in the final calculations.

$$I_4 = (a_b^1)^2\lambda^2 \text{.....[4-26]}$$

4.8.5 Stress in the Primary Loading Direction

The component of the Cauchy stress in the primary loading direction is often the component of most interest. This is because the loading direction is often chosen to be the fiber

direction, meaning that the ligament is undergoing deformation in the preferred or 'structurally strongest' direction. This component of the stress is given by Equations (4-27 – 4-28).

$$\sigma_{11} = C_1\lambda^2 + 4C_2(\lambda^4 + \lambda) + \sigma_{11}^f - p \quad \text{.....[4-27]}$$

where,

$$\sigma_{11}^f = \begin{cases} 0 & \text{if} \quad \lambda < \lambda_s \\ C_3C_4e^{C_4(I_k-1)^2}(I_k-1)\lambda^2 & \text{if} \quad \lambda \geq \lambda_s \end{cases} \text{.....[4-28]}$$

In Equation (4-27), σ_{11}^f is the fiber stress and λ_s is the slack-stretch which quantifies the amount of slack in the ligament. For stretches less than λ_s, the ligament can bear no load and the stress is zero.

The Lagrange multiplier for the hydrostatic pressure can be determined by making a plane stress assumption ($\sigma_{33} = 0$). This assumption is based on the fact that the length of the ligament is significantly greater than the ligament thickness, as shown by the results of Figure (37) and the illustration of Figure (39). The hydrostatic pressure was then given by Equation (4-29) and the finalized stress in the primary loading direction was given by Equation (4-30).

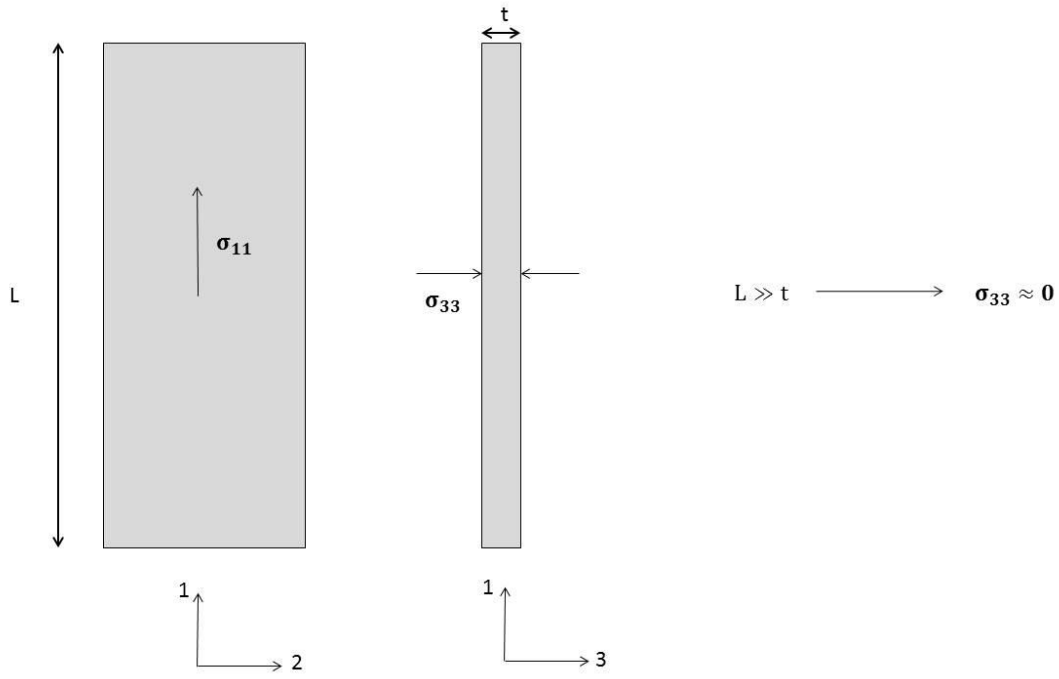

Figure 39: Ligament Width and Thickness Depiction for Assumption of Plane Stress

$$p = C_1\left(\frac{1}{\lambda}\right) + C_2\left[2I_1\left(\frac{1}{\lambda}\right) + \frac{2}{\lambda^2}\right] \text{.....[4-29]}$$

$$\sigma_{11} = C_1\left(\lambda^2 - \frac{1}{\lambda}\right) + C_2\left(4\lambda^4 + 2\lambda - \frac{6}{\lambda^2}\right) + \sigma_{11}^{f}\left(\lambda^2 - \frac{1}{\lambda}\right) \text{.....[4-30]}$$

4.9 MATLAB Routine

With the general form of the elastic constitutive model formulated and the mechanical testing of the specimen completed, a MATLAB routine was generated to inform the constitutive

model with experimental data. The result of the MATLAB routine would be a fully-formed elastic constitutive model, representing the mechanical behavior of the healthy AMCL.

4.9.1 Constitutive Model Implementation

In Equation (4-30). there are four unknown constants, $C_1 - C_4$. Using a custom MATLAB script, these constants were determined through non-linear regression. The regression was accomplished using the built-in function 'fmincon'. The MATLAB routine started with the organization of the stretch data for the three bands taken from the elastic test. These were organized into three columns, along with the force data (Table 1). The force data was then converted into stress data by dividing each force measurement by the nominal cross-sectional area of the ligament (width*thickness), which was measured prior to each test using calipers.

Table 1: Stress and Stretch Vectors for AMCL Bands

$\boldsymbol{\sigma}$	$\boldsymbol{\lambda_a}$	$\boldsymbol{\lambda_m}$	$\boldsymbol{\lambda_p}$
σ_1	λ_{a1}	λ_{m1}	λ_{p1}
σ_2	λ_{a2}	λ_{m2}	λ_{p2}
:	:	:	:
σ_n	λ_{an}	λ_{mn}	λ_{pn}

The stretch data from the middle band was chosen to represent the stretch of the AMCL. This was because the middle band was judged to be the most 'position-neutral' band, displaying

less variability in slack with respect to flexion angle, as compared to the anterior and posterior bands, respectively. The total stress data and middle band stretch data were imported into MATLAB. The regression of the four constants resulting from the constitutive model given by Equation (70) finalized the formulation of the elastic constitutive model for the AMCL. A representation of this model is given in Figure (40) which shows the results for specimen 1 at 90˚ of flexion.

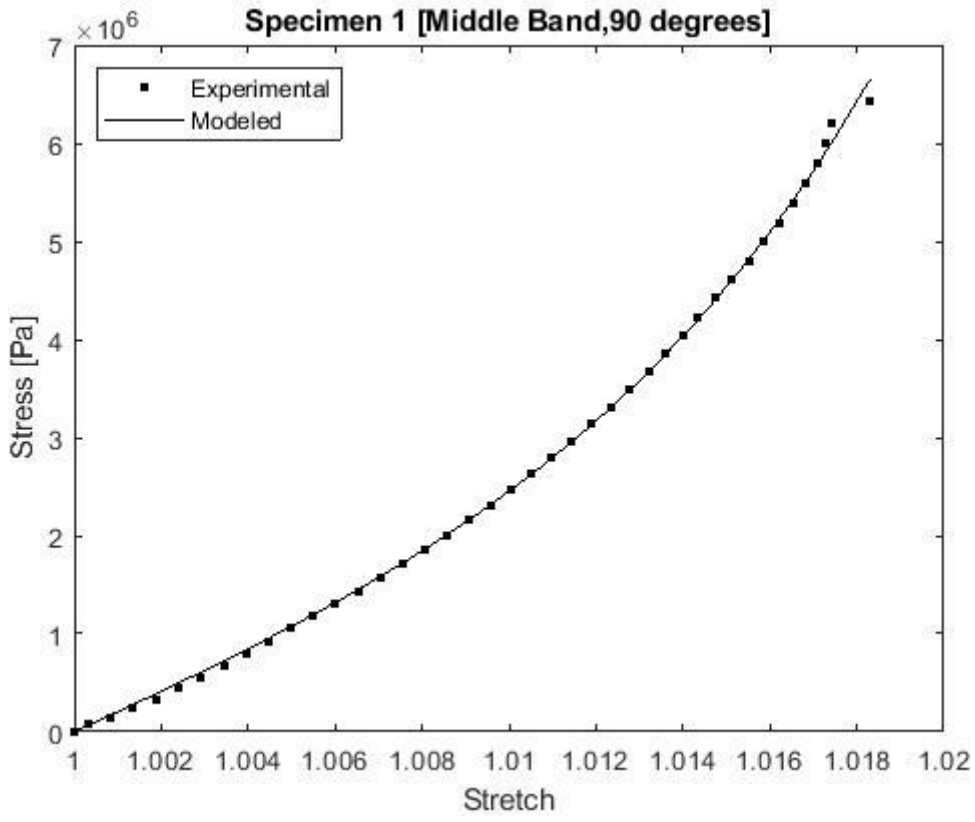

Figure 40: Curve Fit of Hyperelastic Transversely Isotropic Constitutive Model to Experimental Data

4.10 Constitutive Modeling of Inelastic Behavior (Fatigue Effect)

In modeling the gradual reduction of stiffness due to the fatigue damage, two factors are necessary. These are the damage criteria and the damage function, which are summarized in section 3.2.2. In the finite element formulation, the damage criteria is evaluated at each element. If this condition is met, then the fatigue damage proceeds and the stress of the element degrades as given by Equation (4-31), where D(n) is the damage function given as a function of the number of cycles and σ^{o} is the elastic undamaged stress.

$$\sigma = (1 - D(n))\sigma^{o} \quad \text{.....[4-31]}$$

The function D(n) describes how the damage evolves from the cycling at a specific load level. Although the cycling may be performed at the same magnitude, the stress in each element may be different. Therefore, D(n) needs to be properly adjusted based on the value of the maximum strain Ξ_{max}, in the element.

Previous works have assumed a linear fatigue damage function[64, 65] such as $D^{*}(n)$ (Equation 4-32), wherein the damage is accumulated equally for all elements, given that the total number of cycles to failure n_{tot} is known and given as a function of the maximum equivalent strain Ξ_{max}.

$$D^{*}(n) = \frac{n}{n_{tot}(\Xi_{max})} \quad \text{.....[4-32]}$$

In this formulation Ξ_{max} is evaluated, which determines the value of n_{tot} and sets the slope of the linear damage function $D^*(n)$, which gradually increases from 0 to 1, as n increases from 0 to n_{tot}.

In the nonlinear formulation, Ξ_{max} is evaluated similarly, which also determines the value of n_{tot}. This value of n_{tot} then 'selects' the appropriate nonlinear damage function D(n). These nonlinear functions are those determined by the inelastic fatigue tests performed at varying valgus stress levels. These functions range from $D(n) = 1$ at σ_{max}, where failure occurs instantly with one cycle, to $D(n) = 0$ at σ_{min}, where failure will not occur for theoretically infinite number of cycles. A representation for these functions superimposed along the representative fatigue life curve is given in Figure (41).

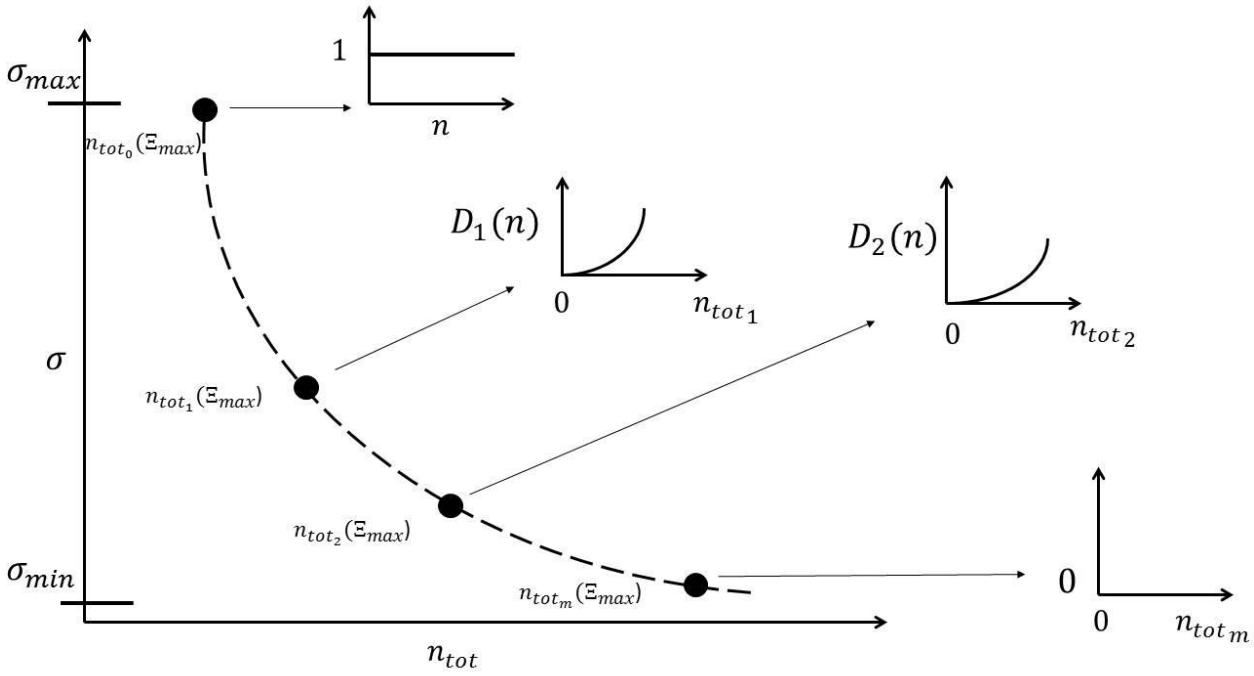

Figure 41: Representation of Nonlinear Damage Accumulation Curves Dependent on Fatigue Life

The representation of this idea is encapsulated within the non-dimensional form of the damage function $D\left(\frac{n}{n_f}\right)$ given in Figure (35). The abscissa of this function is set from 0 to 1. However, once n_f is known from the loading, the abscissa then scales from 0 to n_f. This allows for the modeling of any elbow specimen with an arbitrarily unique value of n_{tot}, thus creating the series of uniquely defined nonlinear damage functions along the fatigue-life curve represented in Figure (41).

4.11 Interpolation and Extrapolation

The construction of the entire fatigue life curve for the AMCL up to a theoretical fatigue life limit would require extensive testing. However, the total curve is necessary to complete the definition of the damage model. To form the complete fatigue life curve, the three experimental data points for the average cycles to failure at 100%, 90% and 80% (Figure 42) of the scaled valgus fatigue moment $\mathbf{M_f}$, were used to fit a complete model. For illustrative purposes, the intermediate data for 4 specimens is presented.

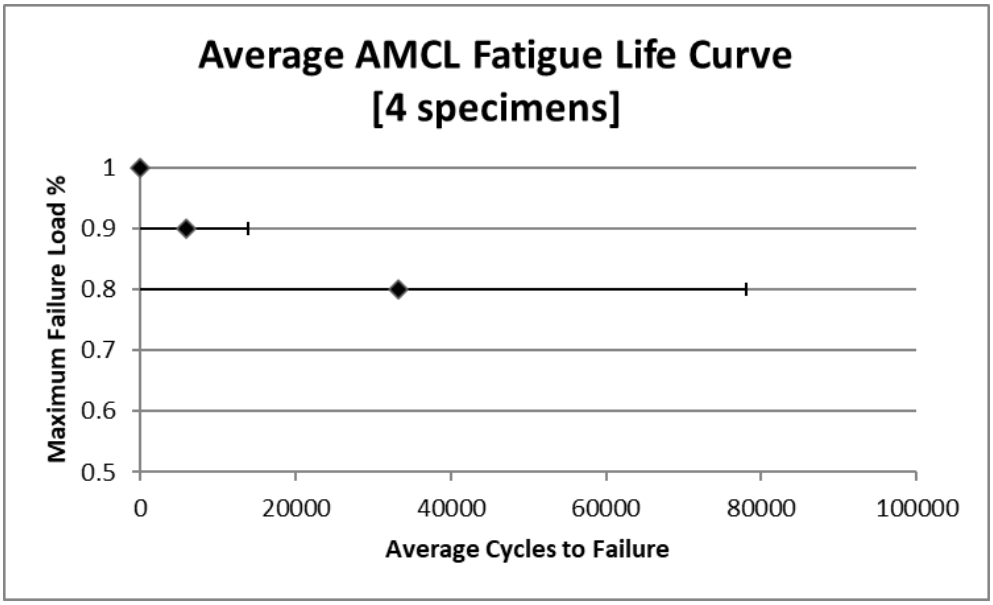

Figure 42: Non-Dimensional Average AMCL Fatigue Life Curve for Valgus Cycling [4 specimens]

These three points were used in a MATLAB script to form a model of the fatigue life curve S(n), using nonlinear regression. The chosen functional form had to satisfy two criteria. The first was that the function had to be monotonically decreasing. The second was that the function needed to be continuous. To satisfy these criteria, an exponential decay equation was chosen to model the fatigue life curve. The general form of this equation is given by Equation (4-33).

$$S(n) = \beta e^{-\frac{\gamma}{r} n_f} \quad \text{[4-33]}$$

In Equation (73), β and γ are constants to be determined and r is a scaling parameter. This equation needed to satisfy one constraint given by Equation (74), which enforces that the cycles to failure when the load is at 100% of $\mathbf{M_f}$ is equal to one.

$$S(n_f = 1) = \beta e^{-\frac{\gamma}{r}} = 1 \quad \text{[4-34]}$$

The correlation of the model with the three experimental data points for 4 specimens is shown in Figure (43). The fatigue life curve up to an arbitrary asymptote is shown without the experimental data in Figure (44).

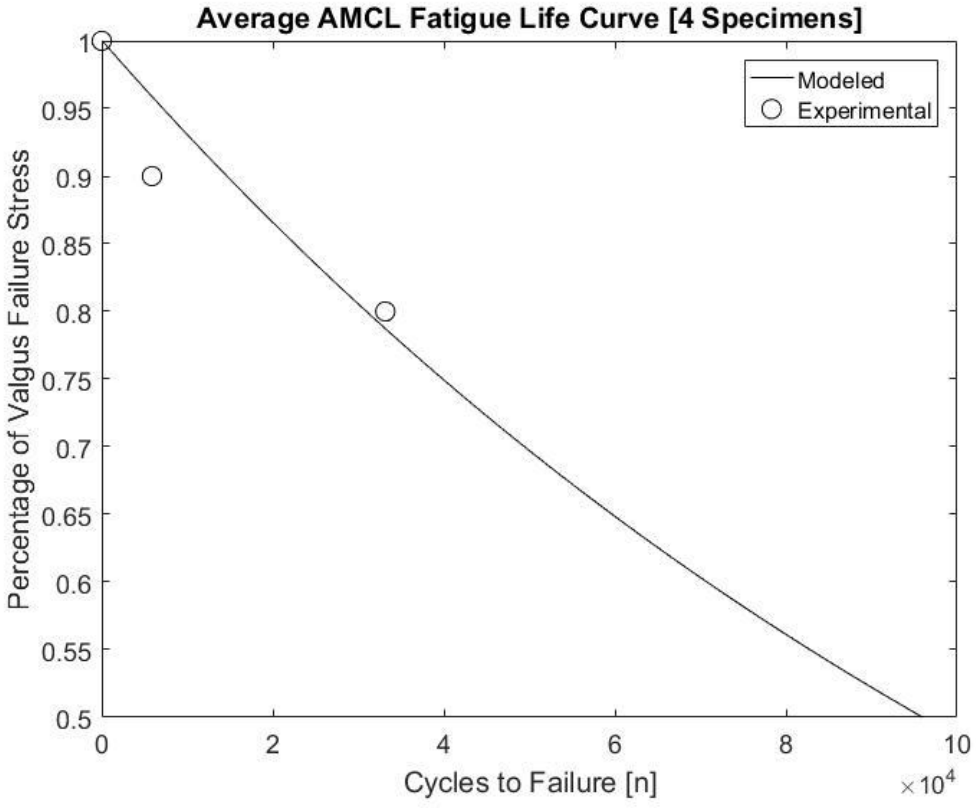

Figure 43: Correlation Between Experimental Average Fatigue Life Data and Exponential Decay Model for 4 Specimens

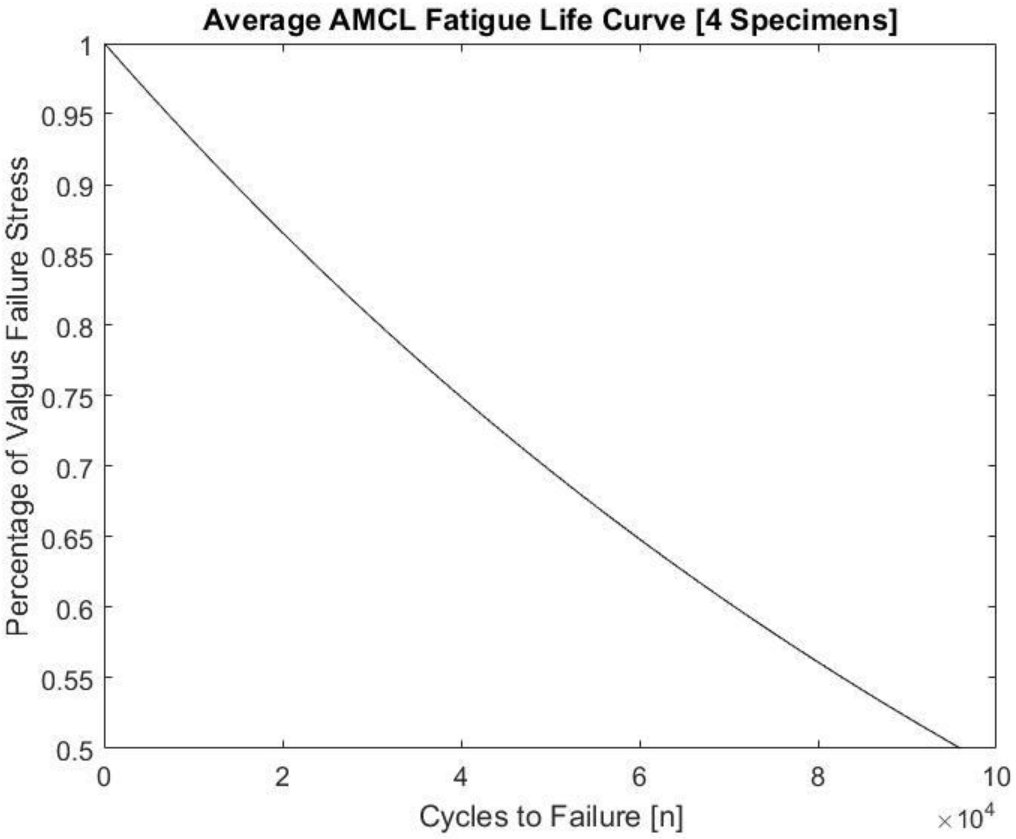

Figure 44: Non-Dimensional Modeled Average AMCL Fatigue Life Curve for Valgus Cycling [4 specimens]

4.12 Model Generation

There were three stages necessary for the development of the 3D elbow joint model. These stages were MRI imaging, segmentation and model smoothing. All of these processes were necessary in order to produce an anatomically accurate geometry of the elbow joint suitable for mechanical analyses.

4.12.1 MRI Imaging

To build the 3D model of the elbow joint and ligament, magnetic resonance imaging (MRI) scans were taken of a single elbow specimen. To take the scans, the specimen needed to be mounted in a stable position. Additionally, images were desired to be taken at four different flexion angles: 0º, 30º, 60º and 90º. To accommodate these conditions, a custom device was built in order to both secure the specimen and allow for flexion at the desired angles (Figure 45).

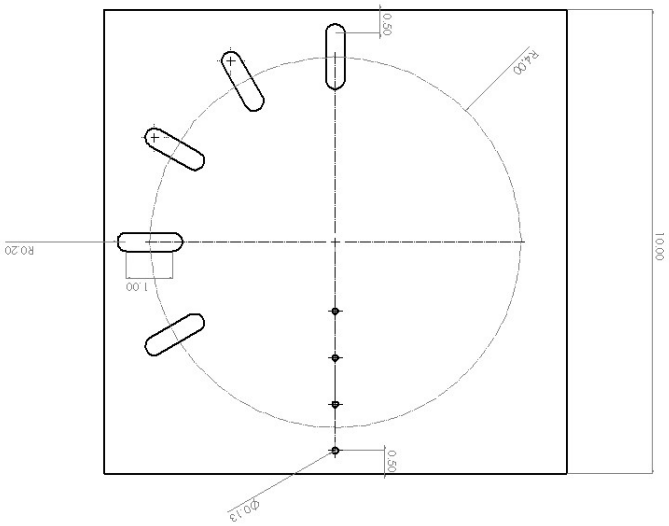

Figure 45: Custom Designed Elbow Mount for MRI Imaging

The custom mount of Figure (45) was designed and built in the machine shop of the Biomechanics Laboratory at Allegheny General Hospital. The mount was made of plexiglass. The dimensions in the figure are given in inches and were chosen to allow the mount to fit within a 27.5 cm diameter coil. The five slots were positioned at intervals of 30º and were the mechanism that allowed for the flexion of the specimen.

The specimen was centered at the midpoint of the mount. Two holes were drilled through the ulna and nylon screws were placed through the holes and into two of the four holes at the bottom of the mount. A single hole was drilled into the humerus and a threaded rod was placed through and into the top slot of the mount. With this, the specimen was securely fixed to the mount at full extension (0º flexion) .

The scans were taken in the radiology department at West Virginia University Hospital using a three Tesla, 27.5 cm diameter magnetic coil. The scans were taken using 2mm slices in a direction perpendicular to the ulna. The resulting images (Figure 46) were extracted and saved onto an external storage device as DICOM files.

Figure 46: Representative Elbow MRI Image

After the images at full extension were saved, the specimen and mount were taken out of the coil. By removing the threaded rod within the humerus out of the first slot and moving it to the next slot, the specimen was flexed to the next angle 30º. The specimen and mount were then

placed back within the coil and images were again taken at the new flexion angle. This process was repeated for the subsequent flexion angles of 60º and 90º.

4.12.2 Segmentation

The MRI DICOM files for each of the flexion angles were loaded into the image segmentation software MIMICs (Materialise, Plymouth, MI). For each image, there were several key constructs that needed to be identified and highlighted. These were the radius, ulna, humerus and AMCL.

From the lower-most image, as you move up along the ulna, the radius was the first significant landmark to come into view. It was followed into frame by the olecranon process of the proximal ulna. Both bones can be seen in Figure (47).

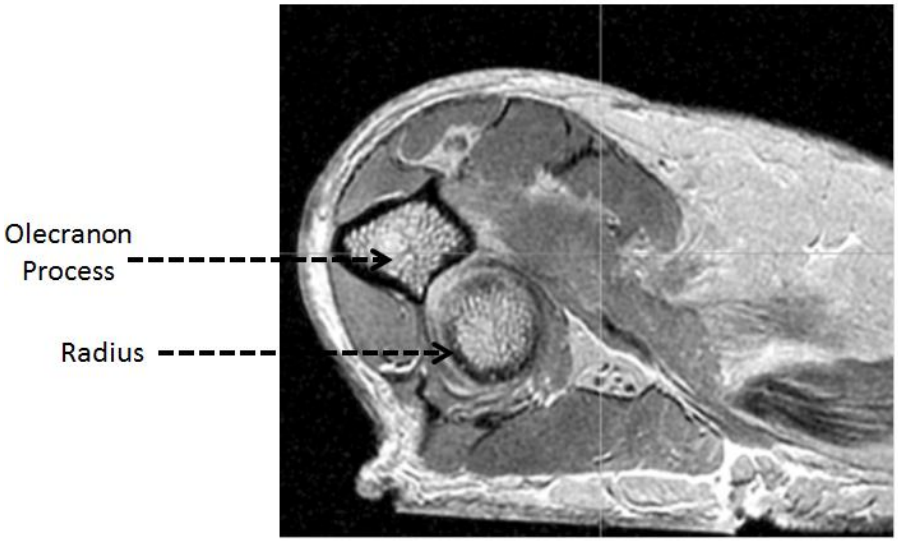

Figure 47: MRI Image (Olecranon Process and Radius)

Moving the frames further along the ulna, the radius began to disappear from view. The view continued to span the proximal ulna as the trochlear notch appeared, along with the capitellum of the distal humerus (Figure 48).

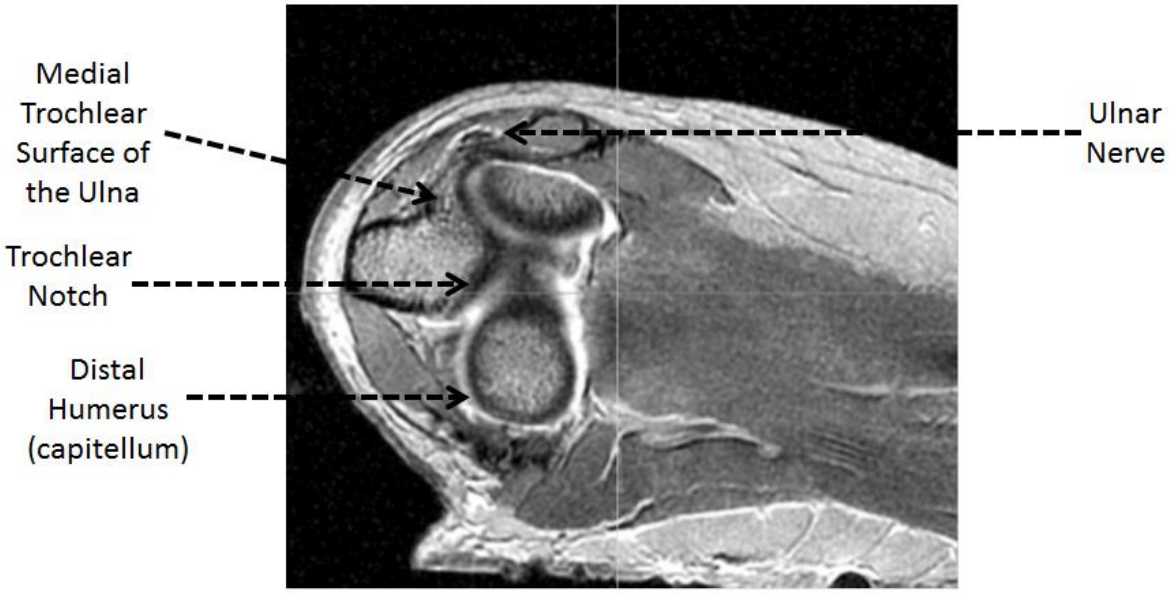

Figure 48: MRI Image (Distal Humerus, Ulnar Nerve, Trochlear Surface and Notch)

It was at this level of the image that the AMCL first started to appear. For consistency between angles, the same protocol was followed for finding the ligament. The appearance of the coronoid process was the first indicator, as this is one of the insertion sites of the ligament. Identification of the ulnar nerve followed, as the ligament is positioned underneath the nerve. Around this area, any tissue which displayed significantly darker color than the surrounding tissue was identified as the ligament and was traced out for the remainder of the images.

Moving further up the proximal ulna, the ligament continued to be traced out, along its length, as it steadily moved from the coronoid process to the medial epicondyle of the distal

humerus. The disappearance of the darker tissue and the visual of the olecranon fossa (Figure 49) were indicators that the entirety of the ligament had been traversed.

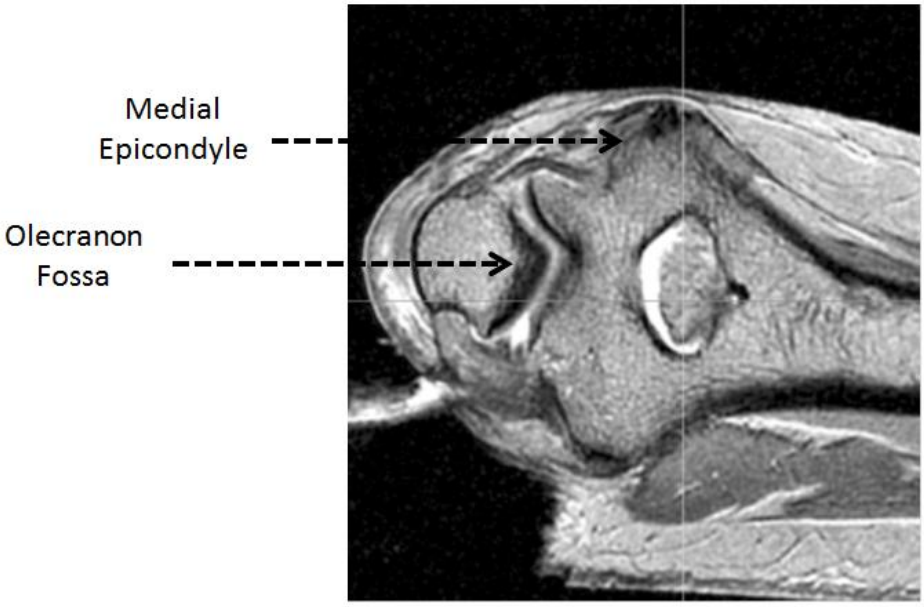

Figure 49: MRI Image (Medial Epicondyle and Olecranon Fossa)

Once the relevant structures had been identified, an initial rendering of the 3D model could be generated. This initial build was very jagged with rough surfaces, exaggerated peaks and various other miscellaneous imperfections (Figure 50).

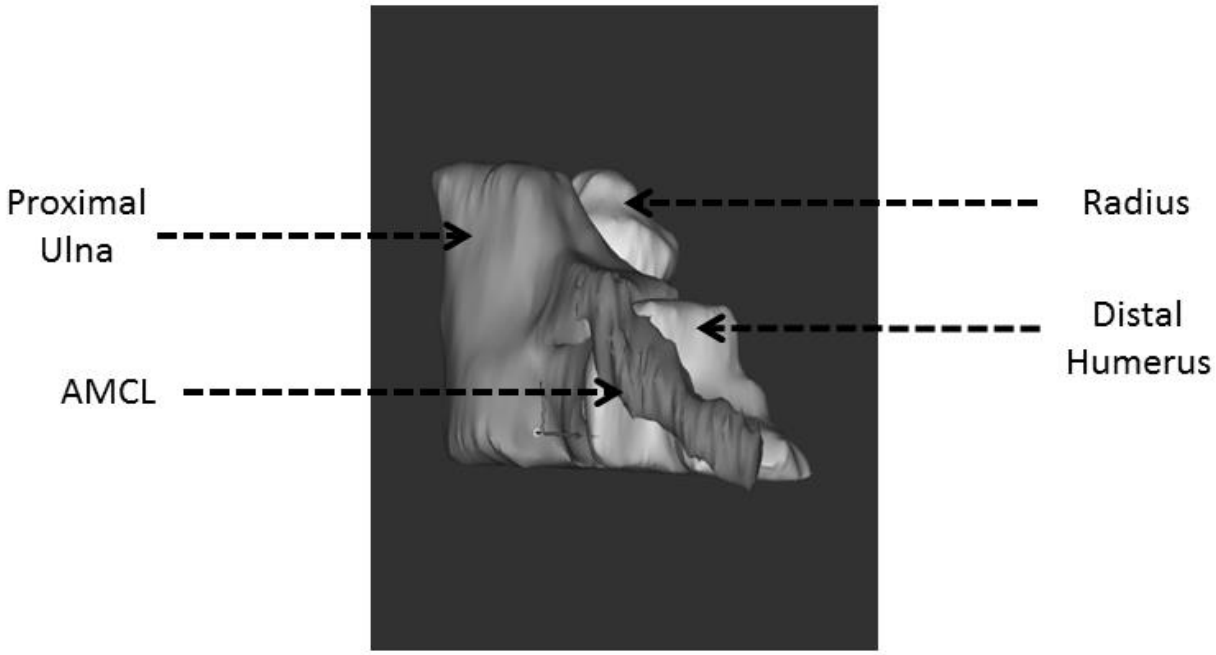

Figure 50: Initial Build of 3D Elbow Model

4.12.3 Smoothing

With the preliminary model of the elbow joint complete, the next step was to remove any and all anatomically incorrect features from the model. This could be done by transferring the model over to the geometric alteration software GeoMagic Design X (3D Systems, Research Triangle Park, NC).

Each individual component of the elbow model was imported separately into the software as polygonal surfaces. Several tools were used to perform the geometric operations. These included tools to remove any peaks that extended a certain distance from the solid surface. Any holes in the surfaces were filled and aligned with the topography of the surrounding surface.

Material could be added or removed to either extend or retract the boundaries of the bodies to match features of experienced observation. For example, it is known that the insertion of the ligament at the proximal ulna is along the sublime tubercle and the insertion at the distal humerus is along the medial epicondyle. The length that the ligament extended onto these features could be adjusted manually along a prescribed direction based on prior observation. With the conclusion of these operations, the smoothed polygon surface of the elbow model was completed (Figure 51).

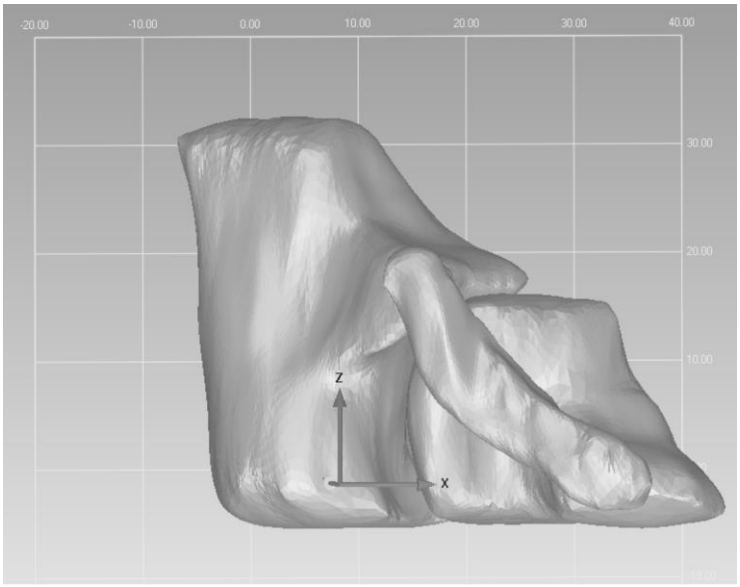

Figure 51: Smoothed Polygon 3D Elbow Model

After the smoothing was completed, the polygon surface was converted into a mesh of triangular elements. These elements were then 'stitched' together to form one coherent surface, in a process called 'exact surfacing'. The result of this operation was a fully coherent solid body, termed a 'nurbs surface' (non-uniform rational b-spline) (Figure 52).

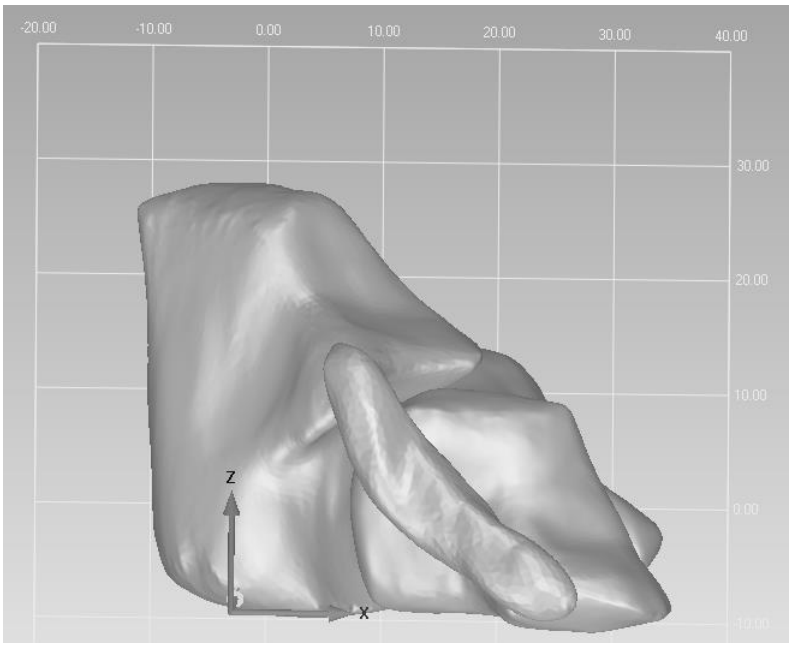

Figure 52: Nurbs Surface of 3D Elbow Model

The creation of the nurbs surface marked the completion of the generation of the elbow solid model. The solid model was then suitable to be imported into the finite element environment for mechanical analysis.

4.13 Finite Element Computation

The initial procedure for the FE analysis was to define the material via a custom subroutine using the UMAT subroutine skeleton within ABAQUS. The subroutine was to be written in FORTRAN. Due to difficulties in obtaining the requisite software packages, the model was instead implemented using the built-in anisotropic material model within FeBio. For completeness, the method for coding the custom subroutine is included. The definition of the

material model was followed by the meshing of the elbow joint model within FeBio and the subsequent application of the boundary conditions and loading cycles needed to replicate repetitive overhand throwing motions.

4.13.1 Material Definition

In defining the material model, the matrices necessary in the theoretical definition of Equation (4-35) need to be converted into a suitable form for finite element utilization.

$$\boldsymbol{\sigma_b} = C_1\mathbf{B} + C_2[2I_1\mathbf{B} + 2\mathbf{BB}] + C_3C_4e^{C_4(I_4-1)^2}(I_4 - 1)\mathbf{Fa} \otimes \mathbf{aF^T} - p\mathbf{I} \quad \text{[4-35]}$$

These matrices included the Left Stretch Tensor **B**, the square of the Right Stretch Tensor **BB,** the product of the deformation gradient and its transpose with the dyadic product of the mean fiber directions $\mathbf{Fa} \otimes \mathbf{aF^T}$ and the stiffness tensor $\mathbb{C}$.

The deformation gradient **F**, was provided in the UMAT subroutine through a built in variable. In defining the Left Stretch Tensor, the general calculation for **B** (Equation 78) was performed and converted to the appropriate nomenclature using Equations (4-36 – 4-38).

$$\mathbf{F} = F_{ij}\mathbf{e_i} \otimes \mathbf{e_j} \quad \text{[4-36]}$$

$$\mathbf{F^T} = F_{qr}\mathbf{e_q} \otimes \mathbf{e_r} \quad \text{[4-37]}$$

$$\mathbf{B} = \mathbf{FF^T} = F_{ij}F_{jr}\mathbf{e_i} \otimes \mathbf{e_r} = B_{ab}\mathbf{e_a} \otimes \mathbf{e_b} \quad \text{[4-38]}$$

This produced a 3x3 symmetric matrix. Because the matrix was symmetric, the independent components (Equation 4-39) could be extracted in the formation of a one-dimensional vector **B*** (Equation 4-40).

$$\mathbf{B} = \begin{bmatrix} B11 & B12 & B13 \\ B21 & B22 & B23 \\ B31 & B32 & B33 \end{bmatrix} \quad \text{[4-39]}$$

$$\mathbf{B}^* = [B_{11}\ B_{22}\ B_{33}\ B_{12}\ B_{13}\ B_{23}] \quad \text{[4-40]}$$

The square of the Left Stretch Tensor was given by Equation (4-41) and was similarly converted into a one-dimensional vector $\mathbf{BB}^*$ (Equation 4-42).

$$\mathbf{BB} = B_{ij}B_{jr}\mathbf{e_i} \otimes \mathbf{e_r} \quad \text{[4-41]}$$

$$\mathbf{BB}^* = [BB_{11}\ BB_{22}\ BB_{33}\ BB_{12}\ BB_{13}\ BB_{23}] \quad \text{[4-42]}$$

For the general case where the mean fiber direction consists of three components in the Cartesian space $\mathbf{a} = a_i\mathbf{e_i}$, the second order tensor $\mathbf{Fa} \otimes \mathbf{aF^T}$ was calculated as provided by Equation (4-43).

$$\mathbf{Fa} \otimes \mathbf{aF^T} = F_{ij}a_j e_i \otimes a_k F_{pk} e_p \quad \text{[4-43]}$$

For the simplified case where the mean fiber direction consists of only one component in the direction of loading, Equation (4-43) reduces to Equation (4-44).

$$\mathbf{Fa} \otimes \mathbf{aF^T} = \left(F_{ij}e_i \otimes F_{pk}e_p\right)a_1^2 \text{.....[4-44]}$$

In matrix form, $\mathbf{Fa} \otimes \mathbf{aF^T}$ was given by Equation (4-45). The symmetric components, shown in red, were transformed into the one-dimensional vector $\mathbf{Fa} \otimes \mathbf{aF^{T^*}}$ (Equation 4-46).

$$\mathbf{Fa} \otimes \mathbf{aF^T} = \begin{bmatrix} F_{11}^2 & F_{11}F_{21} & F_{11}F_{31} \\ F_{11}F_{21} & F_{21}^2 & F_{21}F_{31} \\ F_{11}F_{31} & F_{21}F_{31} & F_{31}^2 \end{bmatrix} a_1^2 \text{.....[4-45]}$$

$$\mathbf{Fa} \otimes \mathbf{aF^{T^*}} = [F_{11}^2 \;\; F_{21}^2 \;\; F_{31}^2 \;\; F_{11}F_{21} \;\; F_{11}F_{31} \;\; F_{21}F_{31}]a_1^2 \text{.....[4-46]}$$

4.13.2 Stiffness Tensor

The stiffness tensor **c**, or compliance matrix, defines the relationship between the stress tensor **σ**, and the strain tensor **ε** (Equation 4-47). The calculation of $\mathbb{C}$ was given by Equation (4-48), where **C** is the Right Cauchy-Green Stretch Tensor and W is the strain energy density (Equation 4-49).

$$\boldsymbol{\sigma} = \mathbb{C}\boldsymbol{\varepsilon} \text{.....[4-47]}$$

$$\mathbb{C} = 2\frac{\partial^2 W}{\partial \mathbf{C}^2} \text{.....[4-48]}$$

$$W = W(I_1, I_2, I_4) = C_1(I_1 - 3) + C_2(I_2 - 3) + C_3 e^{C_4(I_4-1)^2} \text{.....[4-49]}$$

Using the chain rule and product rule for differentiation, the derivation of **c** follows from the work of Weiss et al[76].

$$\mathbb{C} = 2\frac{\partial}{\partial \mathbf{C}}\left[\frac{\partial W}{\partial I_1}\frac{\partial I_1}{\partial \mathbf{C}} + \frac{\partial W}{\partial I_2}\frac{\partial I_2}{\partial \mathbf{C}} + \frac{\partial W}{\partial I_4}\frac{\partial I_4}{\partial \mathbf{C}}\right] \text{.....[4-50]}$$

$$\mathbb{C} = 2\frac{\partial}{\partial \mathbf{C}}\left[\frac{\partial W}{\partial I_1}\mathbf{I} + \frac{\partial W}{\partial I_2}(I_1\mathbf{I} - \mathbf{C}) + \frac{\partial W}{\partial I_4}\mathbf{a} \otimes \mathbf{a}\right] \text{.....[4-51]}$$

$$\mathbb{C} = 4\left[\mathbf{I} \otimes \frac{\partial}{\partial \mathbf{C}}\frac{\partial W}{\partial I_1} + \mathbf{I} \otimes \frac{\partial W}{\partial I_2}\frac{\partial I_1}{\partial \mathbf{C}} + \mathbf{I} \otimes I_1\frac{\partial}{\partial \mathbf{C}}\frac{\partial W}{\partial I_2} - \mathbf{C} \otimes \frac{\partial}{\partial \mathbf{C}}\frac{\partial W}{\partial I_2} - \frac{\partial W}{\partial I_2}\frac{\partial \mathbf{C}}{\partial \mathbf{C}} + \mathbf{a} \otimes \mathbf{a} \otimes \frac{\partial}{\partial \mathbf{C}}\frac{\partial W}{\partial I_4}\right]$$

.....[4-52]

$$\frac{\partial}{\partial \mathbf{C}}\frac{\partial W}{\partial I_k} = \frac{\partial^2 W}{\partial I_k^2}\frac{\partial I_k}{\partial \mathbf{C}}$$

$k = 1,2,4$

$$\frac{\partial}{\partial \mathbf{C}}\frac{\partial W}{\partial I_1} = \frac{\partial^2 W}{\partial I_1^2}\frac{\partial I_1}{\partial \mathbf{C}} = \frac{\partial^2 W}{\partial I_1^2}\mathbf{I}$$

$$\frac{\partial}{\partial \mathbf{C}}\frac{\partial W}{\partial I_2} = \frac{\partial^2 W}{\partial I_2^2}\frac{\partial I_2}{\partial \mathbf{C}} = \frac{\partial^2 W}{\partial I_2^2}(I_1\mathbf{I} - \mathbf{C})$$

$$\frac{\partial}{\partial \mathbf{C}}\frac{\partial W}{\partial I_4} = \frac{\partial^2 W}{\partial I_4^2}\frac{\partial I_4}{\partial \mathbf{C}} = \frac{\partial^2 W}{\partial I_4^2}\mathbf{a} \otimes \mathbf{a}$$

.....[4-53]

$$\mathbb{C} = 4\left[\frac{\partial^2 W}{\partial I_1^2}\mathbf{I}\otimes\mathbf{I} + \frac{\partial W}{\partial I_2}\mathbf{I}\otimes\mathbf{I} + I_1^2\frac{\partial^2 W}{\partial I_2^2}\mathbf{I}\otimes\mathbf{I} - \mathbf{I}\otimes\mathbf{C}\frac{\partial^2 W}{\partial I_2^2}I_1 - \mathbf{C}\otimes\mathbf{I}I_1\frac{\partial^2 W}{\partial I_2^2} + \mathbf{C}\otimes\right.$$

$$\left.\mathbf{C}\frac{\partial^2 W}{\partial I_2^2} + \mathbf{a}\otimes\mathbf{a}\otimes\mathbf{a}\otimes\mathbf{a}\frac{\partial^2 W}{\partial I_4^2}\right] \quad \ldots[4\text{-}54]$$

In Equation (4-54), $\mathbf{I}\otimes\mathbf{I}$ is the fourth-order identify tensor (3x3x3x3) and has components given by Equation (4-55).

$$\mathbf{I}\otimes\mathbf{I} = \delta_{ir}\delta_{jh}\mathbf{e_i}\otimes\mathbf{e_j}\otimes\mathbf{e_r}\otimes\mathbf{e_h} = \mathbf{e_i}\otimes\mathbf{e_j}\otimes\mathbf{e_i}\otimes\mathbf{e_j} \quad \ldots\ldots\ldots..[4\text{-}55]$$

Equation (4-56) gives the general form of the fourth-order compliance tensor (3x3x3x3) in the reference configuration. To obtain the form of $\mathbb{C}$ in the current configuration $\boldsymbol{\mathcal{C}}$ (Equation 4-56), the push-forward operation was applied to Equation (4-54).

$$\boldsymbol{\mathcal{C}} = 4\left[\left(\frac{\partial^2 W}{\partial I_1^2} + \frac{\partial^2 W}{\partial I_2} + I_1^2\frac{\partial^2 W}{\partial I_2^2}\right)\mathbf{B}\otimes\mathbf{B} - \mathbf{B}\otimes\mathbf{B^2}\frac{\partial^2 W}{\partial I_2^2}I_1 - \mathbf{B^2}\otimes\mathbf{B}I_1\frac{\partial^2 W}{\partial I_2^2} + \mathbf{B^2}\otimes\mathbf{B^2}\frac{\partial^2 W}{\partial I_2^2} + \right.$$

$$\left.\frac{\partial^2 W}{\partial I_4^2}I_4^2\mathbf{a}\otimes\mathbf{a}\otimes\mathbf{a}\otimes\mathbf{a}\right] \quad \ldots[4\text{-}56]$$

$\mathbf{B}\otimes\mathbf{B}$ is a fourth-order tensor with components given by Equation (4-57).

$$\mathbf{B}\otimes\mathbf{B} = B_{ij}B_{kl}\mathbf{e_i}\otimes\mathbf{e_j}\otimes\mathbf{e_k}\otimes\mathbf{e_l} \quad \ldots\ldots\ldots\ldots\ldots\ldots\ldots[4\text{-}57]$$

$\mathbf{a}\otimes\mathbf{a}\otimes\mathbf{a}\otimes\mathbf{a}$ is a fourth-order tensor with components given by Equation (4-58).

$$\mathbf{a}\otimes\mathbf{a}\otimes\mathbf{a}\otimes\mathbf{a} = a_i a_j a_k a_l\mathbf{e_i}\otimes\mathbf{e_j}\otimes\mathbf{e_k}\otimes\mathbf{e_l} \quad \ldots\ldots\ldots\ldots\ldots\ldots..[4\text{-}58]$$

Equation (4-56) gives the general form for the stiffness tensor for a hyper elastic material with an arbitrary strain energy function. Given the form of the chosen strain energy (Equation 4-59), the form of $\boldsymbol{\mathcal{C}}$ is simplified (Equation 4-64) using the results of Equations (4-59 – 4-63).

$$\frac{\partial W}{\partial I_1} = C_1 \quad \text{[4-59]}$$

$$\frac{\partial W}{\partial I_2} = C_2 \quad \text{[4-60]}$$

$$\frac{\partial^2 W}{\partial I_1^2} = 0 \quad \text{[4-61]}$$

$$\frac{\partial^2 W}{\partial I_2^2} = 0 \quad \text{[4-62]}$$

$$\frac{\partial^2 W}{\partial I_4^2} = \mathbf{2} C_3 C_4 e^{\left(C_4 (I_4 - 1)\right)^2} [2C_4 (I_4 - 1)^2 + 1] \quad \text{[4-63]}$$

$$\boldsymbol{\mathcal{C}} = 4\left[C_2\, \mathbf{B} \otimes \mathbf{B} + \frac{\partial^2 W}{\partial I_4^2} I_4^2 \mathbf{a} \otimes \mathbf{a} \otimes \mathbf{a} \otimes \mathbf{a}\right] \quad \text{[4-64]}$$

4.13.3 Reduction of Stiffness Tensor

The indicial notation $\boldsymbol{\mathcal{C}}$ is given by Equation (4-65). The components of the Cauchy stress tensor $\sigma_{ij}(3x3)$, are then related to the components of the strain tensor $\varepsilon_{kl}(3x3)$, through Equation (4-66).

$$\boldsymbol{\mathcal{C}} = \mathcal{C}_{ijkl}\mathbf{e_i} \otimes \mathbf{e_j} \otimes \mathbf{e_k} \otimes \mathbf{e_l} \quad \text{[4-65]}$$

$$\sigma_{ij} = \mathcal{C}_{ijkl}\varepsilon_{kl} \quad \text{[4-66]}$$

$\boldsymbol{\mathcal{C}}$ generally has 81 material constants. Through consideration of the symmetries of the stress and strain tensors $\sigma_{ij} = \sigma_{ji}$ and $\varepsilon_{kl} = \varepsilon_{lk}$, the number of independent material constants are reduced to 21 and $\boldsymbol{\mathcal{C}}(3x3x3x3)$ is reduced to $\boldsymbol{\mathcal{C}}(6x6)$ (Equation 4-67).

$$\begin{bmatrix}\sigma_{11}\\ \sigma_{22}\\ \sigma_{33}\\ \sigma_{23}\\ \sigma_{13}\\ \sigma_{12}\end{bmatrix} = \begin{bmatrix} \mathcal{C}_{1111} & \mathcal{C}_{1122} & \mathcal{C}_{1133} & \mathcal{C}_{1123} & \mathcal{C}_{1113} & \mathcal{C}_{1112} \\ & \mathcal{C}_{2222} & \mathcal{C}_{2233} & \mathcal{C}_{2223} & \mathcal{C}_{2213} & \mathcal{C}_{2212} \\ & & \mathcal{C}_{3333} & \mathcal{C}_{3323} & \mathcal{C}_{3313} & \mathcal{C}_{3312} \\ & & & \mathcal{C}_{2323} & \mathcal{C}_{2313} & \mathcal{C}_{2312} \\ & symm & & & \mathcal{C}_{1313} & \mathcal{C}_{1312} \\ & & & & & \mathcal{C}_{1212} \end{bmatrix} \begin{bmatrix}\varepsilon_{11}\\ \varepsilon_{22}\\ \varepsilon_{33}\\ 2\varepsilon_{23}\\ 2\varepsilon_{13}\\ 2\varepsilon_{12}\end{bmatrix} \quad \text{[4-67]}$$

4.13.4 Transversely Isotropic Stiffness Matrix

Ligaments are commonly modeled as transversely isotropic materials[45]. These materials have one plane of isotropy. The preferred direction of the material is symmetric about the normal

axis of this plane (Figure 53). This material symmetry reduces the compliance matrix to the form given in Equation (4-68), with five independent components.

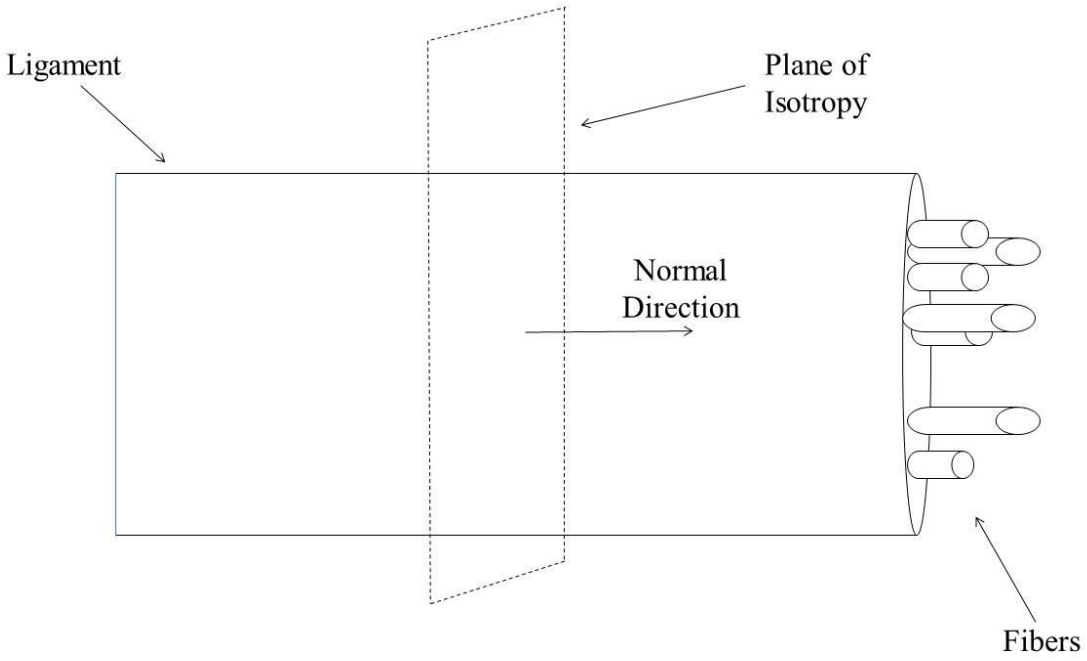

Figure 53: Transverse Isotropy of Ligament Sturcture

$$\begin{bmatrix}\sigma_{11}\\ \sigma_{22}\\ \sigma_{33}\\ \sigma_{23}\\ \sigma_{13}\\ \sigma_{12}\end{bmatrix} = \begin{bmatrix} \mathcal{C}_{1111} & \mathcal{C}_{1122} & \mathcal{C}_{1133} & 0 & 0 & 0 \\ & \mathcal{C}_{1111} & \mathcal{C}_{1133} & 0 & 0 & 0 \\ & & \mathcal{C}_{3333} & 0 & 0 & 0 \\ & & & \mathcal{C}_{2323} & 0 & 0 \\ & symm & & & \mathcal{C}_{2323} & 0 \\ & & & & & \frac{1}{2}(\mathcal{C}_{1111}-\mathcal{C}_{1122}) \end{bmatrix} \begin{bmatrix}\varepsilon_{11}\\ \varepsilon_{22}\\ \varepsilon_{33}\\ 2\varepsilon_{23}\\ 2\varepsilon_{13}\\ 2\varepsilon_{12}\end{bmatrix} \quad \text{....[4-68]}$$

From the results of Equation (4-68), the individual components for the transversely isotropic hyper elastic incompressible material are given by Equations (4-69 – 4-73).

$$\mathcal{C}_{1111} = 4C_2B_{11}B_{11} + \mathbf{2}C_3C_4e^{\left(C_4(I_4-1)\right)^2}[2C_4(I_4-1)^2+1]I_4^2(a_1a_1a_1a_1).....[4\text{-}69]$$

$$\mathcal{C}_{1122} = 4C_2B_{11}B_{22} + \mathbf{2}C_3C_4e^{\left(C_4(I_4-1)\right)^2}[2C_4(I_4-1)^2+1]I_4^2(a_1a_1a_2a_2).....[4\text{-}70]$$

$$\mathcal{C}_{1133} = 4C_2B_{11}B_{33} + \mathbf{2}C_3C_4e^{\left(C_4(I_4-1)\right)^2}[2C_4(I_4-1)^2+1]I_4^2(a_1a_1a_3a_3)....[4\text{-}71]$$

$$\mathcal{C}_{2323} = 4C_2B_{23}B_{23}.....[4\text{-}72]$$

$$\mathcal{C}_{3333} = 4C_2B_{33}B_{33} + \mathbf{2}C_3C_4e^{\left(C_4(I_4-1)\right)^2}[2C_4(I_4-1)^2+1]I_4^2(a_3a_3a_3a_3).....[4\text{-}73]$$

If it is assumed that the mean fiber direction vector **a**, has only one component in the preferred direction of loading, then $a_2 = a_3 = 0$ and Equations (4-69 – 4-73) reduce to Equations (4-74 – 4-78).

$$\mathcal{C}_{1111} = 4C_2B_{11}B_{11} + \mathbf{2}C_3C_4e^{\left(C_4(I_4-1)\right)^2}[2C_4(I_4-1)^2+1]I_4^2(a_1a_1a_1a_1).....[4\text{-}74]$$

$$\mathcal{C}_{1122} = 4C_2B_{11}B_{22}.....[4\text{-}75]$$

$$\mathcal{C}_{1133} = 4C_2B_{11}B_{33}.....[4\text{-}76]$$

$$\mathcal{C}_{2323} = 4C_2B_{23}B_{23}.....[4\text{-}77]$$

$$\mathcal{C}_{3333} = 4\mathrm{C}_2\mathrm{B}_{33}\mathrm{B}_{33} \quad [4\text{-}78]$$

With the relevant matrices and vectors defined, the damage augmentation was to be added. This was to be done by defining a scalar function given by Equation (4-5). In FORTRAN, this function can be defined explicitly.

This completes the description of the intended FORTRAN coding. The FE simulations to follow were performed using built-in routines in the open-source software FeBio.

4.14 Finite Element Details within FeBio

FeBio is an open-source finite element package specifically designed for the solution of nonlinear problems involving bio-materials. It was desired to use this package to perform the work because of the readily available constitutive models for fibrous tissues.

4.14.1 Mesh and Elements

The three solid bodies (distal humerus, proximal ulna and AMCL) were imported separately into the FeBio environment. Each body was identified as a solid continuum. The meshing of each body was done individually using the automatic meshing tool with tetrahedral elements of size 1. The tet4 element is a 4 node linear tetrahedral element. The ulna, humerus and AMCL were each meshed with this element (Figure 54).

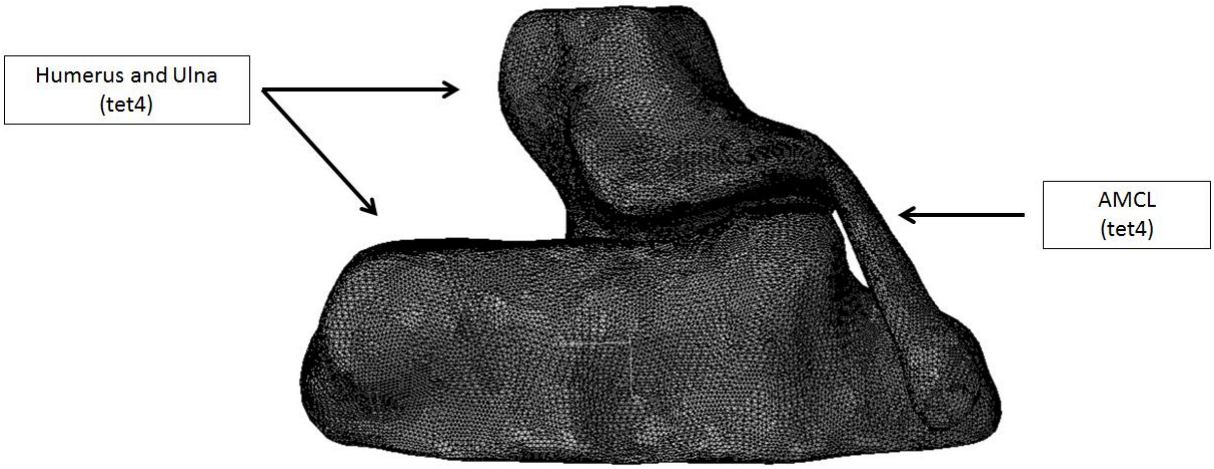

Figure 54: Meshed Bodies of 3D Elbow Model

4.14.2 Step Details and Incrimination

The type of analysis step chosen was 'Static General'. This step is used for analyses where effects from inertia can be neglected. The total simulation time was dictated by the maximum displacement and loading frequency of the experimental protocol. Experimentally, specimens were loaded at a frequency equal to half the measured quantity per second. So, a simulation to a displacement of x, would have a total simulation time of 2x. As a general rule of thumb, the initial step increment was set to one-tenth of the total simulation time, 0.2x. Other essential settings such as cutback behavior, Newton/Quasi-Newton solution methods and maximum number of iterations per step were adjusted as needed.

4.14.3 Material Properties

The ulna and humerus were modeled as Neo-Hookean materials. To define this material two parameters were needed. These were the elastic modulus and Poisson's ratio. The elastic modulus used was that of cortical bone (approximately 1.7 Gpa). Poisson's ratio was taken as 0.45. The utilized material models are shown in Figure (55).

The AMCL was modeled as hyperelastic using the transversely isotropic Mooney-Rivlin material model. To define this model the four constants C_1-C_4, needed to be given, as well as the density and bulk modulus. The density was given as 1000 kg/m^3, which is typical for ligaments where water makes up the majority of the mass. The bulk modulus, which defines the tendency for volume change of the material when subjected to uniform pressure was given as 1e9 N/m^2. A high bulk modulus is typical for materials which are nearly incompressible.

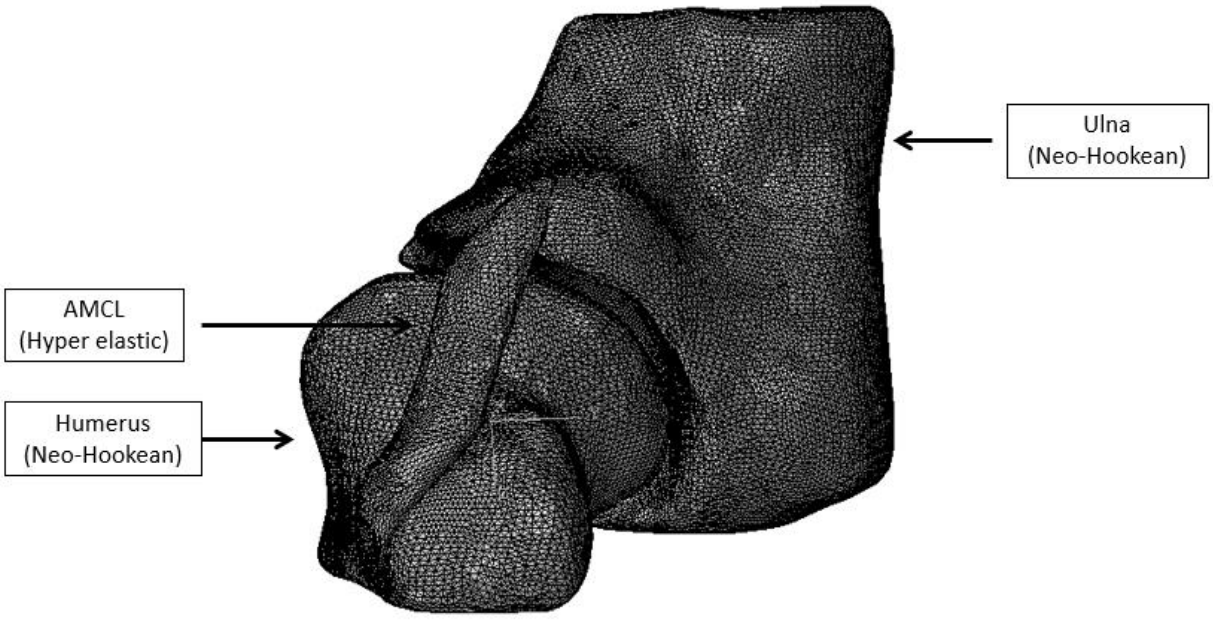

Figure 55: Material Definitions for the 3D Elbow Model

4.14.4 Fiber Direction

With a transversely isotropic material, it is necessary to prescribe a fiber direction. There were several options within FeBio to define the fiber direction. The method which uses two local node numbers was chosen. The local fiber axis was defined by the local element nodes, as a vector originating at the initial node and terminating at the latter node. This chosen alignment is in accordance with the shape of the ligament. Figure (56) shows an example of a local fiber axis for a 4 node tetrahedral element (tet4) defined from local node numbers 2 to 4. These local fibers, chosen such that they align with the long axis of the ligament, are shown in Figure (57).

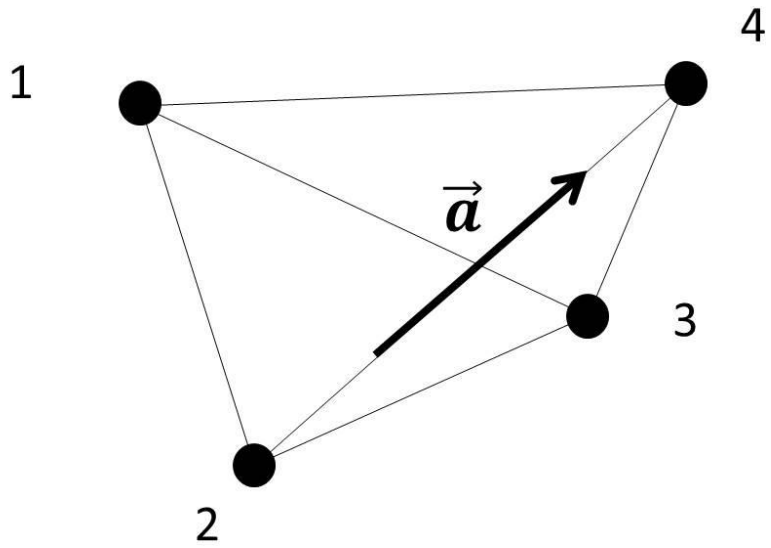

Figure 56: Example of Local Fiber Axis for 4 Node Tetrahedral Element

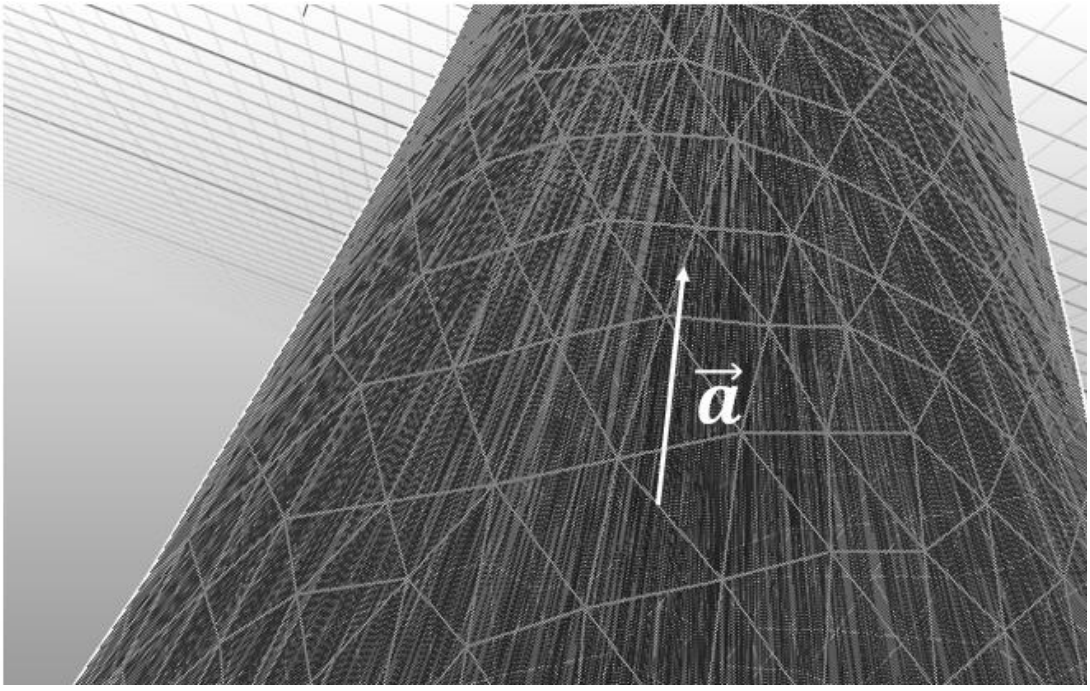

Figure 57: Fiber Alignment Along AMCL Long Axis

4.14.5 Constraints

The constraints in the model were defined at the contact points between the AMCL and its insertion points at the distal humerus and proximal ulna (Figure 58). A tied-elastic constraint was used to model the contact. This type of constraint allows no relative motion between two surfaces within a specified location tolerance, with all surfaces located within the tolerance being 'tied' together. This meant that the motion of the nodes, for each degree of freedom (DOF), would be equivalent for the AMCL and boney materials.

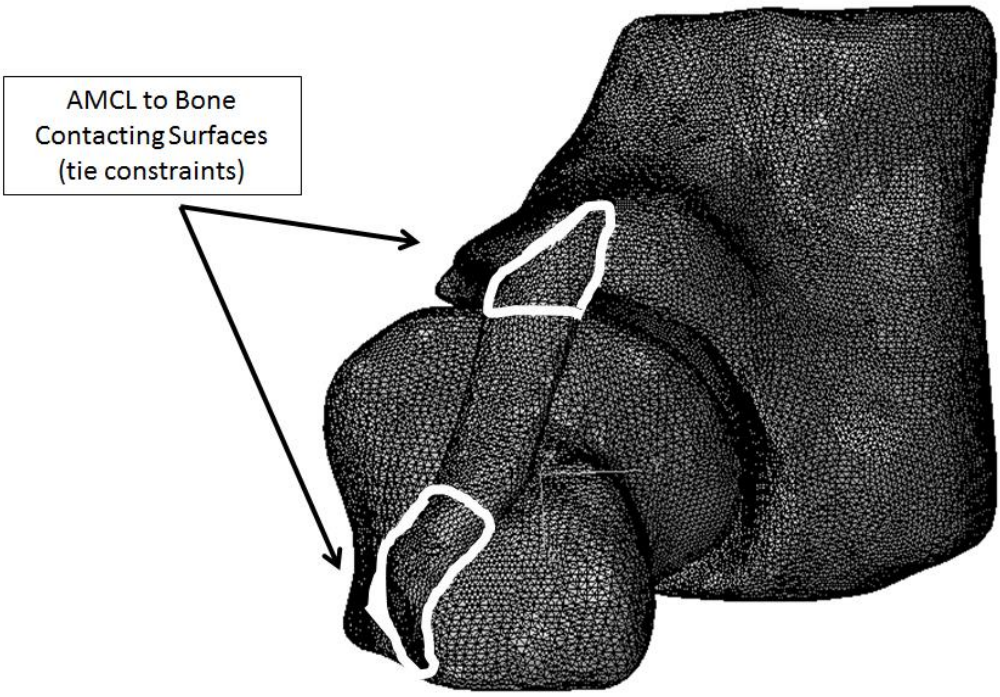

Figure 58: Tied-Elastic Constraints at Ulna and Humerus Insertions

4.14.6 Boundary Conditions

The boundary conditions in the model were applied to the two bones. These conditions were fixed and prescribed displacements. The proximal humerus was set to be fixed in all six DOF $(u_x = u_y = u_z = 0 \ \& \ \theta_x = \theta_y = \theta_z = 0)$.

The prescribed displacement of the ulna was set to mimic the kinematics of valgus rotation. Applying a pure rotation in a finite element setting is challenging. To circumvent this, the displacement was instead applied as a pure vertical distraction, with observations made regarding the joint spacing and small angle theory.

For an arbitrary vertical and rotational displacement δ_v and δ_r, the opening of the joint can be monitored by observing the separation of two points a and b (Figure 59) on the distal humerus and proximal ulna, respectively. For the same initial position, the vertical and rotational displacements will produce displacement vectors r and r', respectively.

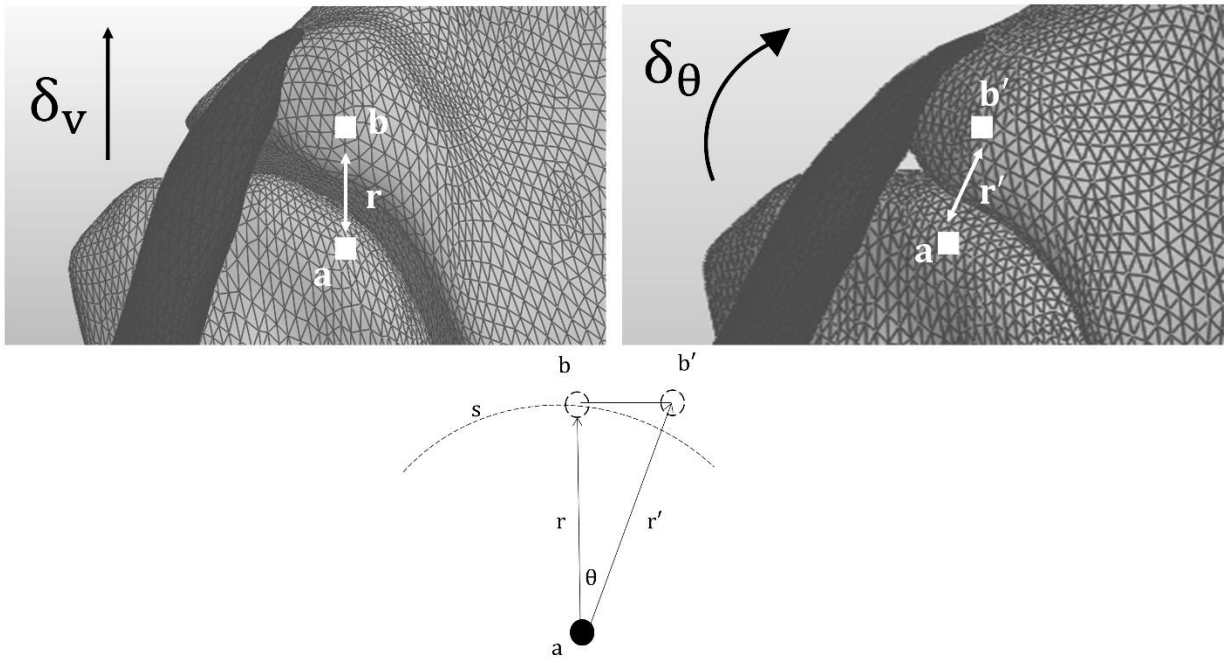

Figure 59: Displacement Vectors for Arbitrary Points during Vertical and Rotational Ulnar Motion

According to small angle theory, for sufficiently small angles θ, the $\sin\theta \approx \theta$. So, for small angle rotations about the arc s, the length bb' is approximately equal to rθ. From the Pythagorean theorem (Equations 4-79 – 4-82), it can be seen that for sufficiently small angles $r \approx r'$ and the displacement caused by the pure vertical displacement is comparable to that caused by a pure valgus rotation.

$$r' = \sqrt{r^2 + (bb')^2} \quad \text{[4-79]}$$

$$= \sqrt{r^2 + (r\theta)^2} \quad \text{[4-80]}$$

$$= \sqrt{r^2(1 + \theta^2)} \quad \text{[4-81]}$$

$$r' \approx r \quad \text{[4-82]}$$

4.14.7 Iterative Fatigue Damage Loading Protocol

Because the damage variable is a scalar quantity independent of the finite element routine, its effect on the simulated mechanical response could be imposed in an iterative fashion through the successive operation of multiple simulations. The damage variable D, multiplies the elastic constitutive model $\boldsymbol{\sigma}$, to create the modified constitutive model $\boldsymbol{\sigma}'$**,** given by Equation (4-83).

$$\boldsymbol{\sigma}' = (1 - D)\left[C_1\mathbf{B} + C_2[2I_1\mathbf{B} + 2\mathbf{BB}] + C_3C_4e^{C_4(I_4-1)^2}(I_4 - 1)\mathbf{Fa} \otimes \mathbf{aF^T} - p\mathbf{I}\right] \quad \text{[4-83]}$$

The multiplication of the scalar parameter (1-D), creates the modified constitutive parameters C_1', C_2' and C_3', given by Equations (4-84 – 4-86). C_4 was unmodified.

$$C_1' = (1 - D)C_1 \quad \text{[4-84]}$$

$$C_2' = (1 - D)C_2 \text{.....[4-85]}$$

$$C_3' = (1 - D)C_3 \text{.....[4-86]}$$

The damage variable D, evolves during every cycle of a cyclic loading event. Therefore, the value of D is a constant during any particular cycle. The modified parameters can then be updated during every cycle i, of the loading and depend only on the current value of the damage parameter and the value of the constitutive parameter from the undamaged model (Equations 4-87 – 4-89).

$$C_{1(i)}' = (1 - D_i)C_1 \text{.....[4-87]}$$

$$C_{2(i)}' = (1 - D_i)C_2 \text{.....[4-88]}$$

$$C_{3(i)}' = (1 - D_i)C_3 \text{.....[4-89]}$$

These updated parameters then 'soften' the stress response accordingly. The entire iterative fatigue damage loading protocol is outlined in the next section.

4.14.8 Iterative Fatigue Damage Loading Protocol

The transversely isotropic Mooney-Rivlin constitutive model for anisotropic elastomers was selected in FeBio. The regressed parameters C_1, C_2, C_3 and C_4 were input into the model.

The modeled specimen was to be loaded in vertical elongation, replicating valgus rotation-induced joint opening. The displacement was applied linearly, with a constant ramp up towards the maximum displacement over the course of the allotted time (Figure 60).

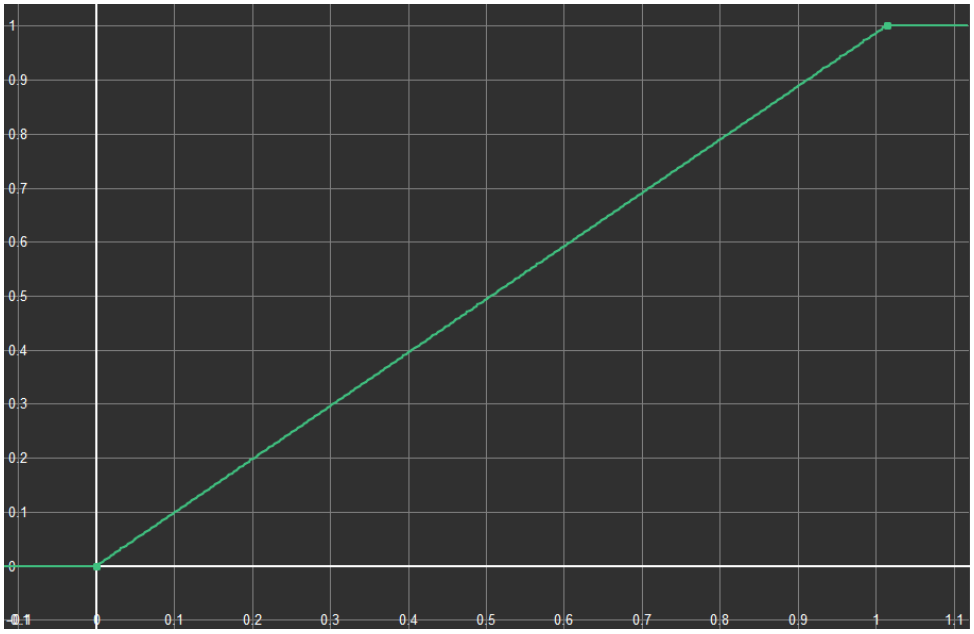

Figure 60: Triangular Finite Element Displacement Curve

Every element of the AMCL was selected for processing (Figure 61). The data for stress and strain along the fiber direction (1st principal direction) were extracted and the maximum stress and strain were identified. To move forward in the analysis, the maximum stress or strain could have either been utilized. As a representation, the maximum stress was identified on the

interpolated fatigue life curve as a fraction of the absolute failure stress and the corresponding total cycles to failure n_f, was determined (Figure 62).

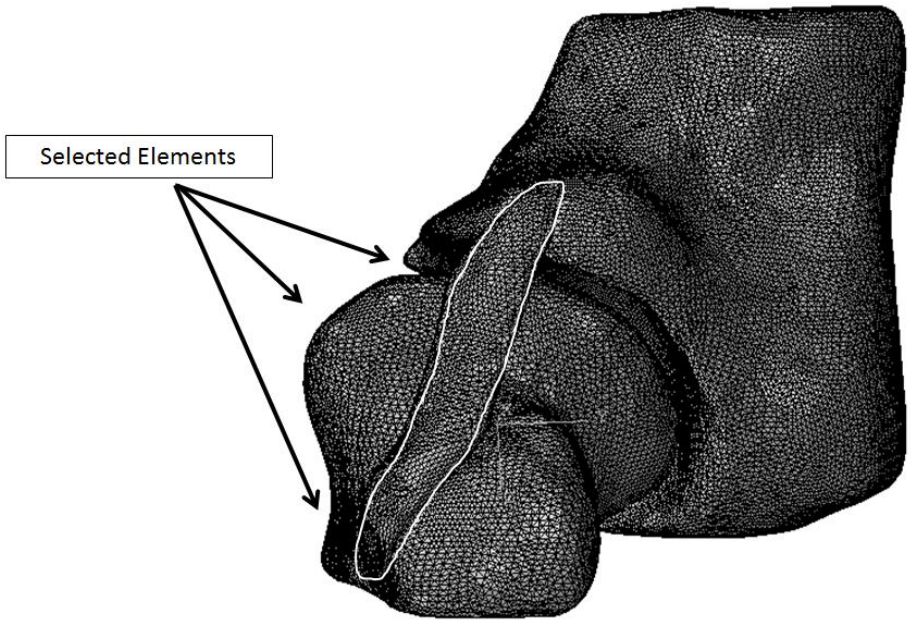

Figure 61: Selection of Every AMCL Element for Postprocessing

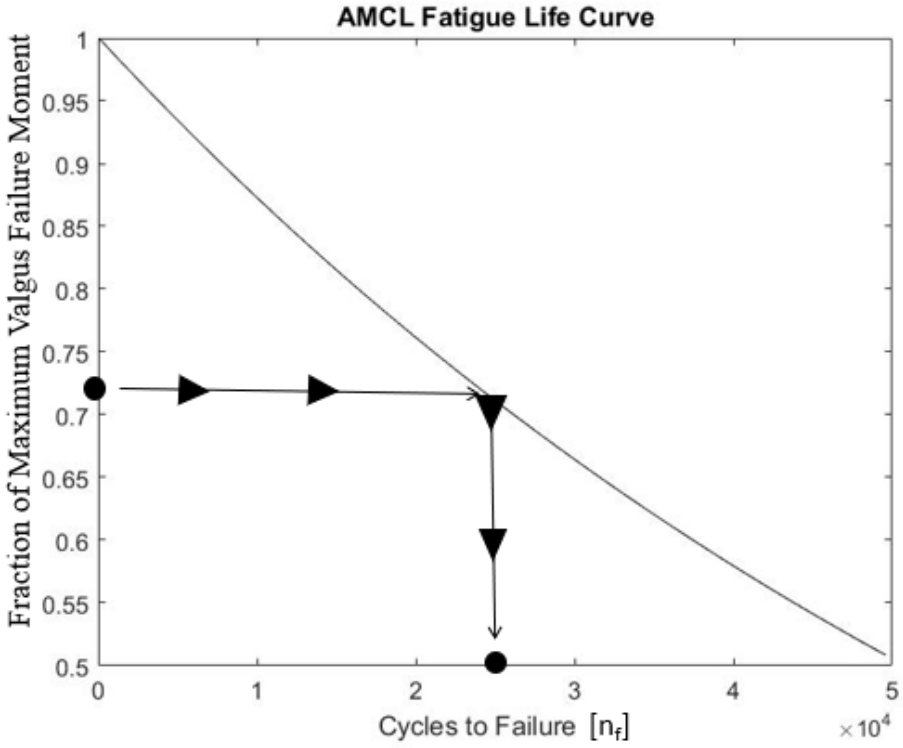

Figure 62: Identification of n_f from AMCL Fatigue Life Curve

The selected value of n_f, was then used to set the scale of the damage evolution curve for the AMCL. With the evolution curve set, the manner in which the damage variable D, would evolve over the remainder of the cycling was fixed. For a desired number of cycles n, the amount of requisite damage D, was known (Figure 63).

For example, if the results for the average stress produced a n_f of 10,000 cycles and the resulting mechanical response after 6,000 cycles was desired, then the value of D corresponding to an n/n_f value of 6000/10000 = 0.6 would be selected. This would produce a mechanical response of $\sigma' = (1 - D(0.6))\sigma$.

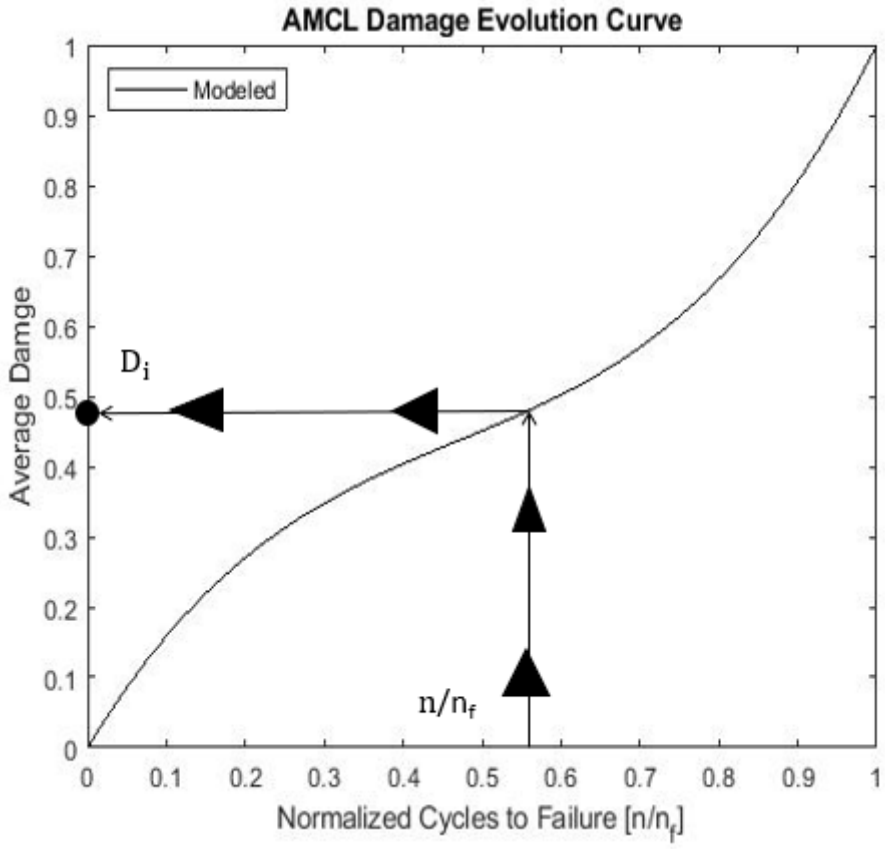

Figure 63: Identification of Damage from AMCL Damage Evolution Curve

With D known, the modified constitutive parameters C_1', C_2' and C_3' were determined. These modified values were re-entered into the FeBio model and the simulation was repeated. This was repeated for an indefinite number of desired cycles. The results for each interaction were extracted and analyzed in the post processing. An example of the expected results for an arbitrary specimen are given in Figure (64), where the mechanical response gradually progresses toward failure ($\sigma = 0$) as the cycles progress toward n_f.

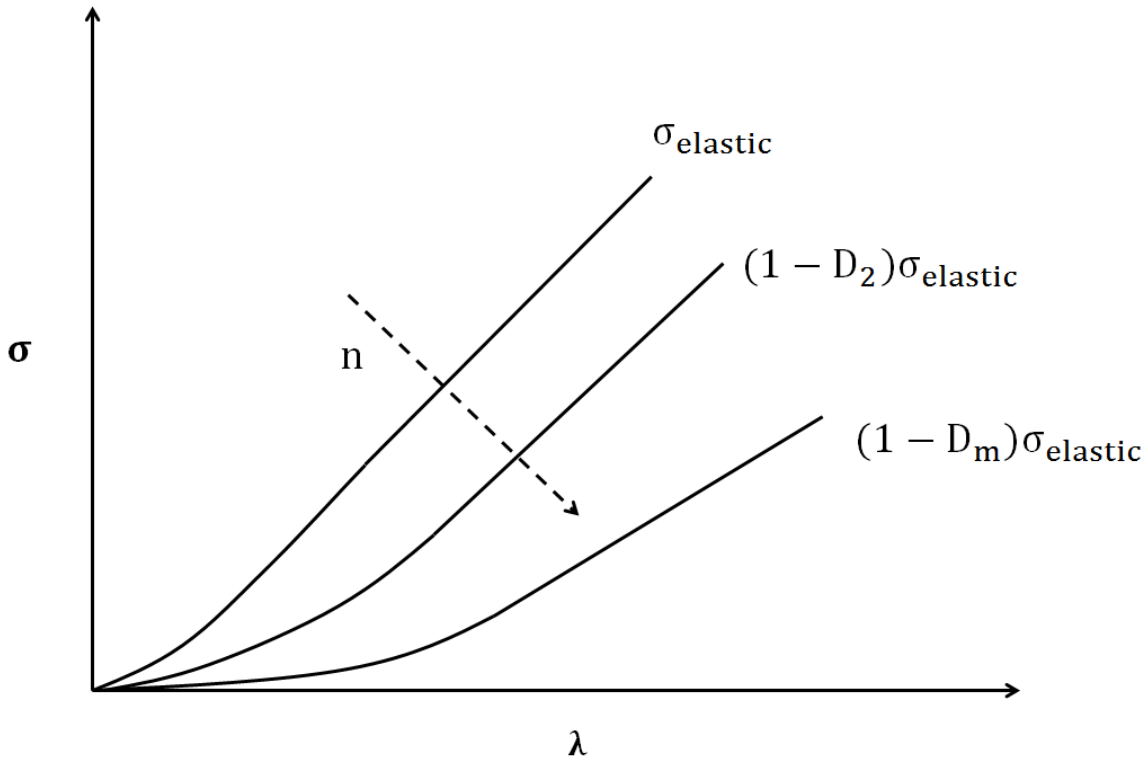

Figure 64: Representative Stress-Stretch Behavior for Anticipated Fatigue-Induced Stress Softening

4.14.9 Convergence

Convergence was evaluated in terms of mesh independence. The maximum stress was recorded for a particular group of elements after the completion of a given simulation. The mesh size was reduced by half and the simulation was repeated. This process continued until the maximum stress for subsequent simulations changed by less than 1 kPa for an arbitrary series of simulations.

4.14.10 Post-Processing and Model Validation

The variables of interest in post processing were the stress and strain in the primary (fiber) loading direction. For a given number of cycles and a given level of valgus torque, there was an estimated level of average damage. This average damage not only softened the ligament response over the cycling, but also increased the range of the valgus rotation and, therefore, the maximum stretch of the ligament. These simulated stretch results can be compared to the experimental stretch measures. Validation will be inferred for simulation stretch increase measurements that resulted to within 10% of the average empirical results, for a given number of cycles and valgus torque level.

5.0 Results

5.1 Anatomy

Every specimen tested in the elastic and fatigue testing protocols, were measured prior to testing using calipers. The average distal width and thickness were $8.52\ \text{mm} \pm 1.84$ and $1.66\ \text{mm} \pm 0.45\ \text{mm}$. The average proximal width and thickness were $5.7\ \text{mm} \pm 1.21$ and $2.09\ \text{mm} \pm 0.35\ \text{mm}$. These results are presented in Figure (65).

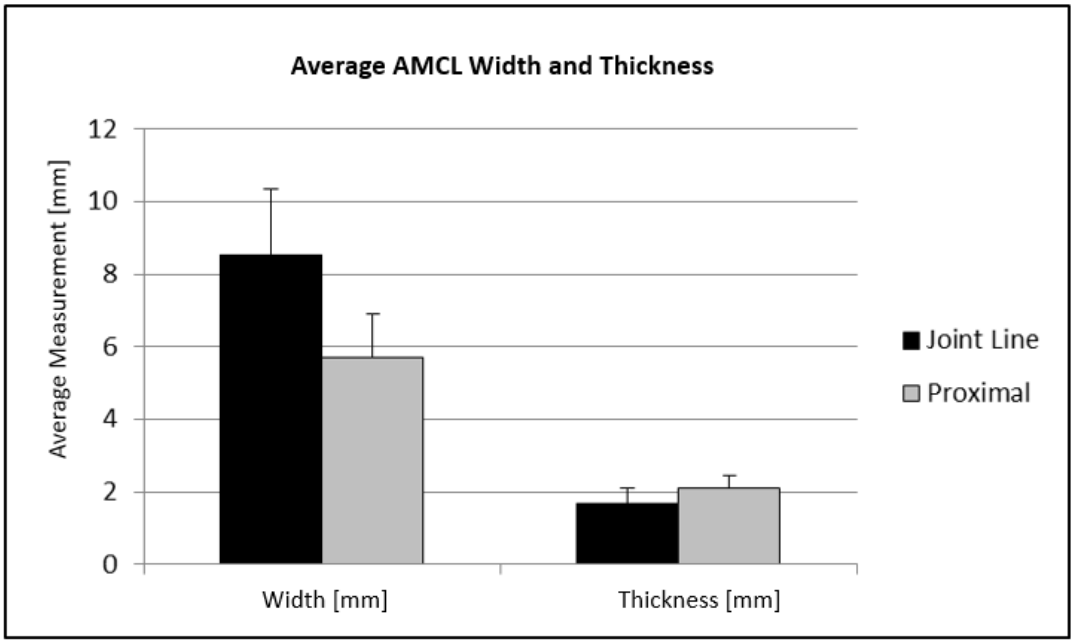

Figure 65: Average AMCL Width and Thickness Results

5.2 Elastic Tensile Testing and Failure Testing Results

A total of eleven specimens were tested in the elastic testing and failure testing protocols. The average failure load for the specimens was $595.25\ \text{N} \pm 201.93\ \text{N}$. The failure loads for each specimen and the average are presented in Figure (66). Dividing the failure load by the cross-sectional area of each specimen, resulted in an average nominal failure stress of $47.46\ \text{Mpa} \pm 25.42\ \text{Mpa}$.

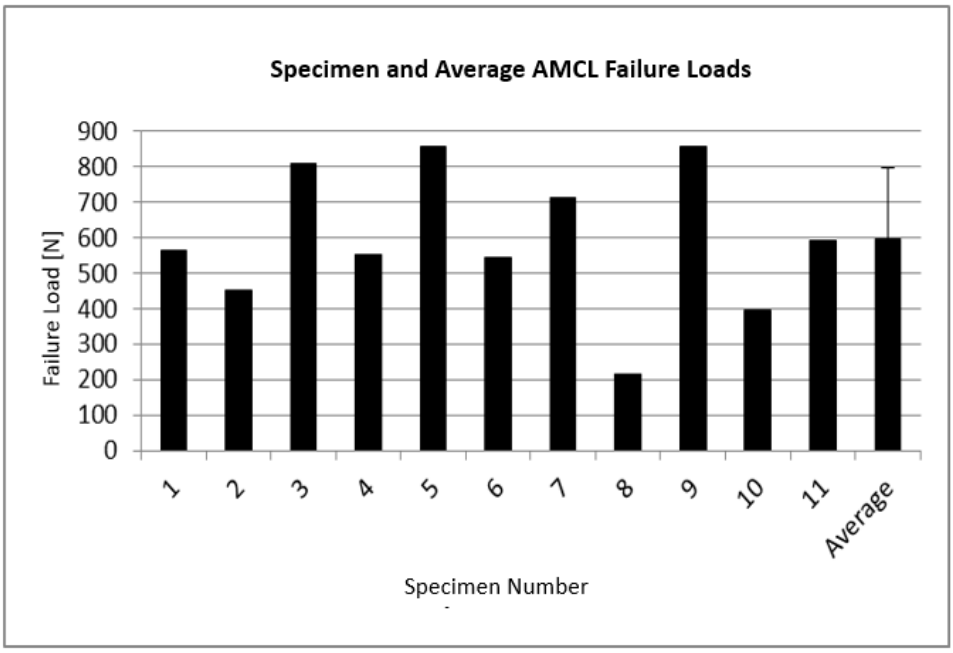

Figure 66: AMCL Failure Load Results

Applying the transversely isotropic Mooney-Rivlin four parameter constitutive model to the elastic data for the middle band of each specimen at 90˚ of flexion, produced the average results given in Table (2). The average value of C_3 was at least one order of magnitude greater than that for C_2 and C_1. C_4 was at least six orders of magnitude less than C_1-C_3.

Table 2: Average Parameters for the Transversely Isotorpic Mooney-Rivlin Constitutive Model

Constitutive Model Parameter	Average Value
C1	$7.79e6 \pm 1.14e7$
C2	$1.98e6 \pm 2.73e6$
C3	$5.10e8 \pm 1.18e9$
C4	1.26 ± 23.01
R^2	0.992 ± 0.015

5.2.1 Tensile Testing Failure Modes

Of the eleven specimens tested in vertical elongation, five failed due to humeral avulsion. In this type of failure, the fibers of the AMCL were separated from their insertion at the medial epicondyle. Figure (67) shows two examples of this failure mode.

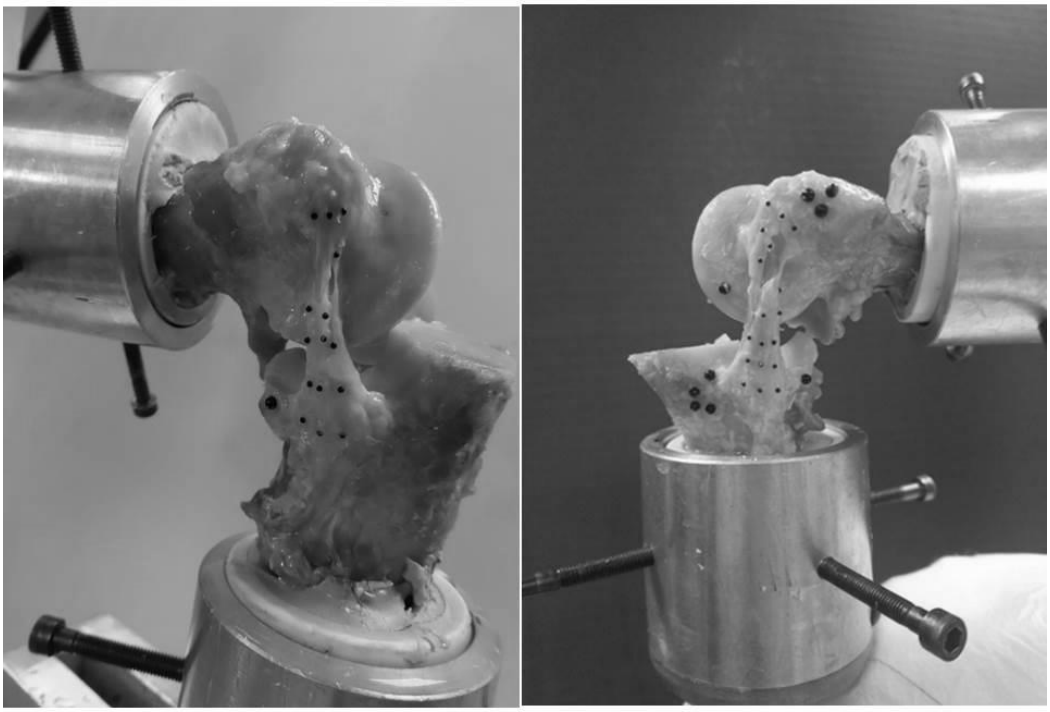

Figure 67: Humeral Avulsion Tensile Failure

Six of the tested specimens failed in ulnar avulsion. In this failure mode, the AMCL fibers were separated from the sublime tubercle. Figures (68) gives two examples of this failure mode.

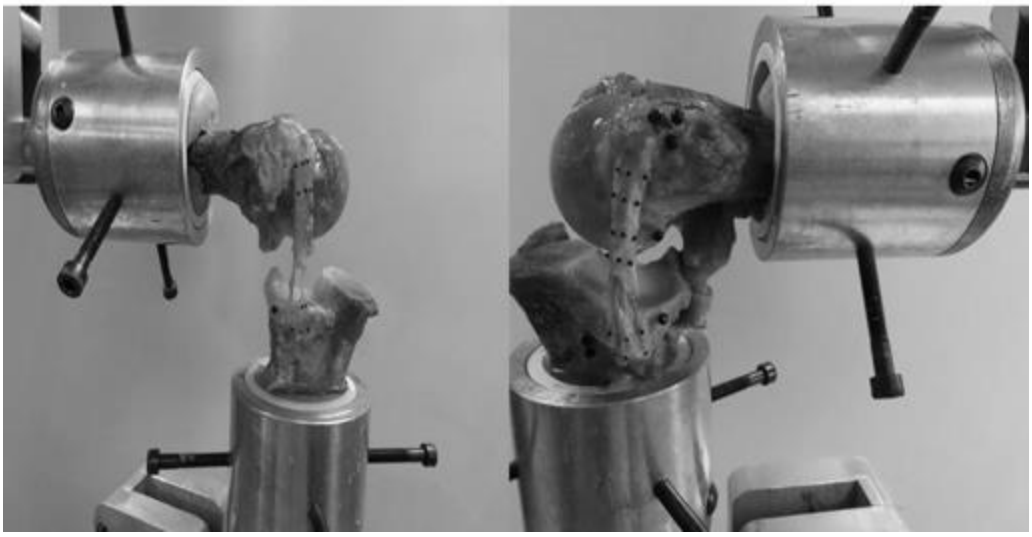

Figure 68: Ulnar Avulsion Tensile Failure

5.3 Fatigue Testing Results

The use of the failure loads from the elongation tests for the calculation of the theoretical valgus failure moments $\mathbf{M_f}$, produced an average single cycle moment of $25.3\ \text{Nm} \pm 8.77\ \text{Nm}$. For the specimens tested at 90% of their respective $\mathbf{M_f}$ magnitude, the average failure torque was $23.14\ \text{Nm} \pm 6.24\ \text{Nm}$. The average cycles to failure was 3211 ± 4721.33. For the specimens tested at 80% of their respective $\mathbf{M_f}$ magnitude, the average failure torque was $19.96\ \text{Nm} \pm 7.97\ \text{Nm}$. The average cycles to failure was 25063 ± 30487.58. A log plot of the acquired data for the eleven specimens is given in Figure (69).

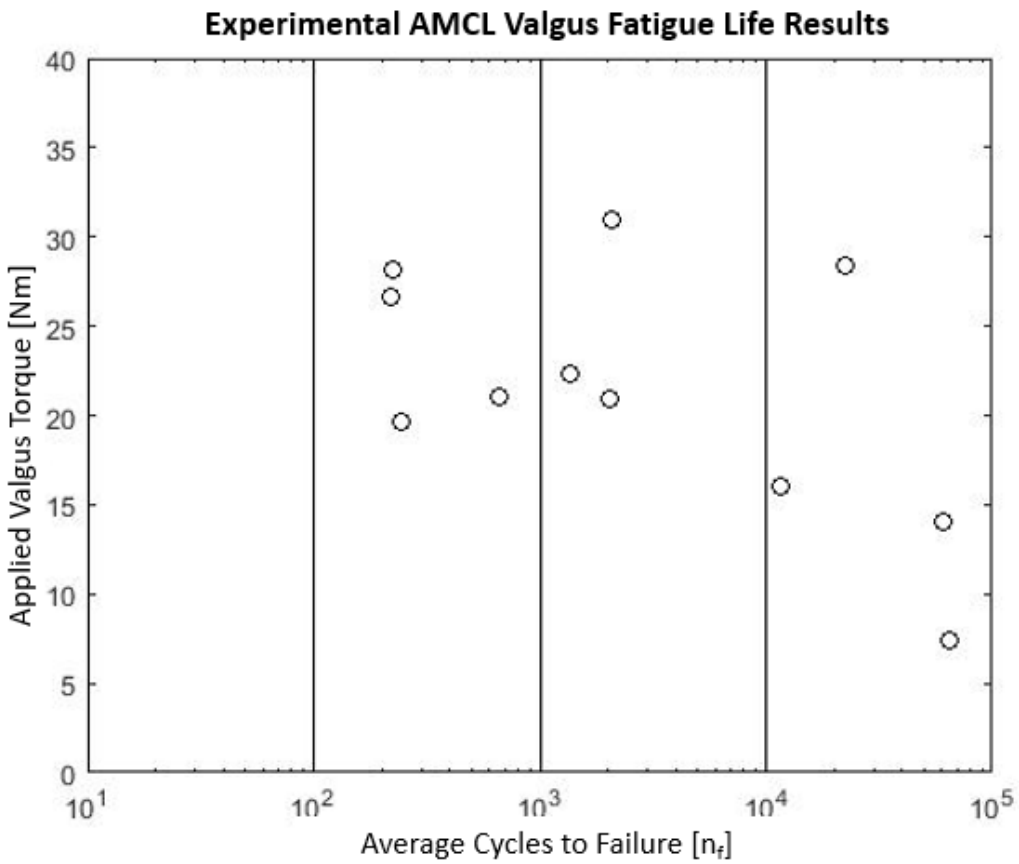

Figure 69: Specimen AMCL Valgus Fatigue Fatilure Results

In Figure (69), it can be seen that, in general, the fatigue life of the specimens tended to increase as the experimentally applied valgus moment magnitude decreased. This trend can be seen more clearly (Figure 70) utilizing the regression of a linear logarithmic model (Equation 5-1), where τ is the applied valgus moment and the undetermined constants are a and b. The results for the parameters a and b were 45.9623 and -3.115, with an R^2 value of 0.91.

$$\tau = a + b\ln(n) \quad \text{.....[5-1]}$$

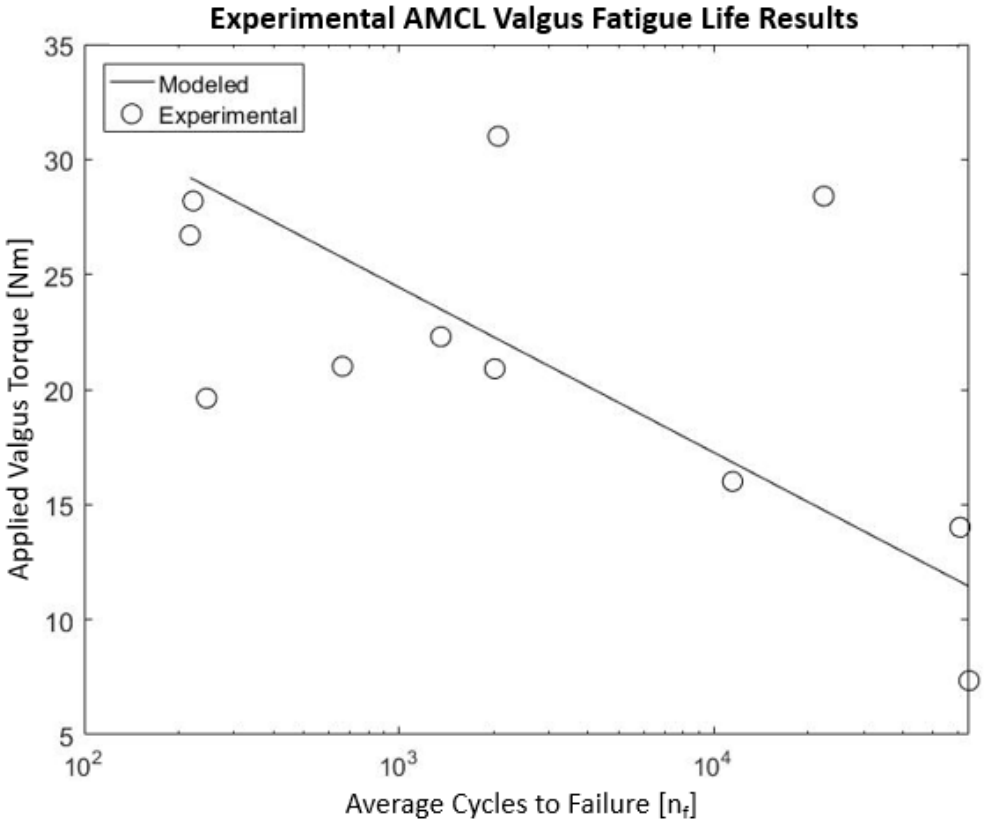

Figure 70: Linear Logarithmic Regression Showing Negative Trend

5.3.1 Stress-Based Fatigue Life Curve

The average results for this data were used to create the average AMCL fatigue life curve of Figure (71), where each data point represents the average valgus moment and failure cycles for all of the specimens tested at that particular percentage of their respective $\mathbf{M_f}$ magnitude (5 specimens at 90% and 6 specimens at 80%).

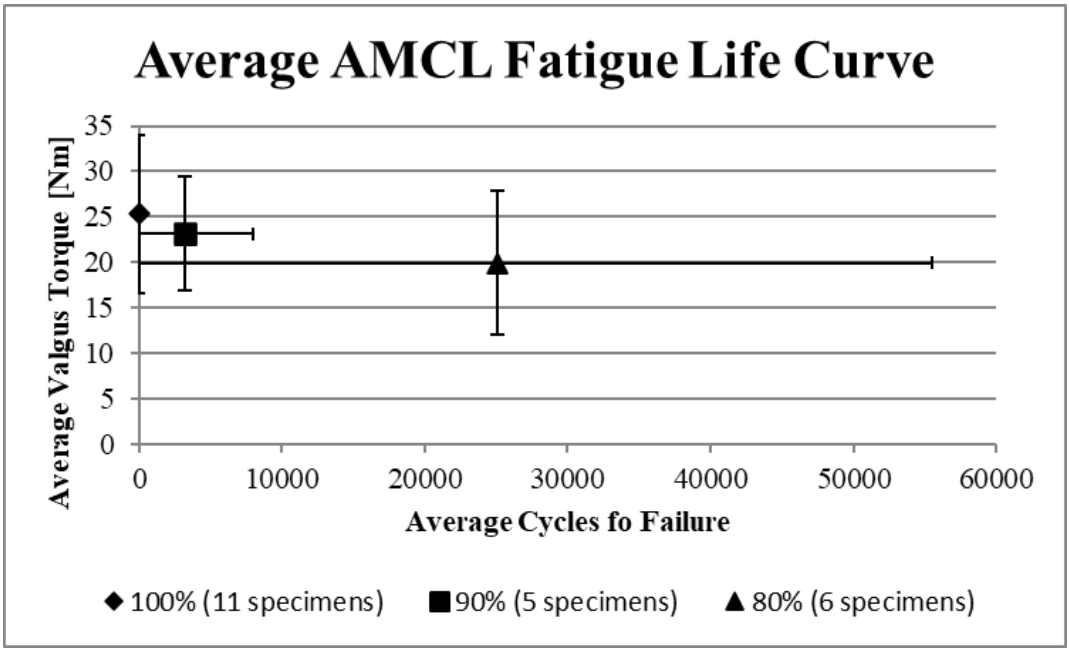

Figure 71: Average AMCL Valgus Fatigue Life Curve

Figure (72) gives an alternative non-dimensional version of the fatigue life curve where the ordinate is given as the respective fractions of $\mathbf{M_f}$. The data from Figure (72) was used to determine the parameters of the exponential decay model of Equation (4-33).

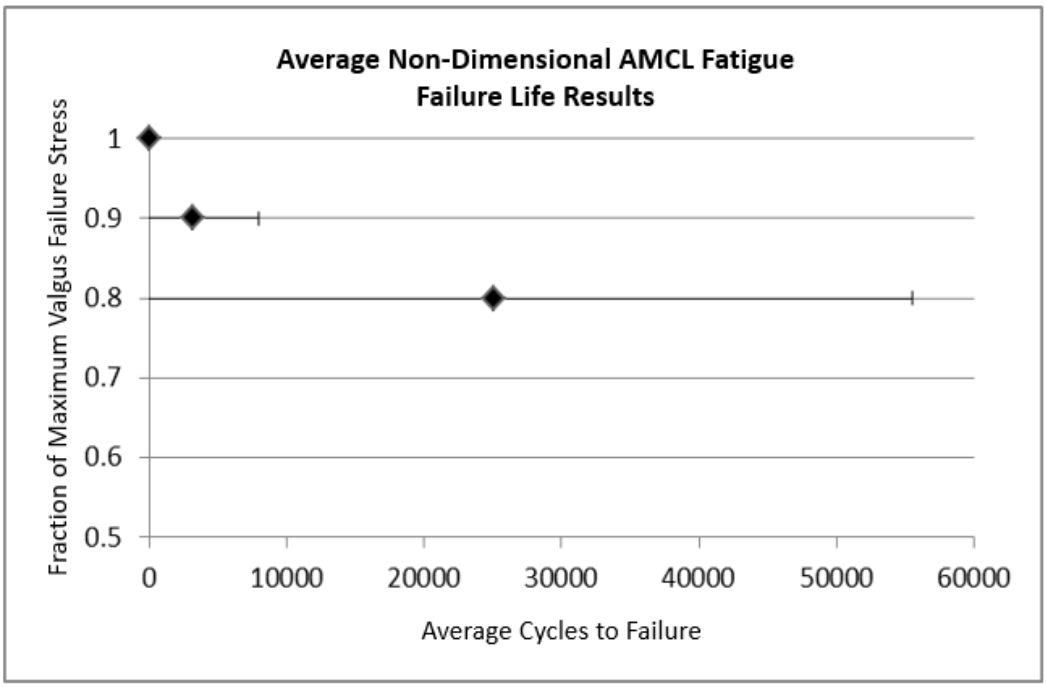

Figure 72: Non-Dimensional Average AMCL Valgus Fatigue Life Curve

The parameters γ and β of the exponential decay model (Equation 4-33) used to model the fatigue life curve are given in Table (3). The parameter r was equivalent to the average maximum number of cycles to failure at 80% of $\mathbf{M_f}$. The final modeled stress-based AMCL fatigue life curve is presented in Figure (73).

Table 3: Results for Exponential Decay Parameters

Exponential Decay Parameter [Stress Ratio]	Value
β	1.0004
γ	0.2375
r	25063
R^2	0.8144

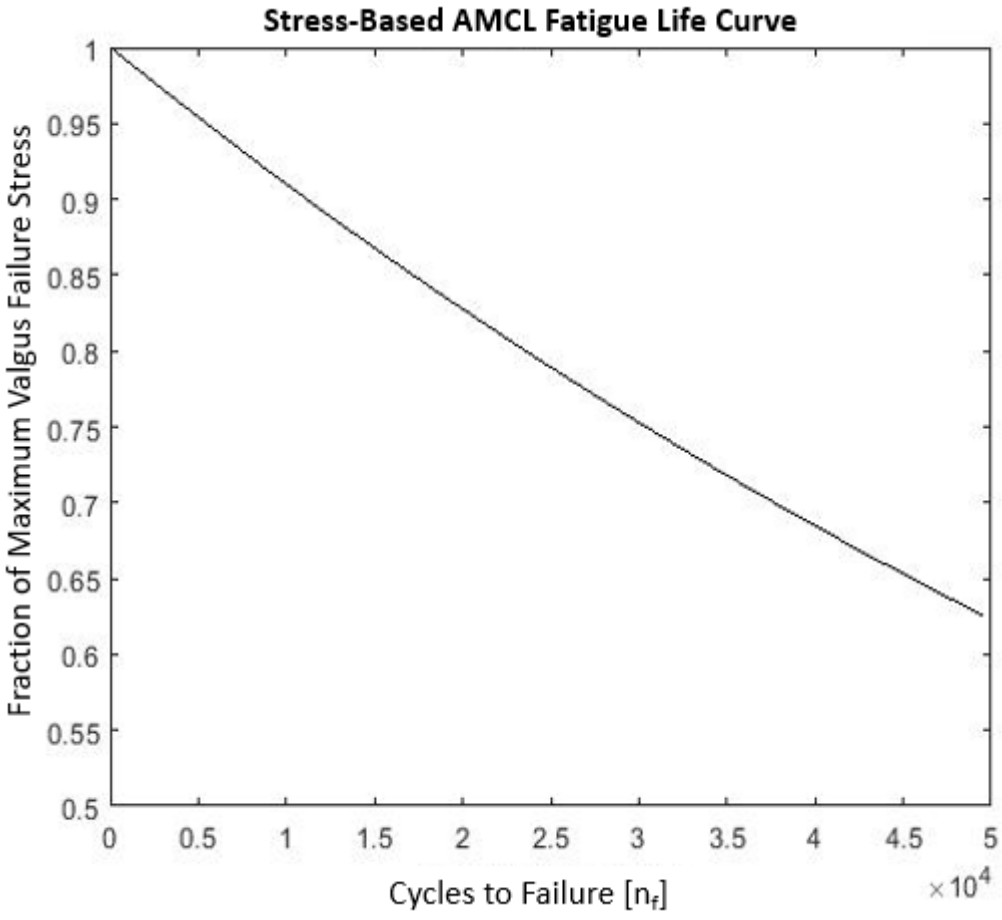

Figure 73: Stress-Based Non-Dimensional AMCL Fatigue Life Curve

The loss of stiffness was defined through the increase of rotation angle for each specimen during the test. The average initial angle θ_i, failure angle θ_f, and change in angle $\Delta\theta$, were $16.06^o \pm 5.55^o$, $20.83^o \pm 4.22^o$, and $4.77^o \pm 2.82^o$, respectively. These results are displayed in Figure (74).

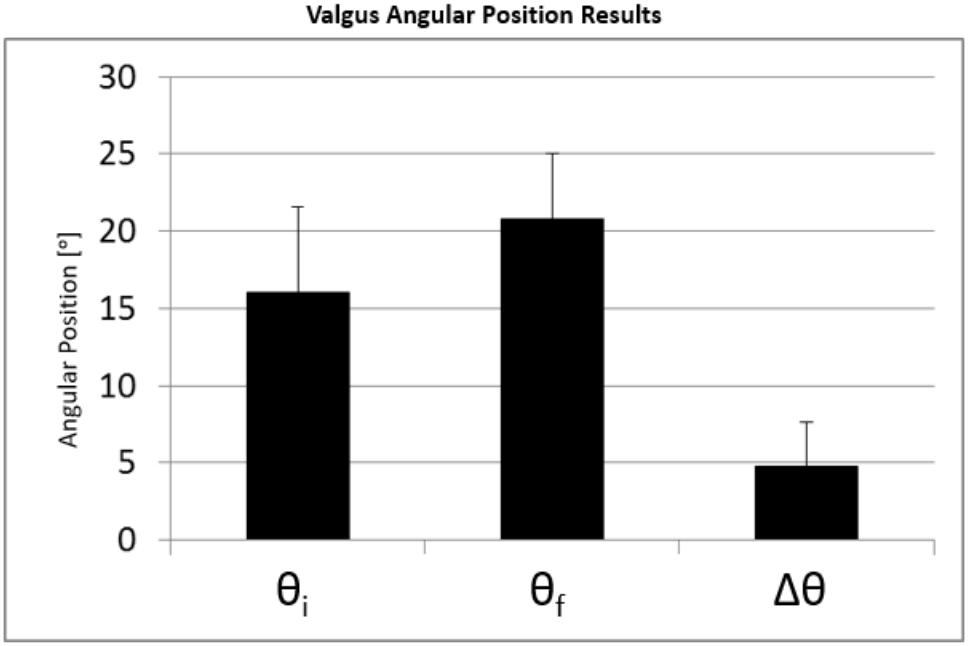

Figure 74: Angular Position Results

The change in the peak rotation angle for each specimen was used to fit a cubic damage model (Equation 4-5) for the experiment to formulate the nonlinear damage evolution curve (Figure 35). The parameters for the model are given in Table (4).

Table 4: Results for Cubic Damage Model Parameters

Cubic Damage Model Parameter	Value
A	2.2223
B	−3.1514
C	1.9291
E	0
R^2	0.9624

5.3.2 Fatigue Stretch Results

For each specimen, the stretching of the ligament throughout the cycling was measured by tracking the displacement of the markers along each of the three bands. In general, the maximum stretch of every specimen gradually increased as the cycling progressed. This behavior for the anterior, middle and posterior bands of a representative specimen (specimen 9) is shown in Figure (75). The stretch vs time plots for the middle band of three additional specimens (specimens 4,7 and 11) are shown in Figure (76).

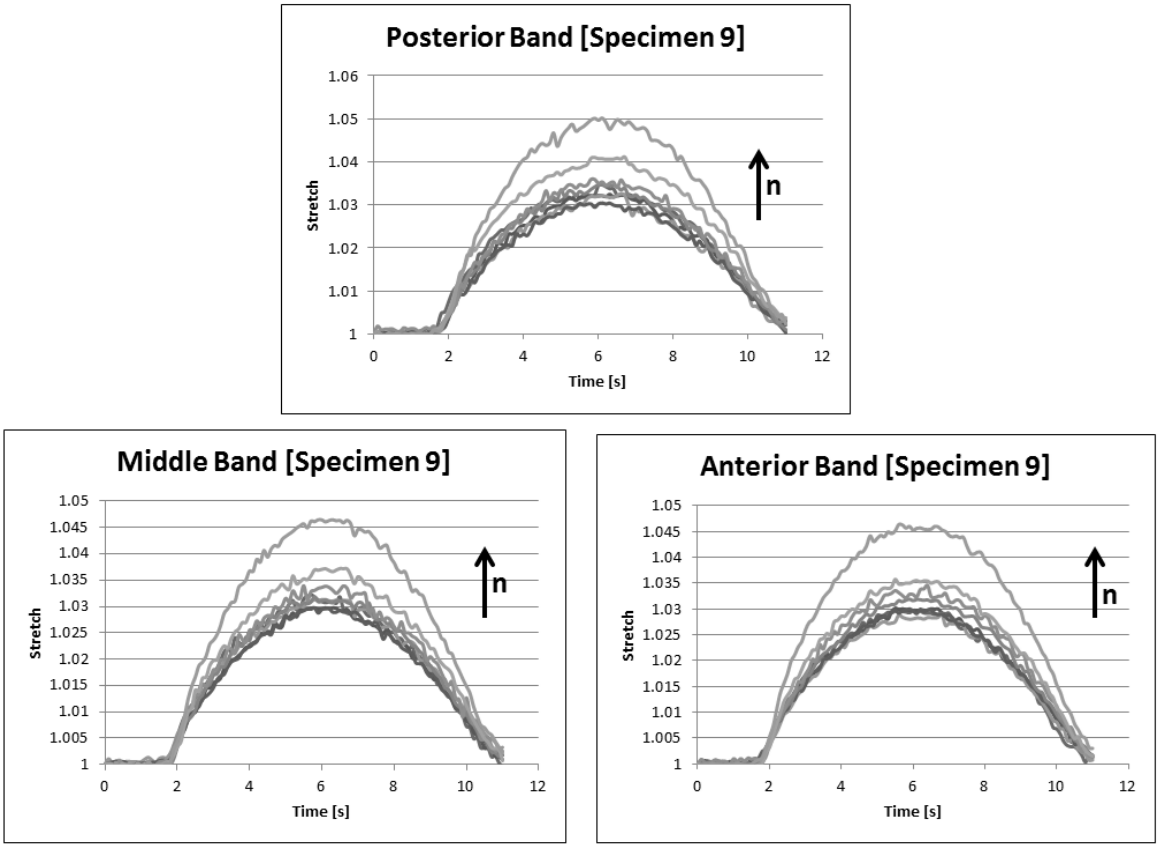

Figure 75: Fatigue Stretch Results for Anterior, Middle and Posterior Bands (specimen 9)

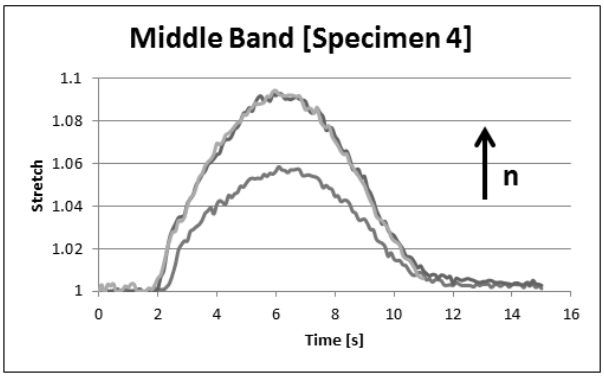

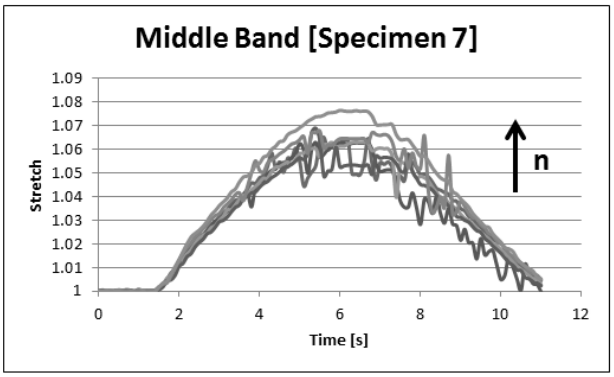

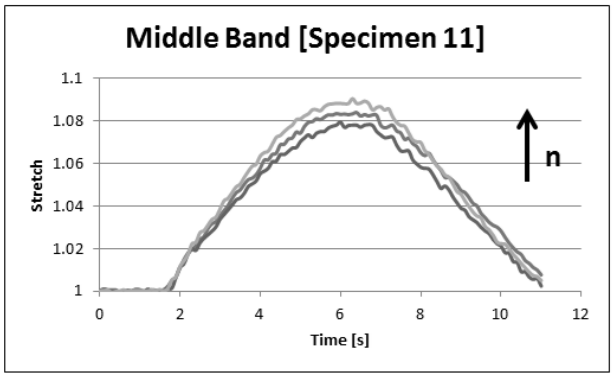

Figure 76: Fatigue Stretch Results for Middle Band (specimens 4,7 and 11)

The results for the average failure stretch for each band are given in Table (5). The overall increase in stretch, given as a percentage relative to the stretch recorded during the initial cycle to the stretch recorded during the last recorded cycle, is given in Table (6).

Table 5: Average Failure Stretch Results for Anterior, Middle and Posterior Bands

AMCL Band	Average Failure Stretch
Anterior	1.073 ± 0.018
Middle	1.077 ± 0.019
Posterior	1.066 ± 0.017

Table 6: Average Stretch Increase Results for Anterior, Middle and Posterior Bands

AMCL Band	Average Increase in Stretch [%]
Anterior	0.62 ± 1.28
Middle	0.89 ± 1.46
Posterior	1.03 ± 2.23

5.3.3 Stretch-Based Fatigue Life Curve

Similarly, as for the stress-based fatigue life curve, a non-dimensional stretch-based fatigue life curve (Figure 77) can be formed by taking the ratio of the maximum stretch at the first cycle and the maximum stretch at the failure cycle. A similar regression was performed for the exponential decay model of Equation (4-33) and the resulting parameters are given in Table (7).

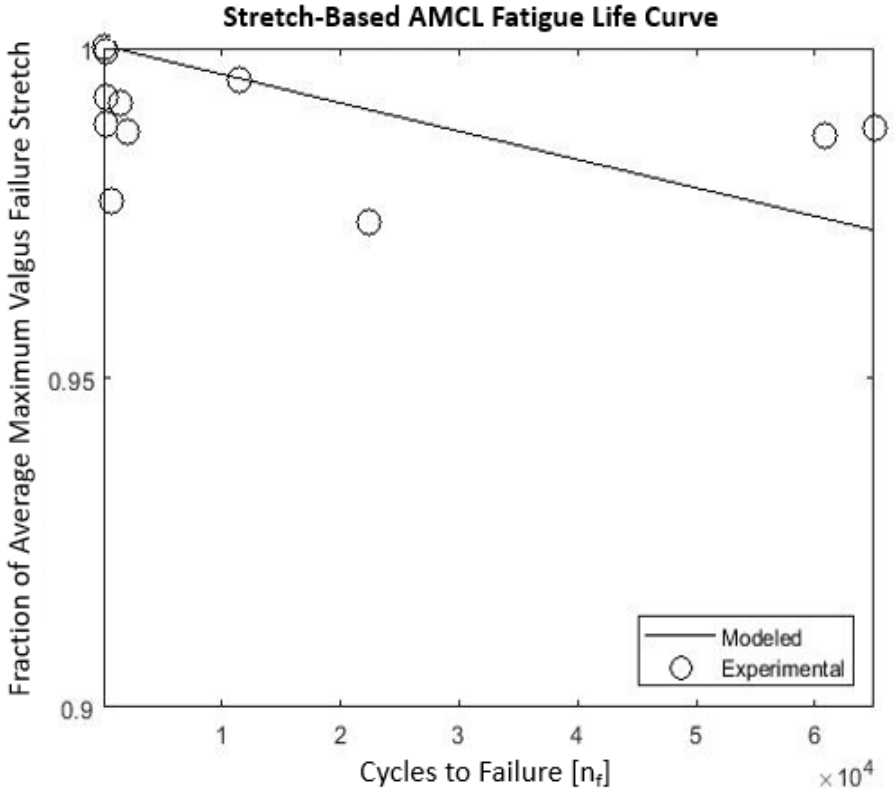

Figure 77: Non-Dimensional Stretch-Based AMCL Valgus Fatigue Life Curve

Table 7: Parameters for Stretch-Based Exponential Decay Model

Exponential Decay Parameter [Stretch Ratio]	Value
β	1.0004
γ	0.0110
r	25063
R^2	0.6367

5.3.4 Fatigue Failure Modes

Of the eleven specimens tested, three specimens failed by humeral avulsion. The failure mode was characterized by the tearing of the fibers from the base of the humerus insertion cite at the medial epicondyle. An example of this failure mode for one specimen is presented in Figure (78).

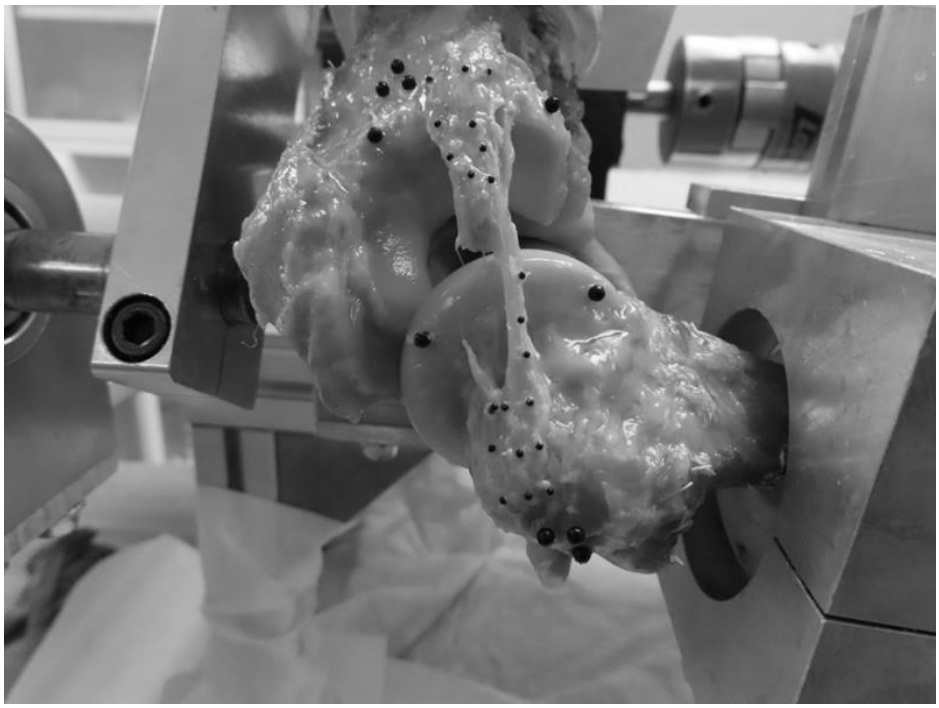

Figure 78: Humeral Avulsion Failure in Valgus Fatigue

Three specimens failed at the mid substance. Failure modes of this type originated on either side of the ligament at the mid substance and traversed across the width in either a diagonal or s-shaped pattern. An example of this failure mode for one specimen is presented in Figure (79).

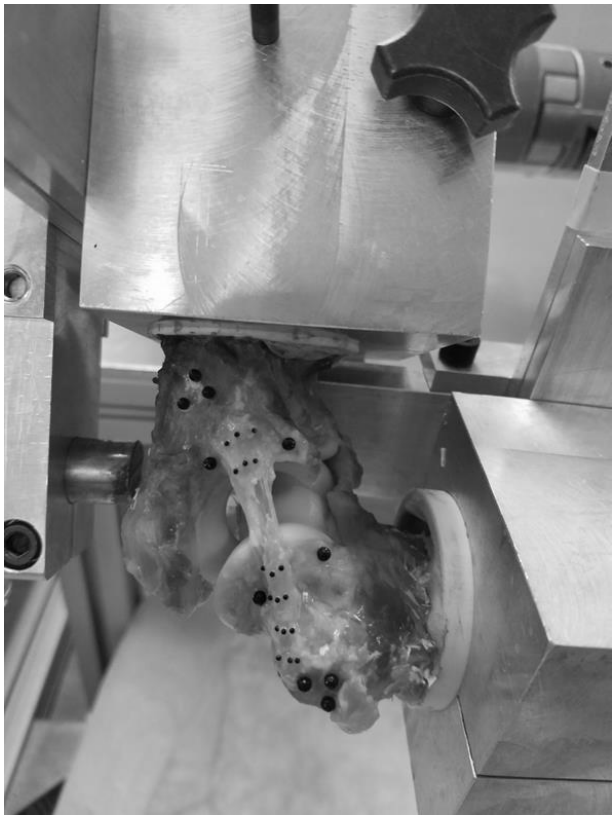

Figure 79: Mid-Substance Failure in Valgus Fatigue

Five specimens failed by ulnar avulsion. This failure mode saw the fibers disengaged from the base of the ulna insertion cite at the sublime tubercle. An example of this failure mode for one specimen is presented in Figure (80).

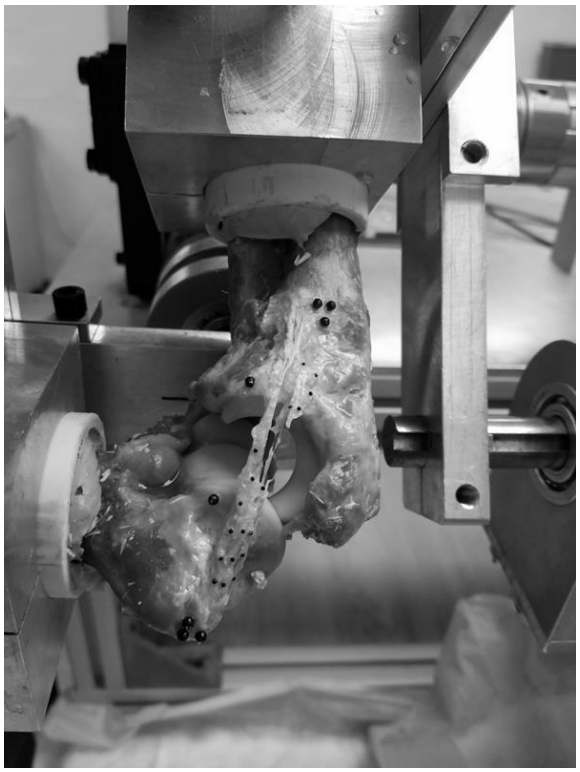

Figure 80: Ulnar Avulsion Failure in Valgus Fatigue

5.4 Finite Element Simulation Results

5.4.1 Mesh Convergence Results

The mesh size used for the analysis was 1. Mesh convergence was evaluated by changing the general element size by several orders of magnitude and observing the change in the stress-strain results. Mesh sizes of 500, 5, 1 and 0.5 were used for convergence analysis and the results are presented in Figure (81) and summarized in Table (8).

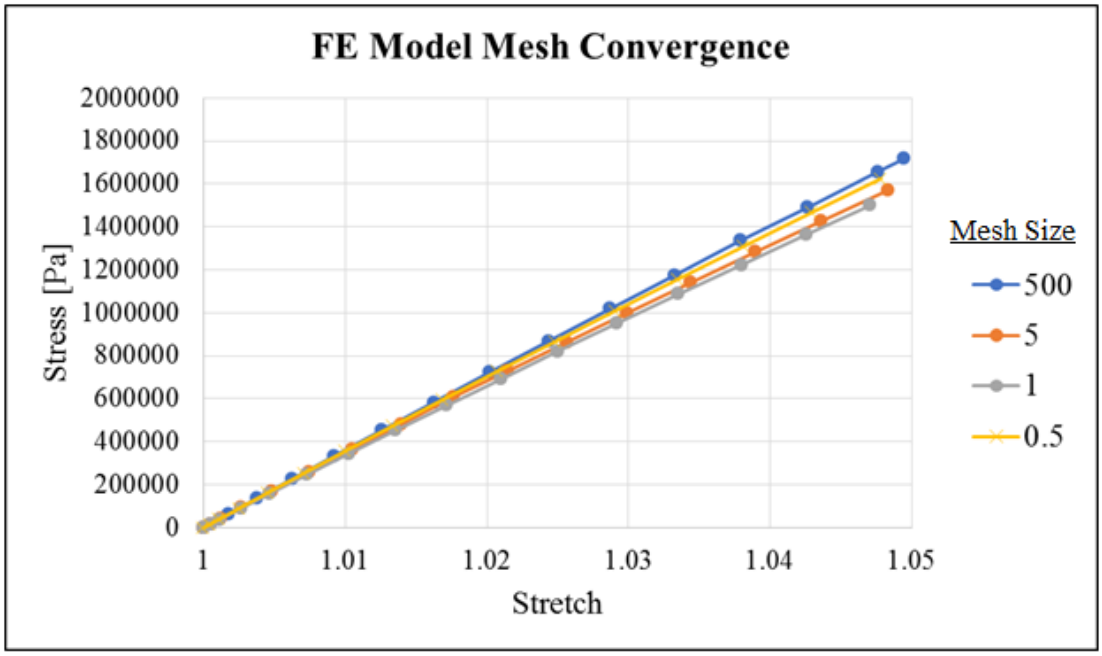

Figure 81: FE Model Mesh Convergence Results

Table 8: Average % Difference for Mesh Convergence

Change in Mesh Size	Average %Difference for each Time Step
500 to 5	17.6 ± 8.5
5 to 1	5.2 ± 0.7
1 to 0.5	5.1 ± 1.7

Mesh independence was observed for mesh sizes within the range of 5 to 1, where the difference in successive results was approximately 5%.

5.4.2 Elastic Simulation Results

For any particular specimen, the constitutive model parameters C_1-C_4 taken from the nonlinear regression were input into the model. After the vertical elongation, the results for the 1st deviatoric stress and strain were extracted for every element of the ligament. The deviatoric stress was chosen in post-processing because it gives the ligament stress in the absence of hydrostatic pressure.

The stress and strain values were averaged together at each time increment. These average stress and strain results, along with the results plus one standard deviation, were plotted together with the stress-stretch curve for that particular specimen for a visual comparison. Five representative results for specimens 2, 6, 8, 10 and 11 are presented in Figures (82-86).

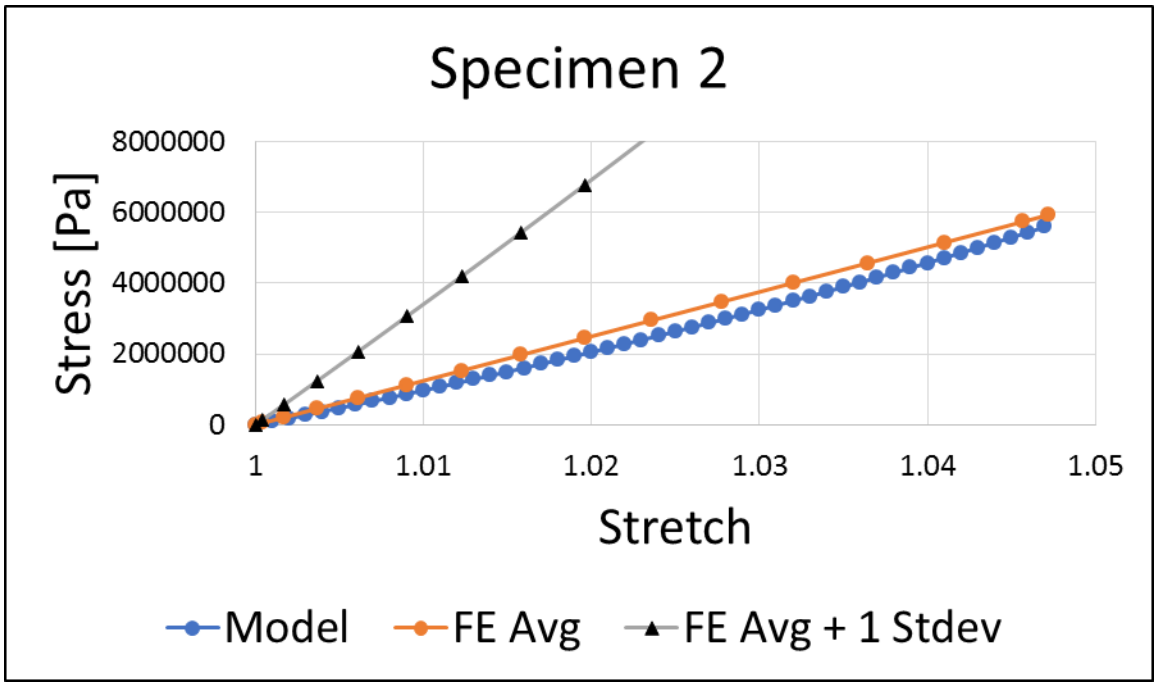

Figure 82: Specimen 2 Elastic FE Results

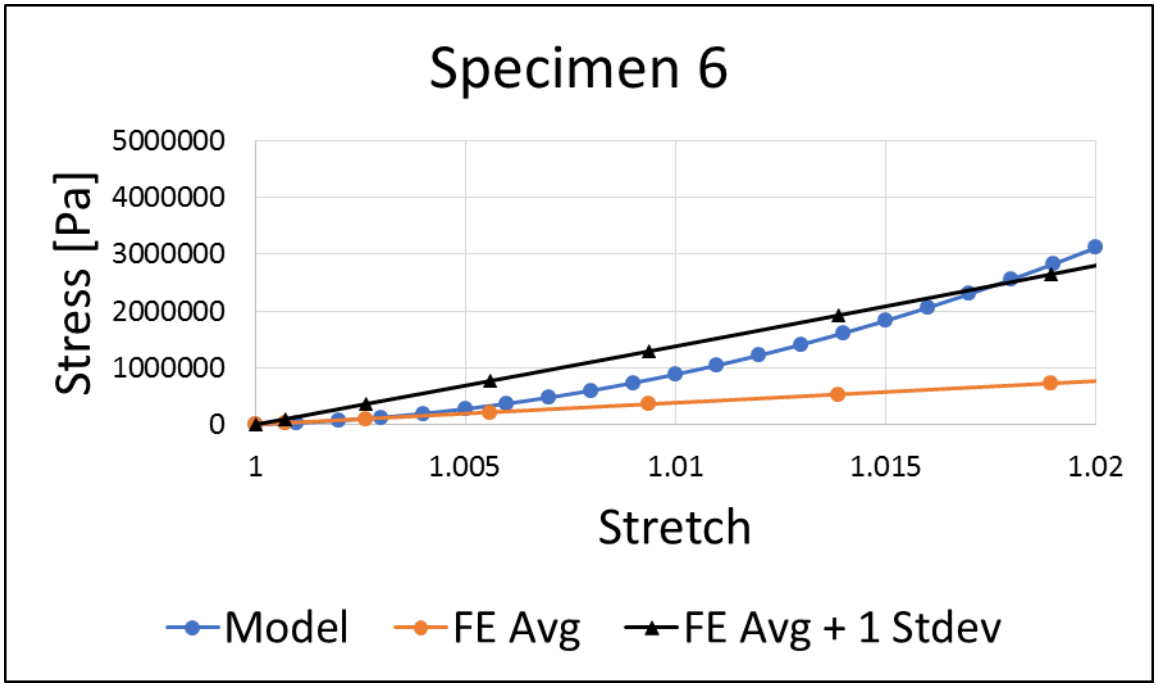

Figure 83: Specimen 6 Elastic FE Results

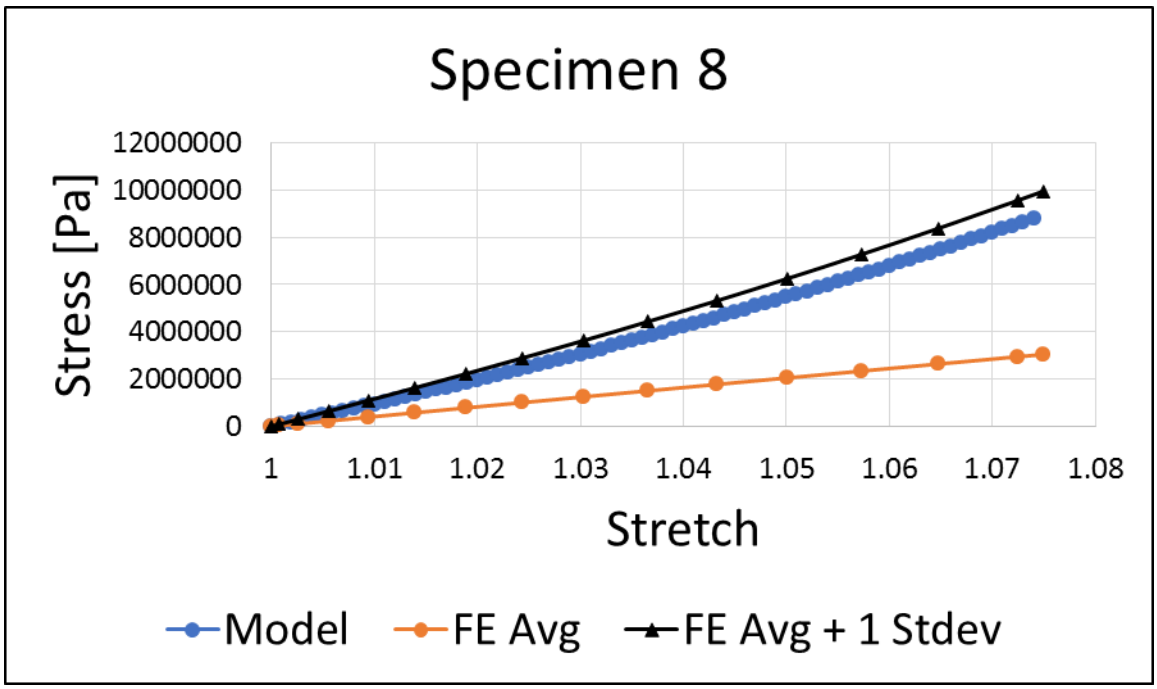

Figure 84: Specimen 8 Elastic FE Results

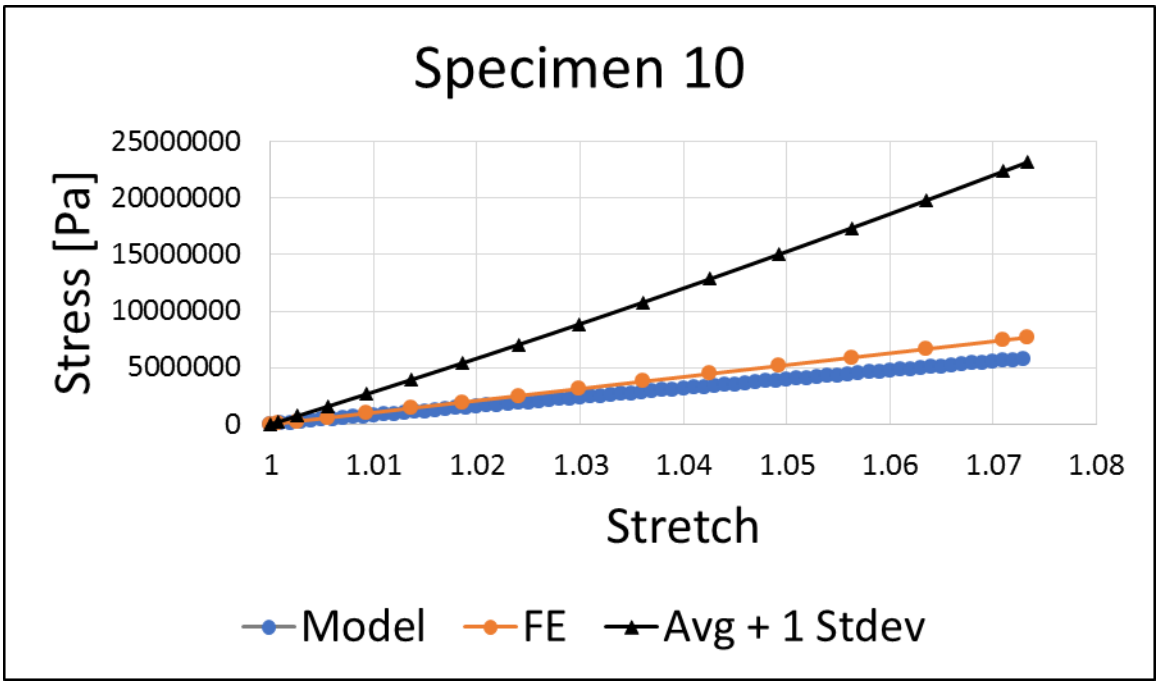

Figure 85: Specimen 10 Elastic FE Results

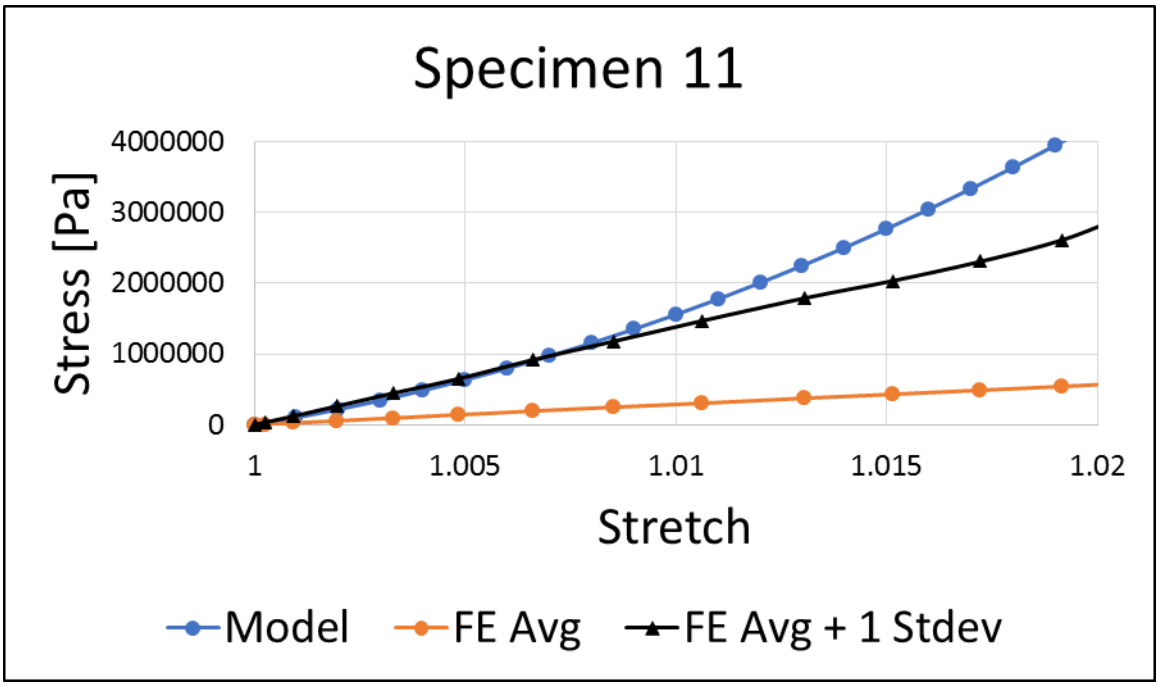

Figure 86: Specimen 11 Elastic FE Results

The agreement of the FE results with the experimental constitutive model was analyzed in terms of the percent difference between the constitutive model stress and FE stress at predisposed values of stretch. The stretch values, percent differences between the stress and the standard deviations are given in Table (9). Figure (87) shows how the percent differences progress with increasing levels of stretch.

Table 9: % Difference Results Stress and Given Stretch

Stretch	Percent Difference [Avg Stress]	Average Percent Difference [Avg Stress + 1 Stdev]
1.01	32.56 ± 74.21	28.58 ± 16.91
1.02	28.05 ± 73.68	29.67 ± 12.79
1.03	22.94 ± 76.04	15.65 ± 4.55
1.04	24.58 ± 70.44	17.23 ± 18.14
1.05	21.44 ± 74.33	8.02 ± 3.12
1.06	22.46 ± 71.48	8.13 ± 9.79
1.07	22.41 ± 69.84	9.01 ± 12.25

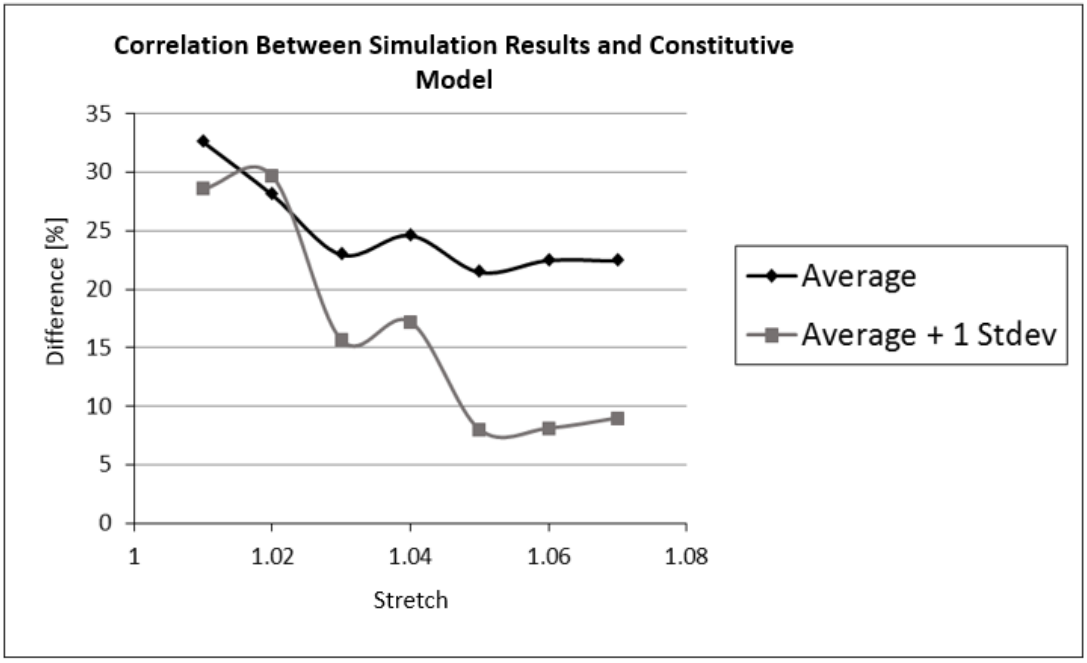

Figure 87: Correlation Between Simulation and Constitutive Model

5.4.3 Fatigue Simulation Results

The simulation of the fatigue effect was performed by imposing 2 mm and 3 mm randomized elongations on the eleven specimens. The maximum 1st principal deviatoric stress and stretch were recorded for that single cycle of elongation. This maximum stretch was then compared to the average maximum valgus failure stretch by forming a ratio of the two magnitudes.

This ratio then produced a maximum cycles to failure (n_f), using the stretch-based fatigue life curve of Figure (77). The exact number of cycles to failure was calculated using Equation (5-2), which is equivalent to Equation (4-33) with the dependent variable being the number of cycles to failure.

$$n_f = -\ln\left(\frac{S_n}{\beta}\right)\left(\frac{r}{\gamma}\right) \quad \text{.....[5-2]}$$

This value of n_f then scaled the abscissa of the damage evolution curve of Figure (35). This allowed the simulation to be repeated as desired to predict the mechanical behavior of the stress softened ligament after an arbitrary number of cycles. An example for specimen 10 is presented hereafter.

For the 3 mm distraction of the AMCL with elastic constitutive parameters corresponding to those of specimen 10, the average maximum 1st deviatoric principal stress was 7.69 Mpa. The average maximum 1st deviatoric principal stretch value was 1.073. From the experiments, the average maximum valgus failure stretch λ_f^{avg}, was approximately 1.077.

Because a direct conversion from the ligament stress experienced in vertical elongation and valgus rotation is not immediately obvious, the fatigue life curve based on the fatigue stretch ratio was used for fatigue life prediction (Figure 77). The stretch ratio r_λ , was calculated by taking the ratio of the maximum simulated stretch for one cycle λ_{max}^{FE} , and the average maximum valgus failure stretch λ_{max}^{EXP} (Equation 5-3). The ratio r_λ was equivalent to the ratio S_n.

$$r_\lambda = \frac{\lambda_{max}^{FE}}{\lambda_{max}^{EXP}} \quad \text{.....[5-3]}$$

The ratio was calculated to be approximately $r_\lambda \approx 0.997$. Using the stretch-based fatigue life curve, the cycles to failure for this percentage of load was predicted to be approximately 7754 cycles. With $n_f = 7754$, the damage evolution curve, was scaled appropriately (Figure 88), using the scaled version of the cubic damage evolution equation (Equation 4-5), Equation (5-4).

$$D\left(\frac{n}{n_f}\right) = \begin{cases} 0 & \frac{n}{7754} = 0 \\ A\left(\frac{n}{7754}\right)^3 + B\left(\frac{n}{7754}\right)^2 + C\left(\frac{n}{7754}\right) + E & 0 < \frac{n}{7754} < 1 \\ 1 & \frac{n}{7754} = 1 \end{cases}$$

.....[5-4]

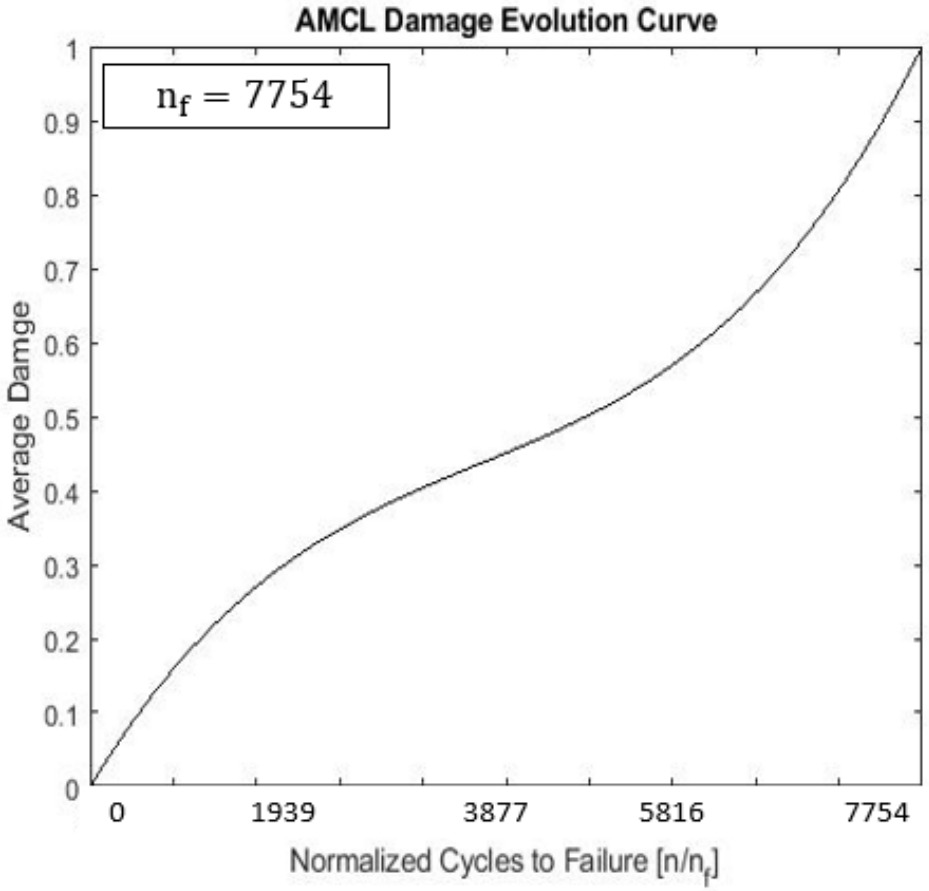

Figure 88: Scaled Damage Evolution Curve with n_f=7754

Using the scaled damage evolution curve, this allowed the fatigue simulations to be performed using the modified constitutive parameters of Equations (4-87 – 4-89). The damage scaling of these parameters was dictated by the number of cycles (i.e. pitches) performed and the corresponding incurred damage. The designated number of simulated cycles was chosen to

coincide with 0, 25%, 50%, 75% and 95% of the respective value of n_f for each specimen. The results for specimen 10 are presented in Figure (89). The legend entries give the number of cycles, the value of $\frac{n}{n_f}$ and the corresponding amount of damage.

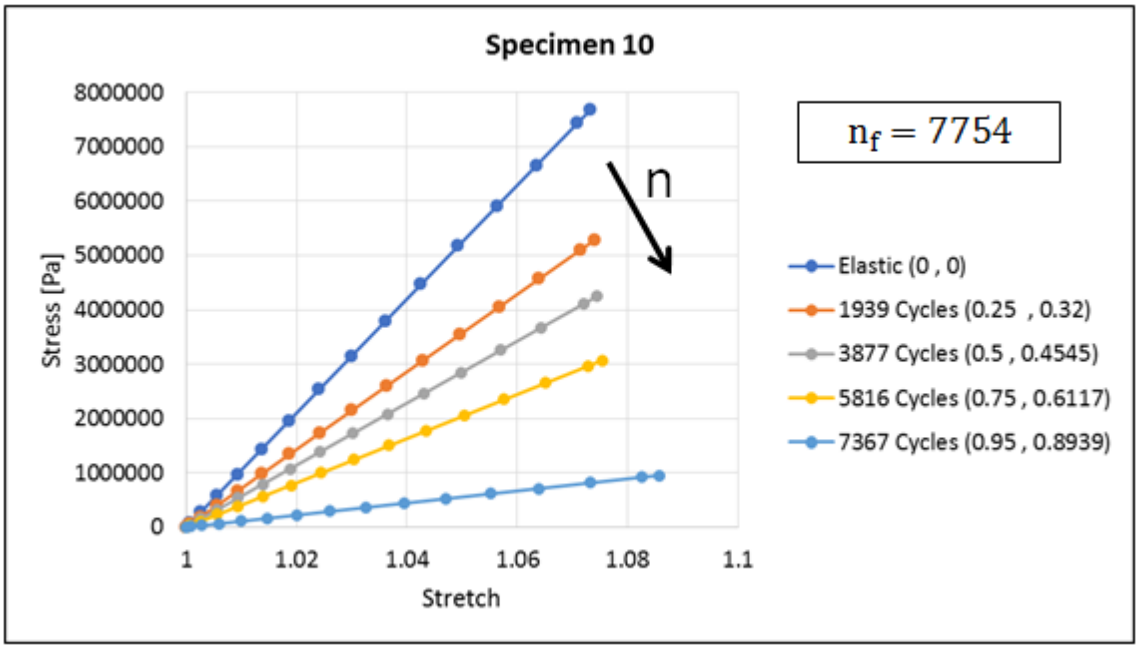

Figure 89: FE Fatigue Results for Specimen 10

For representation, the results for specimens 2 and 8 are also given in Figures (90-91), where the cycles to failure were calculated to be approximately 64054 and 4359 cycles, respectively.

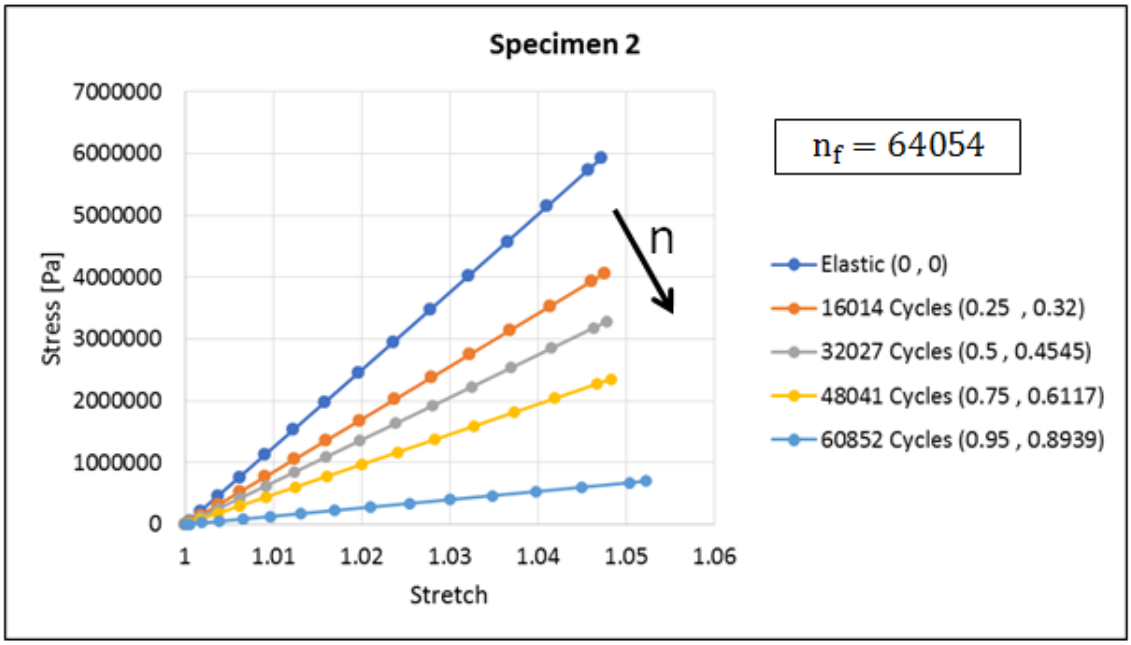

Figure 90: FE Fatigue Results for Specimen 2

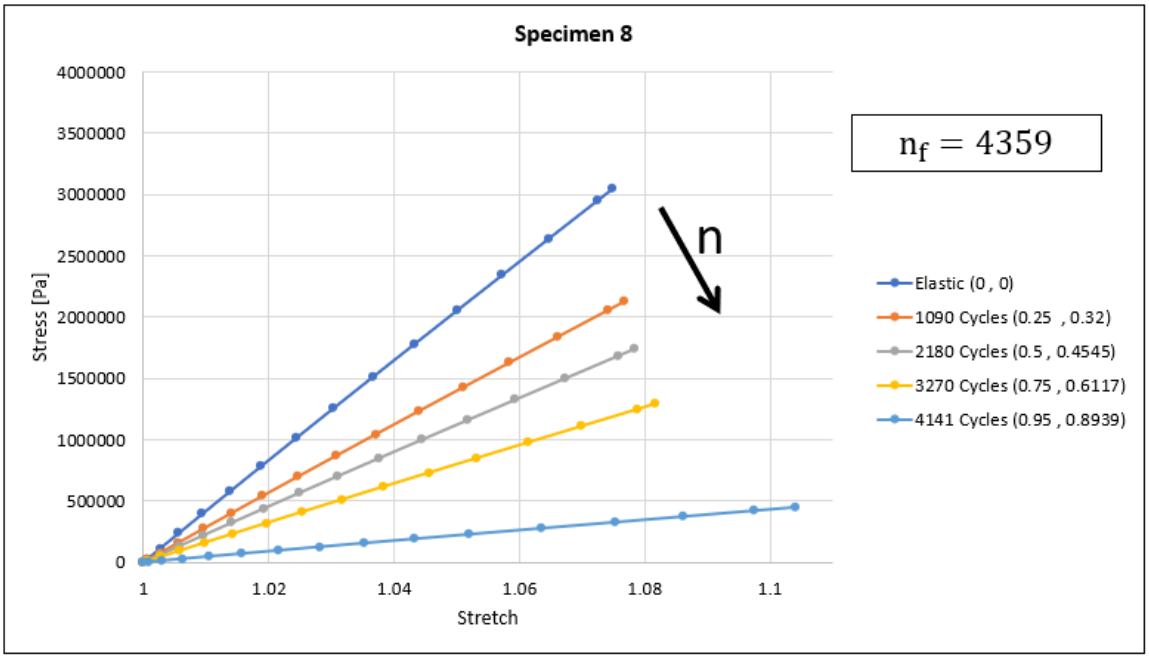

Figure 91: FE Fatigue Results for Specimen 8

Representative visualizations for the stress and strain distributions for specimen 10 for the cyclic cases of $\frac{n}{n_f} = 0, 0.5$ and 0.95 are shown in Figures (92-93). The increase in the maximum stretch, relative to the first cycle, was calculated for each of the simulated cycles and is presented in Figure (94). The decrease in the maximum stress was also calculated relative to the first cycle and is given in Figure (95).

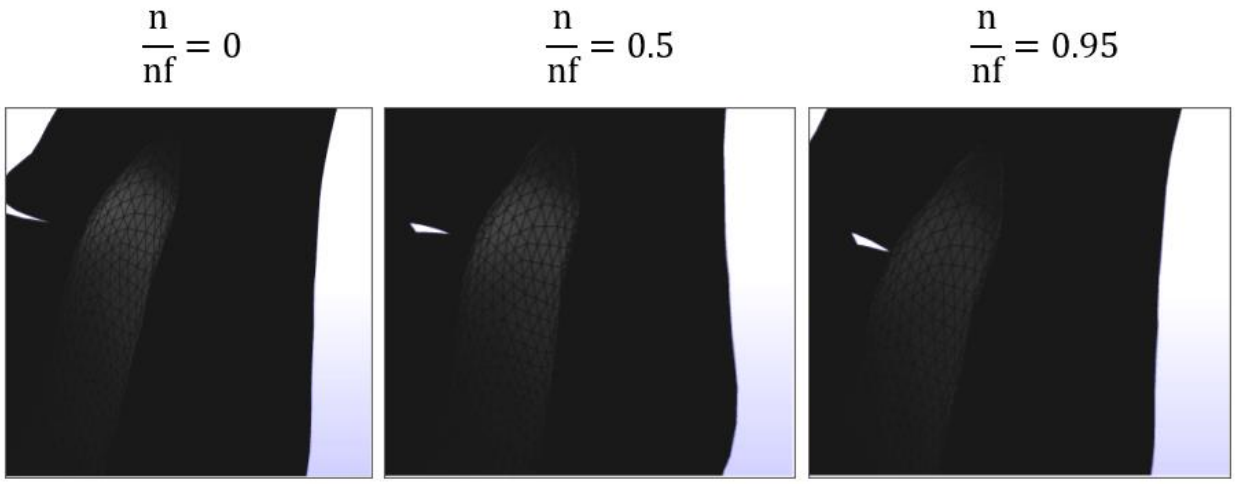

Figure 92: FE Stress Distribution for Specimen 10 for Representative n/n_f Cases

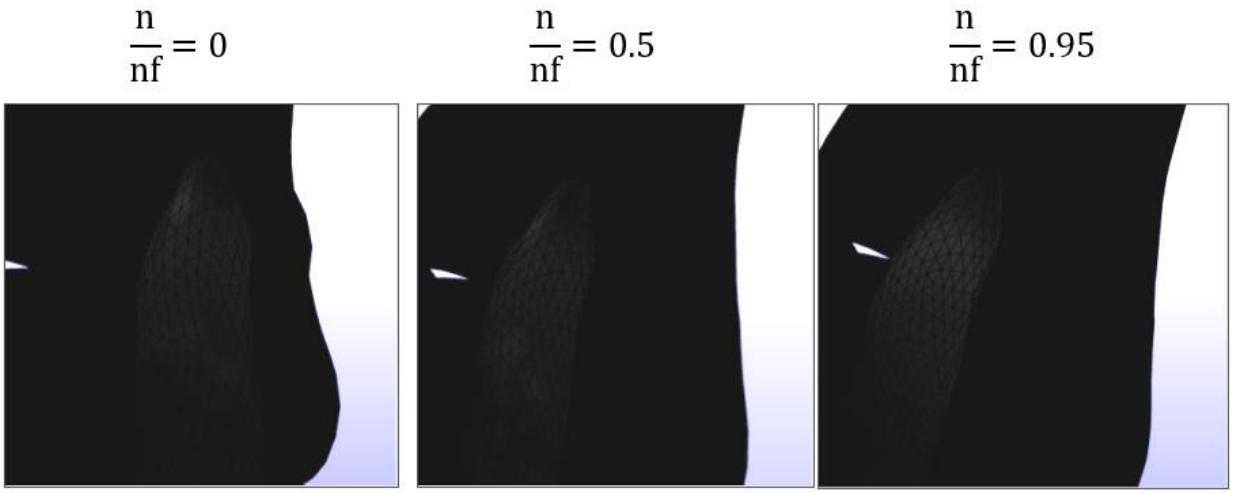

Figure 93: FE Strain Distribution for Specimen 10 for Representative n/n_f Cases

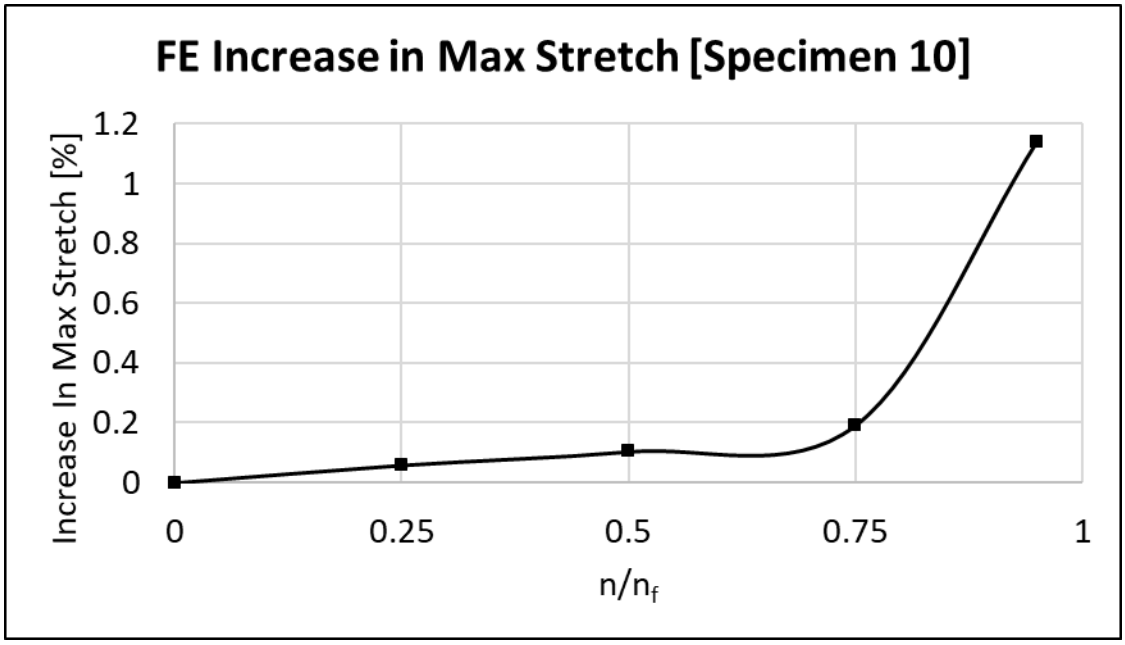

Figure 94: Increase in Max Stretch FE Results for Specimen 10

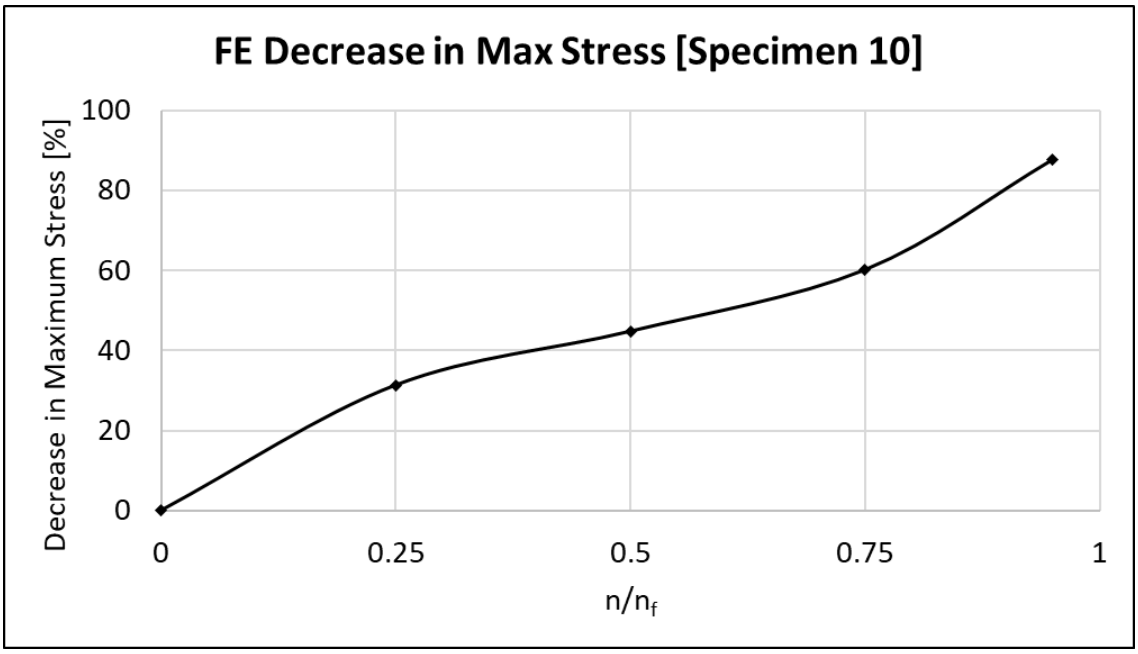

Figure 95: Decrease in Max Stress FE Results for Specimen 10

This simulation was performed for all eleven specimens. The average results for the decrease in maximum stress are presented in Figure (96).

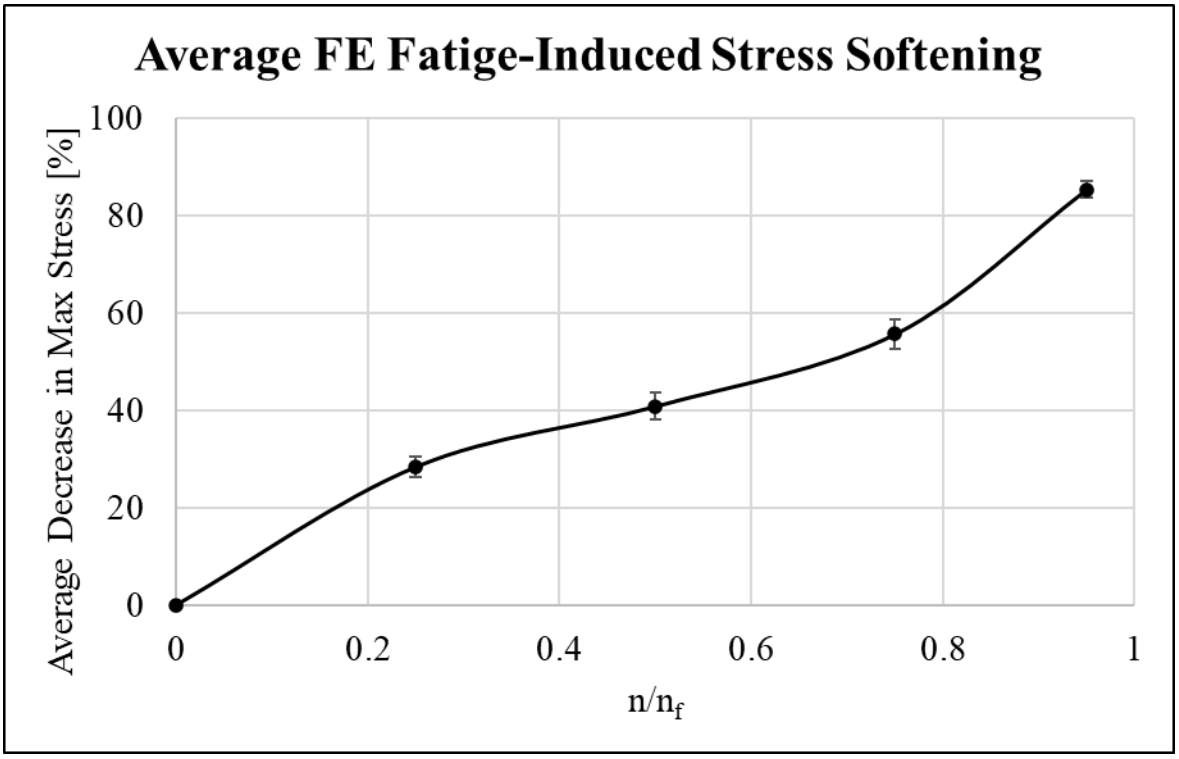

Figure 96: Average Decrease in Max Stress FE Results for Eleven Specimens

5.5 Validation

To validate the results, the increase in stretch from the simulation was compared to the increase in stretch measured during the experimental fatigue tests. The experimental stretch increases were given as average values calculated at 50% and 100% of cycle completion and are given in Figure (97).

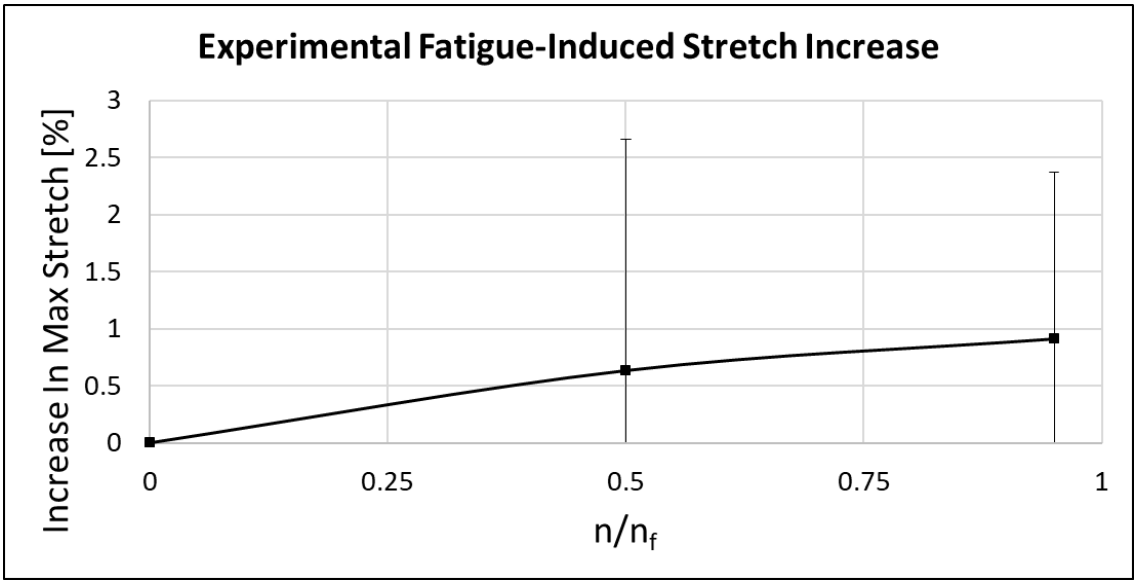

Figure 97: Average Experimental Stretch Increase Results

The increase in stretch for each simulated specimen was calculated at all of the simulated $\frac{n}{n_f}$ values and averaged together. These results, along with the experimental results are presented in Figure (98).

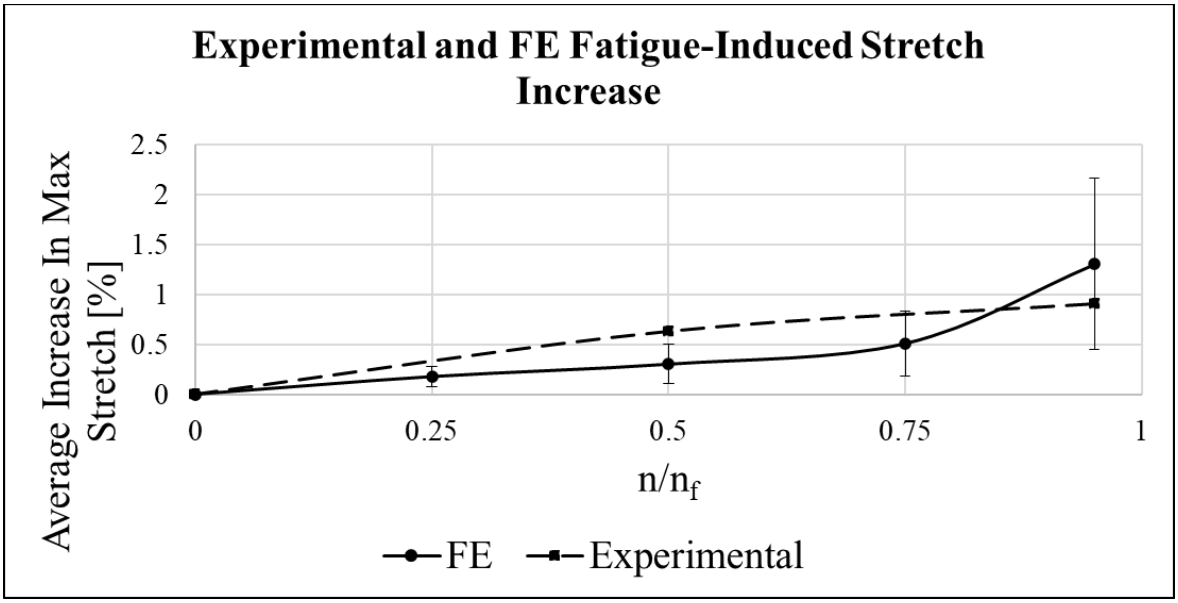

Figure 98: Average Experimental and FE Stretch Increase Results

The agreement between the simulation results and experimental results for stretch increase are summarized in Table (10).

Table 10: % Difference Results Between Experimental and FE Stretch Increase Results

Cycle Completion Percentage	% Difference
0	0
50%	0.522
95%	0.433

5.6 Elemental Cycles to Failure & Stress Softening

To visualize where along the AMCL failure was likely to occur as a result of repetitive cycling, a visualization of the model was produced in MATLAB. After running the FeBio simulation for the undamaged ligament, data for stress, strain and centroidal element position were extracted for each element. The positions of the element centroids were plotted in 3D for the initial and final positions of a 2mm displacement (Figure 99).

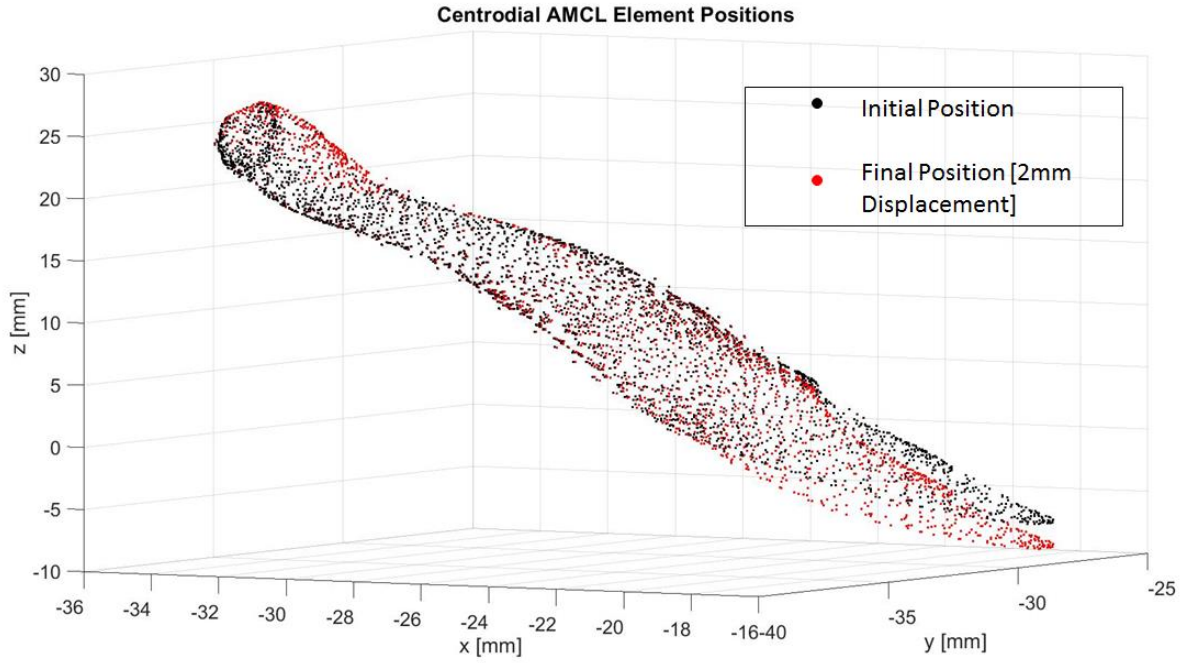

Figure 99: Elemental Centroid Coordinates

The maximum stretch data was recorded for each element and used to produce an individual cycle ratio r_{λ}^{e}, for each element given by Equation (5-5), where $\lambda_{max}^{FE^e}$ is the maximum stretch value for element e.

$$r_{\lambda}^{e} = \frac{\lambda_{max}^{FE^e}}{\lambda_{max}^{exp}} \quad \text{.....[5-5]}$$

Using the stretch-based fatigue life curve, these ratios were used to calculate individual cycle to failure estimates for each element, n_f^e. The maximum cycles to failure $n_{f_{max}}^{e}$, was extracted and taken as the limiting value for which each n_f^e was compared. The elements with n_f^e less than 10% and 25% of $n_{f_{max}}^{e}$ were identified and highlighted in Figure (100). Figure (100)

essentially shows the locations along the AMCL where fatigue failure is likely to occur first, for an equivalent level of 2mm cycling, for the simulated specimen.

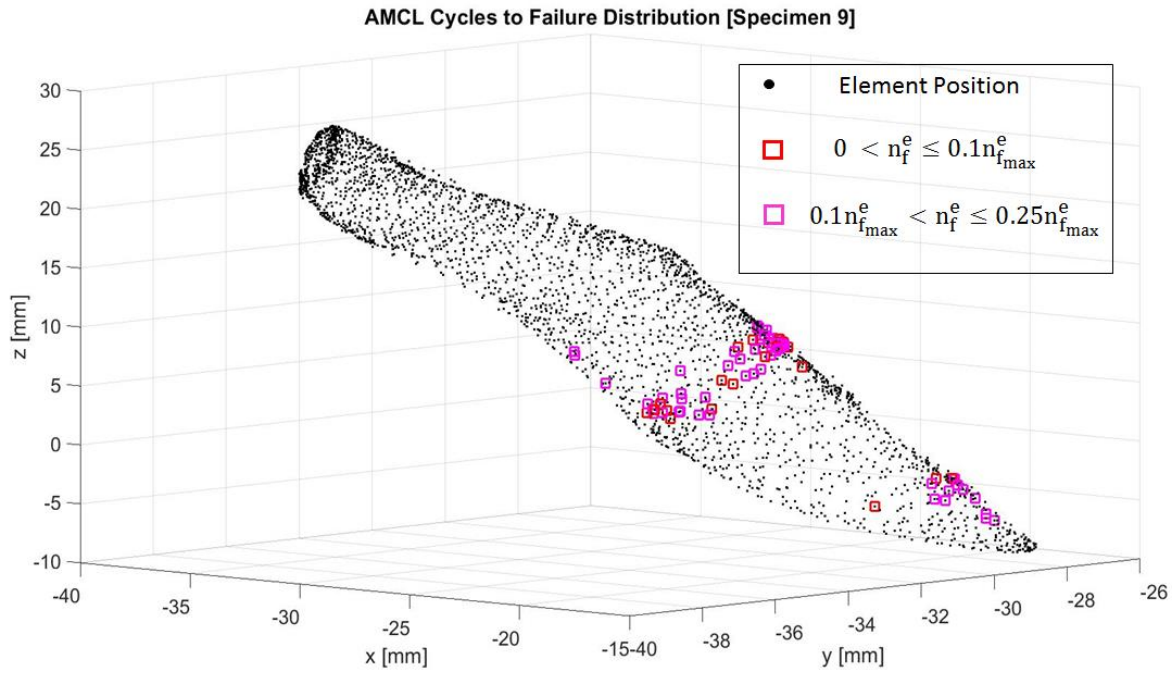

Figure 100: Predictied Locations of Fatigue Failure Initiation

Using the elemental cycles to failure values, a MATLAB script was used to sequentially damage the elements over the course of an arbitrary number of cycles. This elemental damage D^e, was defined individually for each element (Equation 5-6) by using the elemental cycles to failure values n_f^e.

$$D^e\left(\frac{n}{n_f^e}\right) = \begin{cases} 0 & \frac{n}{n_f^e} = 0 \\ A\left(\frac{n}{n_f^e}\right)^3 + B\left(\frac{n}{n_f^e}\right)^2 + C\left(\frac{n}{n_f^e}\right) + E & 0 < \frac{n}{n_f^e} < 1 \\ 1 & \frac{n}{n_f^e} = 1 \end{cases}$$

.....[5-6]

This allowed for the visualization of how the stress carried by each element softened as the cycling progressed. The number of cycles tested were 0, 25, 75 and 100. The maximum was chosen to be 100 because that is approximately equivalent to the standard number of overhand pitches thrown in a regulation baseball game by a single pitcher.

To determine how the stress was changing, the difference r_σ^e, between the maximum element stress at the first cycle σ_o^e and the maximum element stress at the current cycle σ_n^e, was calculated using Equation (5-7).

$$r_\sigma^e = 1 - \frac{\sigma_n^e}{\sigma_o^e} \text{.....[5-7]}$$

The results for each of these cyclic steps are shown in Figures (101-104). The circles designate changes within a specified range of r_σ^e. The red cross symbols designate the elements where the decrease in stress was greater than 50%.

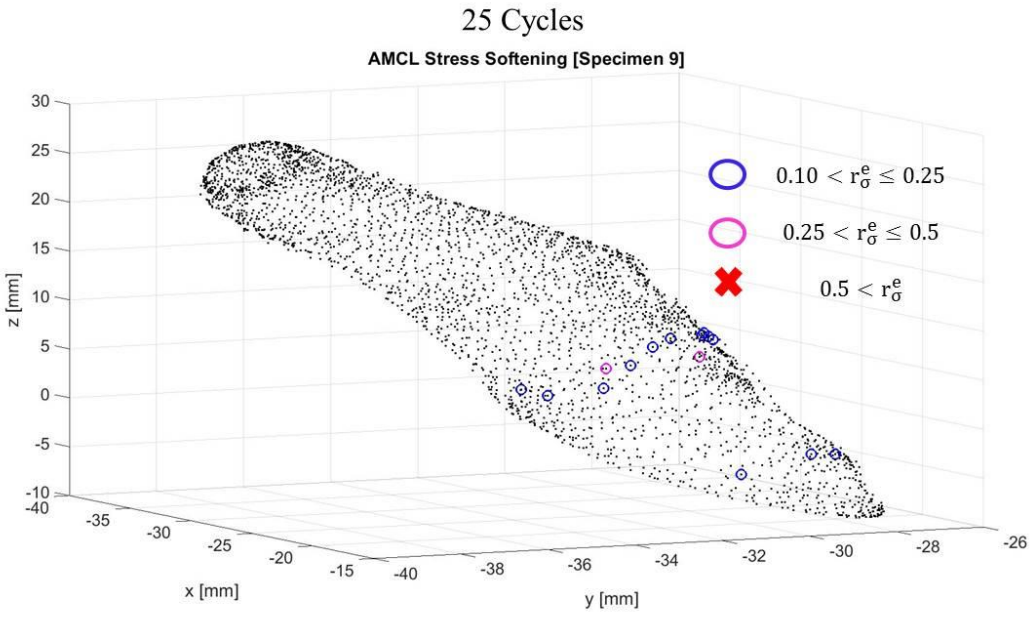

Figure 101: Elemental Stress Decrease (25 cycles)

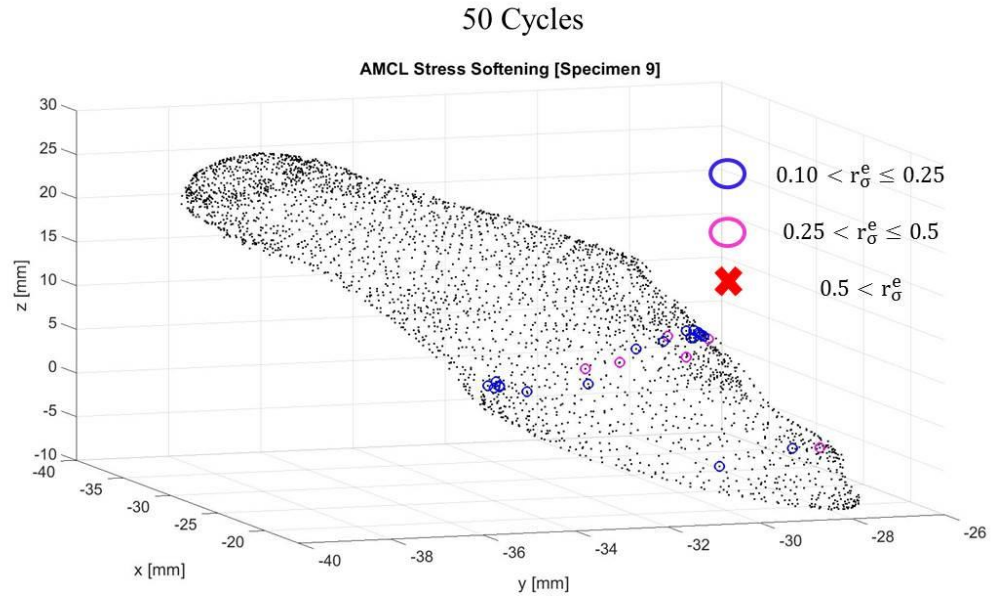

Figure 102: Elemental Stress Decrease (50 cycles)

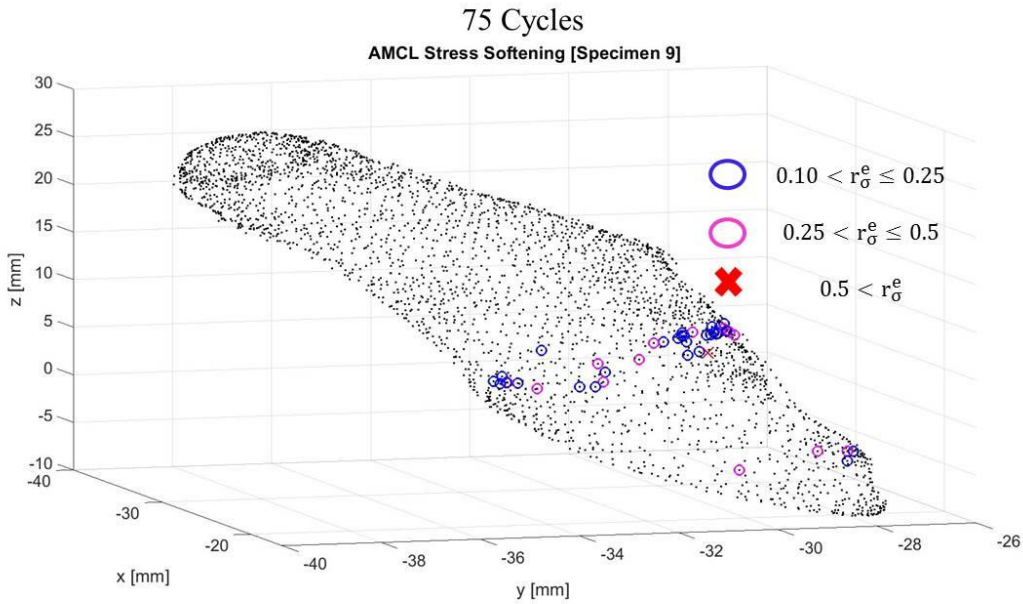

Figure 103: Elemental Stress Decrease (75 cycles)

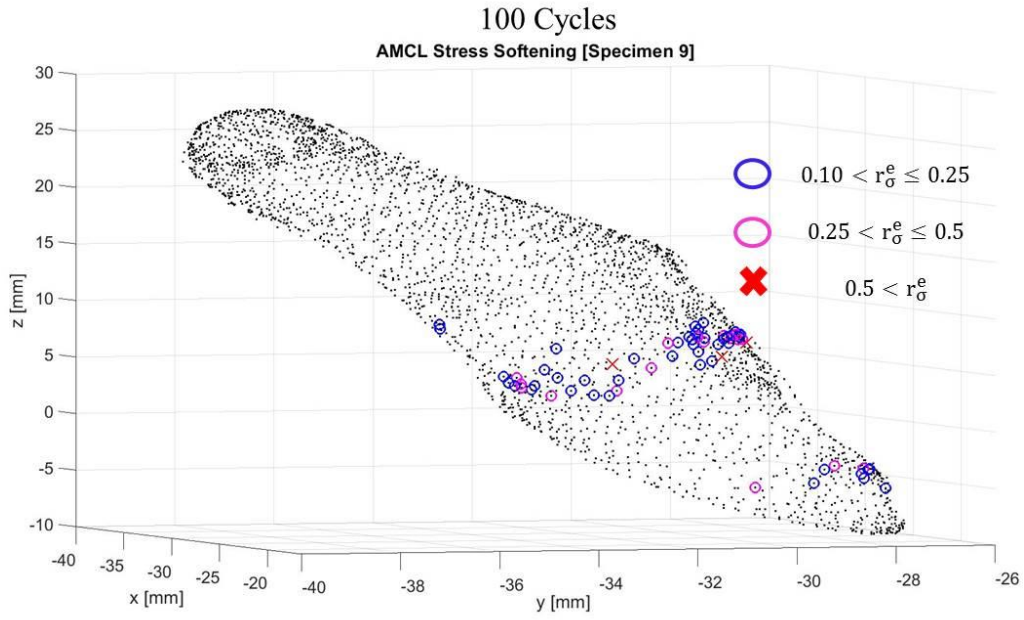

Figure 104: Elemental Stress Decrease (100 cycles)

6.0 Discussion

6.1 Anatomy

The average measured width of the AMCL distal to proximal was $8.52\ \text{mm} \pm 1.84$ and $5.7\ \text{mm} \pm 1.21\ \text{mm}$. These results fall within the range of previously reported values of approximately 4 – 8 mm[81-83]. The observation that the width of the ligament changes along its length was not a new one, and gives the ligament a tapered surface toward the insertions, as was observed in the ACL of the knee[84].

The thickness of the AMCL distal to proximal was between 2.11 mm and 2.44 mm. These thickness measurements fell within the range of previously reported averages of approximately 2 to 3 mm[85]. Ultrasonic measurements using various techniques have reported slightly smaller measurements of about 1.4 – 1.9 mm[86]. This difference can be attributed to uncertainty in mechanical measurements and the manual operation of measuring devices.

The discrepancy in the thickness values between the distal and proximal ends was not as large as the difference in widths. This would suggest that changes in the cross-sectional area of the ligament and, therefore, the amount of stress that can be carried by different sections of the ligament along its length, is more immediately affected by the width. The implications on the regional mechanical strength of the ligament are apparent, as sections of the ligament with greater cross-sectional area would be stronger. This was shown to be true in a transection study involving the ACL, showing regional variations in the mechanical properties of the ligament are indeed possible[69]. This would affect the tendency of the ligament to fail at a specific location.

This variability in width also affects the surface area of the ligament. Previous studies have measured the surface area at the ulna and epicondyle insertion cites to be dissimilar with the ulnar area being approximately 128 mm^2 and the epicondyle area being approximately 45 mm^2[83]. Whether the ligament fails due to ulnar or humeral avulsion could be influenced by the effective surface area of the ligament at these respective sites.

This result can also be significant in the construction of future models where parametric studies are performed based on minute model variations. Knowing that the width is the most critical geometric component can save computation time by eliminating the need to study effects due to variations in other features, such as thickness and length.

6.2 Elastic Testing

6.2.1 Tensile Failure Loads

The average AMCL failure load for the specimens tested at ninety degrees of flexion was $595.25\ N \pm 201.93\ N$. This range of results was significantly greater than the previously reported AMCL tensile failure load of approximately $260\ N \pm 71.3\ N$ [87].

Several factors could have been responsible for this difference. The first factor was loading rate. The current work loaded the specimen at a uniform rate of 0.5 mm/s for all specimens, while the previous work [87] loaded each specimen at a variable rate dependent on the initial ligament length.

The second factor could have been the loading configuration. The current work loaded each specimen in a vertical direction aligned with the centroidal axis of the ulna, while flexed at

ninety degrees. The previous work [87] loaded the specimen in a manner consistent with the long axis of the ligament. The difference in loading configuration could have produced different states of stress within the specimens, causing them to fail at different load magnitudes.

Having the loads aligned with the ligament long axis could produce lesser failure loads, because most of the load magnitude would be aligned with the elongation direction of the ligament. If the axis of the load and principal direction of the ligament have some misalignment, then less of the load magnitude would influence the elongation of the ligament, possibly leading to higher failure loads.

6.2.2 Tensile Testing Failure Modes

Avulsion at the medial epicondyle of the humerus and at the sublime tubercle of the ulna accounted for five and six of the respective failure modes for each specimen. Avulsion of the ligament fibers from their boney insertion or origins is an injury commonly found amongst ligament tears. In the anterior cruciate ligament (ACL) of the knee, root tears of the lateral meniscus can be found in approximately 7-12 % of cases [88]. MRI was the primary means of identifying these injuries[89]. In a study involving 264 patients, 12.8% of the ACL tears were characterized by root tears, either laterally or medially[90].

The prevalence of these failure modes in the torn ligaments of patients can be intuitively reasoned. The insertion and origin cites are the anchors of the respective ligament and the point of direct load transmission from the bone to the ligament. The mismatch of material properties between the collagenous tissue and cartilage of the bone can act as a stress riser, increasing the likelihood of failure at that location.

Whether the avulsion occurs at the origin or insertion could depend on the footprint, or surface area of the ligament at that location, as well as the cross-sectional area. The average width and thickness for the tested specimen were dissimilar, but not by a large margin. This could explain why nearly an equivalent number of specimens failed proximally and distally.

6.2.3 Constitutive Model Parameters

The average results for the four parameters C_1-C_4, of the transversely isotropic Mooney-Rivlin constitutive equation used to model the AMCL stress-stretch behavior were given in Table (2). The magnitudes of the average values for C_1 and C_2 were on the order of 1E6. With the value of stress being on the order of approximately 1E6, it sufficed that the magnitudes for C_1 and C_2 would be of a similar magnitude, given the form of the Cauchy Stress Tensor (Equation 4-20), where C_1 and C_2 multiplied the linear portion of the constitutive model.

In the strain energy function, the parameters C_1 and C_2 were presumed to represent the strain energy function for the isotropic matrix material[45, 46]. These constants accompany the first and second invariants. Inclusion of the second invariant and, thus, C_2 has been shown to be critical when looking to fully represent the non-homogenous deformation behavior of fibrous materials[91]. The results of the eleven tested specimens agree with this premise, as shown by the average magnitudes of C_1 and C_2, which are roughly equivalent. This suggests that both parameters were equally important in capturing the mechanical response of the matrix material.

The average magnitude of C_3 was on the order of 1E8. This was two orders of magnitude greater than the average values for C_1 and C_2. In the additive form of the strain energy function, C_3 was the stress multiplier for the strain energy function of the fibers[45, 46]. The higher magnitude for C_3 suggests that the mechanical response provided by the fibers was greater than

that provided by the matrix. Also, it suggested that the contribution to the strength of the AMCL was greater from the fibers than that from the matrix material. This is indeed the case, as the fibers are the primary load bearing structures in the ligament.

C_4 was the exponential coefficient and was taken as the fiber scaling parameter[45]. The average magnitude was on the order of 1E1, which was significantly less than those for C_1-C_3. As C_4 multiplies the exponential input, it was seen as a control parameter for fiber crimping. The larger the value, the faster the fibers straighten and the quicker the exponential function grows. With an average C_4 value of approximately 1.26, this suggested that the fibers of the AMCL tended to straighten fairly slowly. This was evident in the mechanical responses observed for the specimens which displayed a primarily exponential response, although a fair number of specimens did display a completely linear behavior.

The average correlation coefficient between the constitutive model and experimental data was approximately 0.992. This suggested that the utilized model was sufficient in fitting the experimental data.

6.3 Fatigue Testing

Every specimen tested was free from any known defects such as prior elbow damage and other various health ailments. There was one specimen which was not tested due to calcification at the proximal end and a capitellum fracture.

The results for the fatigue life of the tested specimens had very high variability. This was expected given the variable nature of biological materials. Every ligament had slightly different

geometric properties, which could undoubtedly create some structural differences, leading to the mixed results.

Other factors, such as specimen age, could have contributed to the differences as well. Older individuals are generally physically weaker than younger individuals. Even specimens of the same age can differ greatly in their respective biological age, which reflects factors such as individual wear and tissue damage. For example, a 40-year-old specimen who was a pro pitcher for 15 years, would have a UCL with significantly more wear than a 40-year-old non-athlete. This was shown in a study involving age-identical birds exposed to experimental stressors which produced noticeable changes in several biological age biomarkers, as compared to a control group. [92].

Not only was there a wide variety of fatigue life results, but there was also a large disparity in the individual fatigue life magnitudes. At least three specimens each were within the ranges of 10^2 through 10^3, 10^3 through 10^4, and 10^4 through 10^5 cycles to failure. The specimens tested were randomized in terms of right and left elbows. The hand dominance of the specimens was not recorded. This would mean that some specimens tested could have been the dominant upper extremity, while others could have been the non-dominant extremity. Regarding hand strength, it has been shown that the dominant hand is typically stronger than the non-dominant counterpart[93]. Regarding ACLs, the effect of limb dominance was inconclusive in the identification of primary mechanical risk factors[94]. These findings make the topic of limb dominance interesting, and a potential, yet undetermined influencer of fatigue life.

The average overall applied valgus torque for each specimen was 21.4 Nm. This was much less than the reported valgus failure torque of the UCL of 64 Nm[7]. This result was also significantly less than the reported maximum valgus load experienced at the medial elbow during

standard pitches for adolescent baseball pitchers[16], 47.3 Nm for fastballs and 44.2 Nm for curveballs; and professional baseball pitchers[95], 54.3 Nm for fastballs and 52.1 Nm for curveballs. This corroborates the general knowledge that fatigue leads to failure at loads which can be less than the typical performance strength and the ultimate failure strength of the material.

The individual valgus torques produced an expected observation, which was a higher rotation angle for higher values of valgus torque. These two variables showed a similar correlation and have a significant relationship when it comes to overhand throwing mechanics[96]. These variables can have some biological dependence, as a thicker, more stiff, ligament may produce a lesser angle of rotation than a thinner, less stiff, ligament cycled at a lower magnitude of torque.

The angular position of the tested specimens increased by an average of 22.9%. The increase in position over time was a result experienced in multiple fatigue tests. In a study involving the tensile cycling of rabbit MCLs, the average displacement increased by approximately 45%[97].

This increase in angular displacement can also be an indicator of non-passive valgus laxity. Non-passive valgus laxity under an imposed valgus torque has been shown to depend on the flexion angle of the elbow[81]. With all of the specimens in the present study being tested at 90˚, it was not possible to study and compare this effect. However, given the results of the previous study by Safran et al., it can be reasoned that the results for the average increase in angular position may be different for other flexion angles.

The increase in valgus angle over repeated cycling can have immediate implications on joint spacing. Ultrasonically, the joint space at the medial elbow has been shown to increase under valgus loading[98]. Qualitatively, this was also observed during testing. With the humerus held relatively static, the rotation of the ulna caused the joint to open up. The degree of joint opening

grew slightly larger, as discernable by visual inspection, as the cycling progressed to larger values. This opening of the joint may produce some unforeseen health concerns by possibly placing additional stresses on the boney constructs of the elbow or the surrounding muscles which have been shown to deteriorate in mechanical performance as a result of imposed fatigue protocols[99].

The increase in rotational displacement was used to characterize the damage in the AMCL, as opposed to the measure of ligament stretch, because it was more consistent. While the stretch measured for the final tested cycle was always larger than the measured stretch at the initial cycle, giving a positive value for the reported increase (Tables 5-6), some values for this change at some of the intermediate cycles were negative. This meant that for some of the in-between cycles, the measured stretch was less than the initial cycle. This was not physically feasible. The likely error in these measurements came from some form of camera defect arising from either the positioning or calibration. The angle measures taken through the load cell were free of such influences and so, produced the physically consistent results, showing a steady increase in angle for steadily progressive cycling.

6.3.1 Equation Regression

The information in this section was referenced from a textbook on the subject of numerical methods[100]. The model for the fatigue life curve was generated by fitting a three-parameter exponential decay equation (Equation 4-33) to the data set for the average fatigue life. The regression to determine the best-fit parameters was performed using the three data points at 100%, 80% and 90% of the respective specimen $\mathbf{M_f}$ magnitude. For a powerful regression, it is desired to have a sufficient number of experimental observations. Gaps in the data that arise from either

an insufficient number of data points or data points that are too dispersed, either randomly or in one direction, can lead to a number of non-ideal circumstances within the model.

However, although only three points were used for the stress-based fatigue life curve, these data points contained information from eleven empirical measurements. This was the basis for assuming sufficient observations for the curve fit. The stretch-based fatigue life curve was explicitly fit to the individual eleven data points.

This data set for the stress-based fatigue life curve has a deficit in the range between each data point of 10%. Regarding the domain of the experimental data, between the ordinate values 100% and 90%, there was a gap of 3211 cycles. Between 90% and 80%, this gap was 21852 cycles. This meant that interpolation was needed to model the behavior of the curve between these points. The built-in function 'fmincon' was used in MATLAB to perform the curve-fit and data interpolation. Using the available options, spline interpolation using a cubic model was chosen as the interpolating algorithm.

Spline interpolation was chosen because it tends to be more accurate than other interpolation methods, as the data at the end points of each interval are constrained to equal the experimental values. A downside of this method was that individual equations are formulated within each interval. This can lead to some erratic model behavior, such as inflection points between experimental observations that follow the data very poorly. This was avoided by selecting interpolating polynomials that were not too high of a degree. The utilized experimental data, i.e. the end behavior of each interval, was well-distributed, which generated smooth splines within each interval.

Because the fatigue life curve was sought to model the fatigue life beyond the tested limit of 80%, extrapolation was needed to model the equation behavior beyond the experimental

domain. The extrapolation of the data followed from the cubic model used in the interpolation step. Because the data was well-dispersed, this allowed the extrapolated curve to follow a smooth trend from the final data point. This, along with the general knowledge of standard fatigue life curve behavior, was the subject of confidence in the extrapolation result.

6.3.2 Fatigue Failure Modes

In the fatigue test, five of the eleven specimens failed at the sublime tubercle of the ulna. This was a greater amount than the three specimens that failed each at the epicondyle and mid-substance. In the experiment, the motion of the humerus was maintained relatively static and the ulna was made to rotate. This motion mimicked the kinematics of the rotating forearm during an overhand pitch. Because the ulna was the location on the ligament furthest away from the axis of rotation, the magnitude of the moment was greatest at this point. This could explain why the majority of the specimens failed due to ulnar avulsion.

The issue of injury/failure location was highlighted by the variability of injury locales in the results and was tested by the work of Frangiamore et al[101]. In a study involving the UCL, cuts were made to the distal and proximal insertions while applying varying degrees of valgus torque. The results showed that the posterior distal insertion contributed more to the rotational stability and stiffness of the medial elbow for all cases. This directly supports the current findings. The majority of the failures occurring at the distal, or ulnar insertion, suggest that the majority of the load was being supported at this location, leading to a higher likelihood of localized failure.

In addition, the experimentally observed tendency of the valgus loaded specimens to fail at the ulnar insertion was also supported by the work of Hassan et al[102]. Different degrees of detachment of the UCL from its distal and proximal ends were imposed while varying degrees of

valgus torque was applied at 90˚ and 30˚ of flexion. Measurements were made regarding the change in contact area and center of pressure which showed the proximal half of the UCL ulnar footprint having the primary role in maintaining elbow biomechanics in the posteromedial elbow. The failure modes of the presently tested specimens, all at 90˚ of flexion, were supported by this work.

The primary cause of the avulsion failures observed in the experiment was assumed to be due to fatigue, although other factors like creep and viscoelastic stress relaxation may have played a role. If these effects were appreciable, the increase in stretch could have altered the ligament failure properties. It is known that the conditions of the experiment play a role in the failure mode exhibited by the ligament. In knee ligaments, it was shown that the strain rate can significantly affect the ligament failure mode[103]. All of the specimens in the current work were cycled at the same frequency of 1 Hz. The previously discussed failure patterns may be different for different cycling frequencies.

Because the ultimate fatigue failure is an amalgamation of smaller micro-traumas arising during the cycling, the presence of pain may serve as an indicator of impending failure. Potential pain caused by these micro-traumas has been evaluated through physical examination of throwing athletes using a variety of tests[104, 105]. The sensitivity of these tests may not be sufficient to identify the exact location of the source of pain, but the general observations of these results and the related work could give high probability to the likelihood of the issue being located near the region of the ulnar insertion.

Other indicators of the onset of fatigue failure can be sound. Athletes with acute UCL tears have been known to hear or feel a “popping” sensation at the time of suspected injury[106]. During the fatigue testing, there were several minute “popping” sounds that could be distinguished

throughout the cycling. These sounds became more pronounced as the specimens reached their failure point. Complete failure was often accompanied by a significant "pop" which was not as sudden, but longer in duration, signifying the continuous tearing of the ligament.

Whether the fatigue failure of the ligament occurs by avulsion at the origin/insertion cites or tearing at the mid-substance, the reconstruction of the fractured ligament can be performed by many different techniques. These may include the docking technique, Jobe technique, Dane Tommy John technique or American Sports Medicine Institute technique[107]. Good outcomes in regard to valgus stability restoration and return-to-play have also been documented[31, 108].

6.4 Finite Element

6.4.1 Elastic Simulation

For the elastic finite element simulation, the post-processing took the average of all the deviatoric stress and strain results for every element in the ligament. The average was taken because it was desired to run a large number of simulations and, while taking the results from a specified region of the ligament was possible, selection of the same elements for analysis after each simulation was impractical. It was also desired to gain a complete representation of the whole-ligament response, which could be better achieved by analyzing all of the elements.

Selection of every element had its disadvantages. The first disadvantage was that the inclusion of every element meant that those elements at the boundary, either in direct contact with the bone or in the near vicinity, were included in the results. This could have introduced some irregularities in the average results. In accordance with St. Vennant's Principle[109], the behavior

of the material farther away from the boundary more closely represents the actual material behavior. To mesh the material at the boundaries, some elements may have been stretched or compressed, leading to high aspect ratios. Because of this, these elements too close to the boundary could have displayed stress and strain responses that were far removed from the physiological range.

This was noticeable when analyzing the individual responses of the elements. Some elements displayed maximum stresses on the order of 10^8 and strains greater than 100 percent. Both of these values were non-physiological. To account for this, it was assumed that the number of elements near the mid-substance of the ligament, away from the ulna and humerus insertion sites, was much greater than the number of elements at the boundary. This assumption was based on the quantitative measurements taken of the ligament length, which has the greater proportion away from the boney insertions. Therefore, given their quantity, the mechanical responses of the mid-substance elements would out-weigh the influences from the boundary and contribute more to the average stress-strain response.

Another disadvantage of taking the average of the results for every element was the loss of non-linearity. As seen from the results of Figures (82-86), every average response was linear. However, when analyzing the individual responses, the non-linear stress-strain behavior typical of ligaments was present in a majority of the elements. When considering that there were thousands of elements involved in the simulation, it was likely that the total response of the ligament could become linearized within the average calculation. This is because amongst the individual element responses, some were entirely linear. This was not unexpected because some of the specimens in the experimental elastic testing displayed similar behavior. If the magnitude of the stress in these elements was significantly greater than the magnitude of stress in those elements with non-linear

responses, then the average response of all the elements would be dominated by the linear behavior.

As seen in Figures (82-86), for several specimens, the average response correlated well with the modeled behavior of the ligament. For other specimens, the average response did not correlate very well, but the addition of one standard deviation did. Analyzing the response with the inclusion of one standard deviation was done because it is commonplace to include the standard deviation with average measurements.

For every specimen, the constitutive modeled behavior was always within one standard deviation of the average simulated FE behavior. When the results did not closely agree, the average FE results were typically less than the constitutive modeled behavior. This may have been a result of the small degree of displacement that was imposed in the FE model. Excluding the rigid body motion of the elements near the displacing ulna, the relative motion between the elements along the length of the ligament may not have been great enough to produce large stress-stretch responses. Averaging all of these minute responses together would undoubtedly produce an average response that was less than the constitutive modeled response.

6.4.2 Fatigue Simulation

For the fatigue simulation, the simulated displacement of 2-3 mm was consistent with the measured joint opening of the cadaveric specimens during testing, and was within the range of ultrasonically measured values of 3 – 5 mm for current athletes undergoing valgus loading protocols[98].

The direction of ulnar displacement was set to be vertical with respect to the humerus. The olecranon constrains the ulna from separating too far out of the same plane as the distal humerus.

Given the results of Pexa et al[98], it was seen that no such constructs prevent the joint from opening in a plane perpendicular to the ulna, as observed in valgus rotation. The tetrahedral elements used in the simulation do have rotational degrees of freedom however, the asymmetric geometry of the ulna made the boundary conditions necessary for rotational displacement difficult to define. The experimental findings, small angle theory and limitations of the simulation lead to the utilized vertical elongation method.

For a single cycle of displacement, the average maximum stretch of all the elements was observed to be approximately 99.7 percent of the experimentally observed average failure stretch. The result of the one cycle average stretch being close in magnitude to the average fatigue failure stretch for an approximately equivalent level of loading could be explained numerically and physically. Physically, the AMCL is the primary inhibitor of elbow valgus rotation[19], therefore, the amount of stretch to prevent rotation should be relatively close to the stretch at failure, given the tendency of the ligament to resist excessive stretching to stabilize the elbow. Numerically, any number of misshapen elements or elements to close to the boundary could contribute to an enlarged stretch result.

The maximum stretch was used instead of the maximum stress to form the ratio by which to estimate the cycles to failure, because while the displacements for a small degree of valgus rotation and vertical elongation may be similar, the stresses may be different. Because stress is a second order tensor, the 3D loading of a body can greatly affect the magnitudes of the components. The orientation of the body with respect to a given coordinate system can also have a significant effect on the components, as transformations may need to be considered. In contrast, the strain/stretch tensor, when considering the principal values, can be represented as a vector whose

components are independent of the orientation of the body or the loading. This is because these principal values occur in planes where shear influences are negligible[109].

Only three of the eleven tested specimens produced cycles to failure values that were of the same magnitude of the experimental values. For most cases, the experimental values were much higher. This could be a consequence of the lack of individual specimen geometry present in the model. The same 3D model was utilized for the simulation of each specimen. As mentioned before, each specimen was unique in their width, thickness and length measures. Having these variables more closely related to the actual physical attributes may have produced closer cycles to failure estimates.

6.4.2.1 Iterative Manual Application of Damage

This method of simulating fatigue differs from the standard finite element method. In the standard method, the 3D model would be cycled automatically given the conditions of the simulation. After every unloading, the constitutive equation parameters would be altered individually for each element. This would then alter their elemental stiffness matrices and, likewise, the global stiffness matrix. The average stress-strain response of the AMCL would then be output.

The current method adjusted the constitutive equation and consequently, the stiffness matrices, of every element on a global scale. This method can be justified through assumptions made about how the ligament accrues damage and where the damage may occur. This method considered the ligament as one body and for the first cycle, the maximum stress/stretch represented an equivalent stress/stretch that would be experienced at every level of the body. This was akin to the stress/stretch that would be measured in a standard tensile test of a rectangular tissue specimen.

This singular maximum stress/stretch then presented a single estimate of the cycles to failure for the whole ligament and, thus, every element.

This cycles to failure value governed the nature of the subsequent cycling, for which each element was assumed to accrue, nonlinearly, the same amount of damage per cycle. Therefore, each element had a different stress-strain response, but each element's response was changing at the same nonlinear rate and would ultimately reduce to a failure state at the same number of cycles. This was a holistic approach to characterizing the damage accumulation of the AMCL, rather than a localized one.

While a localized method may be useful for predicting where failure may occur for the AMCL, it may not be as necessary when predicting when failure might occur. As mentioned earlier, every cycle produces a wide variety of stress-stretch responses for each element. Elements with very high stress responses would be predicted to fail at a low cycle number. Conversely, elements with low stress responses would fail at a high cycle number. Both of these results would provide an insufficient prediction for the cycles to failure causing the ligament to approach localized failure either too quickly or too slowly. Having the holistic approach, where the average of these responses was considered, could have possibly brought the cycles to failure prediction into a more anatomically accurate range.

6.4.2.2 Elemental Stress and Strain Distribution Contours

The contour options in post processing gave a visualization of the respective stress and strain distributions. Figures (92-93) show these distributions for specimen 10 for the cyclic cases of n/n_f equal to 0, 0.5 and 0.95. For both stress and strain, the more focused regions indicating the greater magnitudes of stress and strain were located at the mid-substance of the ligament. These results were expected because the elements near the humerus are near the static body and therefore,

displace less and should show lesser magnitudes of the kinetic variables. The elements closer to the mid-substance would have more relative displacement, as compared to the rigid body motion of the elements near the ulna, producing a more distinguishable stress/strain distribution.

The contours of strain did not change by a noticeable degree for each of the cyclic cases. This meant that the distributive effect seen in the strain behavior remained relatively constant throughout the simulated cycling. This could be indicative of stretch magnitudes that do not change much with the altering of the constitutive parameters, i.e. softening of the ligament. This was indicative of the nonlinear relationship between stress and stretch, where the changes in these two variables in response to some perturbation can be non-proportional.

The contours of stress changed by a moderately distinguishable amount for each of the representative cases (Figures 92-93). As the value of n/n_f increased, the distribution of stress concentration became more broadened around the mid-substance of the ligament. This suggested that the magnitude of the stresses near this portion changed significantly as the cycling progressed. This was expected because altering the constitutive parameters directly affected the stress response of the elements. The highest stresses being located near the mid-substance is difficult to analyze because the results discussed in section 6.3.2 would suggest that the regions of greatest concentration should be near the ulna, but these elements were near the boundary, so some of the ulnar element behaviors may be irregular.

6.4.2.3 Stress Softening

The simulated decrease in stress and increase in stretch was evaluated at n/n_f values of 0.25, 0.5, 075 and 0.95. These specific evaluation points were chosen for ease of comparison with the experimental results. The stress was observed to decrease nonlinearly across the simulated cases. The stretch was observed to increase nonlinearly from the first to last cycles.

The profile of the nonlinear stress softening nearly resembled that of the damage evolution curve of Figure (35) and had very little variation according to the average results seen in Figure (96). This was expected because the fraction by which the stress decreased was governed by the manual altering of the constitutive model parameters. The relative matching of the two curves justified the method of altering the parameters of C_1-C_3 only, excluding C_4, showing that the straightening of the fibers represents a physical property that remains unaffected by the stress softening from fatigue loading.

6.4.2.4 Stretch Increase

It was expected for the maximum stretch of the ligament to increase with increasing values of n/n_f. The magnitude of this increase was evaluated for the same values of n/n_f as the analysis for the stress decrease. As seen in Figure (98), the rate of this increase for the simulation was nearly linear and constant up to a value of n/n_f of 0.75. Up to a value of n/n_f of 0.95, the curve then exhibits a sharp increase in slope up to the maximum value of stretch increase.

The constant slope of the linear region could be indicative of the minute, yet steady, formation of micro-trauma failure mechanisms, such as individual fiber deformations. This small degree of fiber deformation at low cycle fatigue levels has been observed ultrasonically in animal tendons subjected to repetitive cycling[110]. It could be at this point during a pitching cycle that small indicators of these fiber deformations can arise on the macro-level, such as discomfort in the throwing elbow. The degree of these deformations was observed to grow in magnitude as the cycling progressed until the tendon reached a state of significant matrix disruption at the higher cyclic levels[110]. This severe matrix distortion would undoubtedly result in high rates of stretch increase, which could be indicative of the sharp increase in slope seen in the results for fatigue induced stretch increase.

The breaking of the fibers during this initial region may present an opportunity for healing of the ligament to occur. These small defects in the ligament where the fiber tearing might have occurred would be healed by the typical ligament/tendon healing pathway. This pathway includes cell proliferation, fibrous tissue reformation and collagen fiber realignment[111] and collagen fibril diameter growth[112].

The accelerated slope near the latter end of the curve could represent a region during the cycling where irreparable damage has occurred and failure is likely imminent. However, it is necessary to highlight that the data in these results was taken at every approximate 25th percent of the total cycle life for each specimen. If the data were sampled at a finer rate, then the dramatic rise in slope displayed between 75% and 95% cycle completion may not be as pronounced.

6.4.3 Model Validation

The validation of an FE model is predicated on the ability of the model to predict the outcome of experimental observation. The experimental observation chosen for proof of validation was the increase in maximum stretch recorded after specified cycle completion. The average experimental increase in stretch for the eleven specimens was approximately 0.63% and 0.91% for 50% and nearly 100% of their respective cycles to failure value. The simulated stretch increase values agreed well with the experimental values, giving percent difference magnitudes of less than 1% for each case, as seen in Table (10).

The variable of stretch increase was used to validate the model because it was a dependent variable of the displacement-controlled simulation. The damage evolution curve of Figure (35) was derived using the experimental data for the increase in rotation angle for the specimens subjected to cyclic valgus loading. Rotational angle and ligament stretch are understandably

correlated, as larger rotation angles will produce larger stretch values. However, this relationship, given the nonlinear behavior of the ligament, is not one-to-one. Therefore, the information contained in the damage evolution curve and imparted into the model has no inclusion of information regarding fatigue induced ligament stretch effects. Thus, the increase in the maximum stretch was a uniquely predicted variable and was not influenced by the mechanical properties input into the elastic model, or the modified cycling model, rendering it a suitable variable for validation analysis.

Another variable for validation would be the stress-stretch behavior. With this consideration, the stress-stretch behavior of the specimen would be analyzed at some experimental cyclic step and compared to the stress-stretch behavior of the simulation at the same number of cycles. In the absence of a method to relate ulnar torque to ligament force, or to measure ligament force directly, this method of validation was not feasible for the current work.

6.4.4 Elemental (Localized) Stress Softening

The localized stress softening method was used to visualize where along the AMCL failure was likely to occur. It was not a finite element routine. The elements were treated as isolated entities with their own stress-strain responses, damage evolution rate and cycles to failure value. In a finite element routine, these variables would also be unique to each element, but there would also be individual alterations to the elemental and global stiffness matrices, making the stretch-stress responses inherently different after each cycle. However, the damage evolution rate and the cycles to failure for each respective element, as dictated by the results of the first cycle, would be unaltered in the finite element routine.

Because these two variables, the damage evolution rate and elemental cycles to failure, were independent of the finite element method, the effect of these variables on the initial stress-stretch behavior of the ligament was also independent. Therefore, a visualization of how the stress and strain distribution was changing during cycling was not plausible in the absence of the finite element resources, but a visualization of how quickly the stress would soften was plausible. In the interest of predicting fatigue failure location, this was more valuable.

The results showed the regions with the quickest stress deterioration were at the mid-substance and at the ulnar insertion. These results match with the findings of the fatigue experiment where the most failures occurred at the ulna and the mid-substance, respectively. However, it is again mentioned that because the elements near the ulna were located at the boundary, these results warrant further attention. These results are also supported by previously reported works. In a study involving 353 patients, MRI was used to classify acute ACL tears based on location. Of those patients tested, approximately 43% of the tears occurred at the proximal ligament and 52% at the mid-substance[113]. In adolescent pitchers, these numbers were approximately 38% and 52%[114].

This observation of proximal vs distal ligament tearing is critical when concerning the UCL of baseball pitchers. In a study involving 25 pitchers who underwent UCL reconstruction (UCLR), 60% had proximal tears and had lesser return to sport (RTS) rates and lower postoperative utilization than athletes with distal tears[115]. These findings show how critical it is to know who may be susceptible to a fatigue injury and where, because it can significantly affect the career of the athlete. The visualization results of Figure (100), could provide a rough estimate of this valuable information.

The progression of the stress softening as the cycles were increased was evident across Figures (101-104). As the number of cycles grew, the number of elements within the designated problem ranges increased and those elements previously within the problem range progressively moved toward more hazardous ranges. This shows how the visualization model can track the progression of stress softening at different locations along the ligament.

A disadvantage of this technique was how the cyclic ratio for each element was calculated. It was a ratio of the maximum average elemental stretch to the maximum average experimental fatigue failure stretch. If this ratio was greater than one, then the natural log in the cycles to failure equation (Equation 5-2) would have produced a negative number for the predicted cycles to failure value, which is not feasible. This was inevitable, due to the nature of finite elements, that some elements would produce maximum stretch values that exceed the experimental value. Elements exhibiting this result had to be excluded from the visualization.

Another disadvantage was that the rate of stress softening could be faster in the finite element method. The softening of surrounding elements could have an effect on the nearest neighbors, causing softening to occur at an accelerated rate in the adjacent vicinities. This would affect the visualization and the overall results.

6.4.5 Alternative Influencing Factors

6.4.5.1 Stress Relaxation

Stress relaxation could have played a role in the final results, based on the nature of the fatigue experiment. After each step of 500 cycles, the apparatus was stopped for a period of time to allow for the re-initiation of the next 500 cycles and video recording. Depending on the total

cycles achieved, this brief window of inaction occurred multiple times during the testing of each specimen and could have provided the opportunity for stress relaxation to occur.

The rate of stress relaxation in ligaments is dependent on the magnitude of strain[67]. Because each specimen was loaded to a different magnitude of valgus torque, the strain magnitude was different for each specimen. This meant that any relaxation experienced would occur at a different rate for each specimen. Those tested at lesser loads would relax faster than those tested at higher loads, as the rate of stress relaxation in ligaments has been shown to decrease with increasing strain magnitude[116].

If the influence of stress relaxation were significant, the varying degree of relaxation rates between the specimens could have affected the results. Specimens loaded to lesser strains would have relaxed faster, possibly allowing the ligament to recover and increase the ultimate fatigue life of the ligament. Ligaments loaded to larger strains would not have been afforded this mechanical advantage.

This advantage for the lower strained specimens could have been mitigated by the time allowed for relaxation. It has been shown that the effects of time allotted and strain magnitude influence the relaxation phenomenon independently of each other, with relative relaxation rates being equivalent for similar times and varying strains[117]. This means that if the time spent in these periods of inactivity were relatively equivalent for each specimen, each specimen would experience a similar rate of relative relaxation regardless of the strain magnitude. With this in mind, the time of each dead period was dependent on the consistency of the operator and was not consciously controlled for each specimen. However, the relative speed was fairly consistent.

6.4.5.2 Temperature

Three of the fatigue tests could not be concluded in one day. Those specimens had to be stored in a cooling unit for testing to resume the following day. There was one specimen which had to be completely refrozen. It has been shown that the refreezing and thawing of fibrous tissues, such as ligaments[118] and tendons[119], does little to affect the mechanical, viscoelastic or damage properties of the material. This is true assuming the tissue has been thawed to room temperature. Given the time scale of the current work, the single refrozen specimen and the three re-cooled specimens were not able to equilibrate to room temperature before testing resumed.

It is known that temperature changes within a body can affect the mechanical properties. In dynamic frequency testing of brain tissue, it was shown that decreasing temperatures resulted in stiffer material responses[120]. Assuming that the cooled specimens experienced an increase in stiffness, this would significantly affect the results for their fatigue life. The fatigue failure characterized by decreasing stiffness could have been counteracted by the increase in stiffness experienced from the lowered temperature.

This was addressed during the test, as observation of the colder tissue did reveal a tougher texture and seemingly less flexibility. After a few hundred cycles, the heat generated from the motion eventually returned the specimens to room temperature. Because this was only experienced for four of the eleven specimens, it was assumed that the overall fatigue life results remained adequately representative.

7.0 Conclusion

This work was the first to define the nonlinear damage accumulation behavior of the AMCL resulting from repetitive valgus loading and provide a basis for implementation of the nondimensional results into a finite element routine. An empirical result by which to estimate the fatigue life of the AMCL based on the maximum stretch/stretch was also presented. When combined, these two contributions provide a method by which to estimate the nonlinear stress-softening of the AMCL resulting from an arbitrary number of valgus repetitions, relevant to baseball pitching.

This work was performed in the interest of providing a contribution to the understanding of the mechanical and damage accumulation properties of the AMCL. Having a reliable model phenomenologically derived from the behavior of twenty-two specimens can be a valued asset in the effort to manage and improve the elbow health of the overhand throwing athlete.

Regarding baseball pitchers, if estimates can be made about the stretch experienced by the AMCL during a certain type of pitch, then the fatigue life of the AMCL can be estimated using the fatigue life curve provided by this work. That curve would inform the athlete and trainers about how many approximate pitches of that type can be performed before failure. This could help the relevant decision makers devise routines that alternate and optimize periods of performance and rest.

At the conclusion of performance periods, the amount of pitches thrown can be used to estimate the accrued amount of damage using the nonlinear damage evolution curve provided by this work. This could inform physicians about what degree of additional stretching and stress softening has occurred. Having this information could inform decisions on how long to rest the

athlete to enable an adequate amount of healing. If any assistive rehabilitation is necessary, knowledge of the degree of estimated damage could guide decisions on utilized methods and techniques.

In the presence of elbow pain, knowing the amount of damage could help clinicians make estimates as to whether significant tearing has occurred. Knowing this before having the confirmation of MRI could help in the immediate stabilization of the elbow prior to imaging and subsequent intervention.

Having an additional method for the purpose of monitoring and predicting the fatigue health of the AMCL in the throwing athlete can provide an improvement in the confidence of performance, reliability in investment and assuredness of availability.

7.1 Limitations

To measure the deformation of the ligament during the elastic testing, the tracking of optical markers was used to make measures of strain. The reliability of this method depended on the positioning of the markers. Markers too close together could register as a single marker and markers too far apart could fail to capture the curvilinear nature of the ligament. This could have resulted in some inaccuracies in the strain measurements, which would affect the stress-stretch behavior and the resulting model. Full-field strain measurement techniques, such as digital image correlation (DIC) may be more suitable.

It was desired to have the humerus completely stationary during the valgus cycling of the fatigue tests. This was never exactly accomplished, as the swing arm housing the humerus did experience some slight motion for each specimen. The cause of this could have been the

inadequate properties of the shaft which allowed for bending to take place. Slight movement of the humerus allowed for increased relative motion between the ulna and humerus, resulting in strain measurements that would be inherently different from those measured from an ideally stationary humerus. Because the motion of the humerus was relatively small in comparison to that of the ulna, the magnitude of this effect on the resulting strains was assumed negligible. This was a design issue that will be corrected for future works.

The fatigue properties were unable to be explicitly implemented into a finite element routine. This limited the ability of the work to analyze the local stress and strain states at different locations along the ligament. It necessitated that a simpler, more general formulation be used which was sufficient for the purposes of the current work, but may lack the sophistication needed for more advanced efforts. With the resources available to acquire the necessary software, this limitation could be readily overcome.

7.2 Future Work

Completely implementing the fatigue effects defined by the work into a fully automated finite element routine would be the primary continuation. Once this has been achieved, complete simulations can be ran without the need for manual augmentation and full analyses on the local stress and strain effects can be performed.

The hope is for this work to someday benefit the performance and health of the baseball pitcher. For this to happen, the utility of the work needs to be extended for the consideration of active pitchers. Non-invasive methods such as ultrasound assisted shear wave elastography could be used to estimate the stress-stretch behavior of the throwing athlete for a variety of pitch types

and pitch speeds. This data could then be used in conjunction with the fatigue life curve, damage evolution curve and finite element simulation to make accurate predictions on the relevant ligament health implications for the athlete, resulting from any number of prospective performance levels.

The 3D models, for purposes of increasing predictive accuracy, would need to be better suited to fit the native biology of the individual athlete. Because every AMCL can vary in width, thickness and length, a method to accurately adjust these variables based on the measurements of the current subject would be critical in increasing model reliability. This could be accomplished by taking an MRI of the athlete's elbow and generating a unique solid model specifically for that athlete. In cases where that may not be possible, the current model can be augmented as guided by certain anthropometric variables, such as body mass index (BMI), height or bone structure that may correlate with ligament geometry, as has been shown to be true for the diameter[121] and length[122] of hamstring grafts used in ACL reconstruction.

To increase the utility of the model, the ability to simulate the fatigue implications resulting from different pitch types could be potentially added. Because the model simulates valgus motion through vertical joint opening, different pitches would need to be categorized by their respective joint opening magnitudes. This could be measured ultrasonically on a population of pitchers performing different pitching actions. In addition, because different amounts of these pitches are thrown per game, the utility of the model would need to be extended for the purpose of simulating an arbitrary number of mixed pitch types.

The current model consists only of the ulna, humerus and AMCL. It does not consider the effect of the surrounding muscle complexes. The muscles at the elbow and forearm support valgus motion and therefore, relieve some of the stress on the AMCL. This relief in stress would

intuitively increase the fatigue life of the ligament. Improving the accuracy of the model for future work would include introducing additional model parameters that could effectively simulate the presence of the surrounding muscle.

Bibliography

1. K, Kadler, *Fell Muir Lecture: Collagen Fibril Formation in Vitro and in Vivo.* Int J Exp Path, 2017. **98**(1): p. 4-16.

2. M, Buehler, *Nature Designs Tough Collagen: Explaining the Nanostructure of Collagen Fibrils.* Proc Natl Acad Sci USA, 2006. **103**(33): p. 12285-12290.

3. J, Halper, *Progress in Heritable Soft Connective Tissue Diseases*. 2014: Springer.

4. Szczesny S, Fetchko K, Dodge G, Elliott D, *Evidence That InterFibrillar Load Transfer in Tendon is Supported by Small Diameter Fibrils and Not Extrafibrillar Tissue Components.* J Orthop Res, 2017. **35**(10): p. 2127-2134.

5. Henninger H, Valdez W, Scott S, Weiss J, *Elastin Governs the Mechanical Response of Medial Collateral Ligament Under Shear and Transverse Tensile Loading.* Acta Biomater, 2015. **25**: p. 304-312.

6. Shen Z, Dodge M, Kahn H, Ballarini R, Eppell S, *Stress-Strain Experiments on Individual Collagen Fibrils.* Biophysical Journal, 2008. **95**: p. 3956-3963.

7. Fleisig G, Escamilla R, *Kinetics of Baseball Pitching with Implications About Injury Mechanisms.* Am J Sports Med, 1995. **23**(2): p. 233-239.

8. Weber A, Kontaxis A, O'Brien S, Bedi A, *The Biomechanics of Throwing: Simplified and Cognet.* Sports Med Arthrosc Rev, 2014. **22**(2): p. 72-79.

9. Sisto D, Jobe F, Moynes D, Antonelli D, *An Electromyographic Analysis of the Elbow in Pitching.* Am J Sports Med, 1987. **15**(3): p. 260-263.

10. Werner S, Fleisig G, Dilman C, Andrews J, *Biomechanics of the Elbow during Baseball Pitching.* J Orthop Sports Phys Ther, 1993. **17**(6): p. 274-278.

11. Feltner M, Dapena J, *Dynamics of the Shoulder and Elbow Joints of the Throwing Arm During a Baseball Pitch.* Int J Sports Biomech, 1986. **2**: p. 235-259.

12. Urbin M, Fleisig G, Abebe A, Andrews J, *Associations Between Timing in the Baseball Pitch and Shoulder Kinetics, Elbow Kinetics, and Ball Speed.* Am J Sports Med, 2012. **41**(2): p. 336-342.

13. Pappas A, Zawacki R, Sullivan T, *Biomechanics of Baseball Pitching.* Am J Sports Med, 1985. **13**(4): p. 216-222.

14. Fehr S, Damrow D, Kilian C, Lyon R, Liu X, *Elbow Biomechanics of Pitching: Does Age or Experience Make a Difference?* Sports Health, 2016. **8**(5): p. 444-450.

15. David J, Limpisvasti O, Fluhme D, Mohr K, Yocum L, Elattrache N, Jobe F, *The Effect of Pitching Biomechanics on the Upper Extremity in Youth and Adolescent Baseball Pitchers.* Am J Sports Med, 2009. **37**(8): p. 1484-1491.

16. Okoroha K, Lizzio V, Meta F, Ahmad C, Moutzouros V, Makhni E, *Predictors of Elbow Torque Among Youth and Adolescent Baseball Pitchers.* Am J Sports Med, 2018. **46**(9): p. 2148-2153.

17. Naito K, Takagi T, Kubota H, Maruyama T, *The Effect of Multiple Segment Interaction Dynamics on Elbow Valgus Load during Baseball Pitching.* J Sports Eng Tech, 2017. **232**(4): p. 285-294.

18. Hattori H, Akasaka K, Otsudo T, Hall T, Amemiya K, Mori Y, *The Effect of Repetitive Baseball Pitching on Medial Elbow Joint Space Gapping Associated with 2 Elbow Valgus Stressors in High School Baseball Players.* J Shoulder Elbow Surg, 2018. **27**(4): p. 592-598.

19. Eygendaal D, Olsen B, Jensen S, Seki A, Sojbjerg J, *Kinematics of Partial and Total Ruptures of the Medial Collateral Ligament of the Elbow.* J Shoulder Elbow Surg, 1999. **8**(6): p. 612-616.

20. Lyman S, Fleisig G, Waterbror J, Funkhouser E, Pulley L, Andrews J, Osinski D, Roseman J, *Longitudinal Study of Elbow and Shoulder Pain in Youth Baseball Pitchers.* Med Sci Sports Exerc, 2001. **33**(11): p. 1803-1810.

21. Fleisig G, Andrews J, *Prevention of Elbow Injuries in Youth Baseball Pitchers.* Sports Health, 2012. **4**(5): p. 419-424.

22. Wright R, Steger-May K, Klein S, *Radiographic Findings in the Shoulder and Elbow of Major League Baseball Pitchers.* Am J Sports Med, 2007. **35**(11): p. 1839-1843.

23. Camp C, Dines J, Voleti P, James E, Altchek D, *Ulnar Collateral Ligament Reconstruction of the Elbow: The Docking Technique.* Arthrosc Tech, 2016. **5**(3): p. 519-523.

24. Donohue B, Lubitz M, Krernchek T, *Elbow Ulnar Collateral Ligament Reconstruction Using the Novel Docking Plus Technique in 324 Athletes.* Sports Med Open, 2019. **5**(3): p. 1-9.

25. Bodendorfer B, Looney A, Lipkin S, Nolton E, Li J, Najarian R, Chang E, *Biomechanical Comparison of Ulnar Collateral Ligament Reconstruction with the Docking Technique versus Repair with Internal Bracing.* Am J Sports Med, 2018. **46**(14): p. 3495-3501.

26. Dugas J, Walters B, Beason D, Fleisig G, Chronister J, *Biomechanical Comparison of Ulnar Collateral Ligament Repair with Internal Bracing versus Modified Jobe Reconstruction.* Am J Sports Med, 2012. **44**(3): p. 735-741.

27. Hurwit D, Garcia G, Liu J, Altchek D, Romeo A, Dines J, *Management of Ulnar Collateral Ligament Injury in Throwing Athletes: A Survey of the American Shoulder and Elbow Surgeons.* J Shoulder Elbow Surg, 2017. **26**(11): p. 2023-2028.

28. Jones C, Beason D, Dugas J, *Comparison of Cyclic Fatigue Mechanics Between UCL Repari with Internal Bracing and UCL Reconstruction.* Orthorp J Sports Med, 2017. **6**(2).

29. Erickson B, Bach B, Verma N, Bush-Josheph C, Romeo A, *Treatment of Ulnar Collateral Ligament Tears of the Elbow. Is Repari a Viable Option?* Orthorp J Sports Med, 2017. **5**(1): p. 1-6.

30. Marshall N, Keller R, Limpisvasti O, Schulz B, ElAttrache N, *Major League Baseball Pitching Performance After Tommy John Surgery and the Effect of Tear Characteristics, Technique, and Graft Type.* Am J Sports Med, 2019. **47**(3): p. 713-720.

31. Cain E, Andrews J, Dugas J, Wilk K, McMichael C, Walter J, Riley R, Arthur S, *Outcome of Ulnar Collateral Ligament Reconstruction of the Elbow in 1281 Athletes.* Am J Sports Med, 2010. **38**(12): p. 2426-2434.

32. Saper M, Shung J, Pearce S, Bompadre V, Andrews J, *Outcomes and Return to Sport After Ulnar Collateral Ligament Reconstruction in Adolescent Baseball Players.* Orthorp J Sports Med, 2018. **6**(4): p. 1-7.

33. Erickson B, Gupta A, Harris J, Bush-Josheh C, Bach B, Abrams G, San Juan A, Cole B, Romeo A, *Rate of Return to Pitching and Performance after Tommy John Surgery in Major League Baseball Pitchers.* Am J Sports Med, 2013. **42**(3): p. 536-543.

34. Marshall N, Keller R, Limpisvasti O, ElAttrache N, *Pitching Performance After Ulnar Collateral Ligament Reconstruction at a Single Institution in Major League Baseball Pitchers.* Am J Sports Med, 2018. **46**(13): p. 3245-3253.

35. Wojtys E, Beaulieu M, Ashton-Miller J, *New Perspectives on ACL Injury: On the Role of Repetitive Sub-Maximal Knee Loading in Causing ACL Fatigue Failure.* J Orthop Res, 2016. **34**(12): p. 2059-2068.

36. Lynn S, Noffal G, *Frontal Plane Knee Moments in Golf: Effect of Target Side Foot Position at Address.* J Sports Sci Med, 2010. **9**(2): p. 275-281.

37. Purevsuren T, Kwon M, Park W, Kim K, *Fatigue Injury Risk in Anterior Cruciate Ligament of Target Side Knee During Golf Swing.* J Biomech, 2017. **53**: p. 9-14.

38. Lipps D, Wojtys E, Ashton-Miller J, *Anterior Cruciate Ligament Fatigue Failures in Knees Subjected to Repeated Simulated Pivot Landings.* Am J Sports Med, 2013. **41**(5): p. 1058-1066.

39. Flick J, Devkota A, Tsuzaki M, Almekinders L, Weinhold P, *Cyclic Loading Alters Biomechanical Properties and Secretion of PGE2 and NO from Tendo Explants.* Clin Biomech, 2006. **21**(1): p. 99-106.

40. Leena N, King K, Abrahamsson S, Rempel D, *Evidence of Tendon Microtears due to Cyclical Loading in an in vivo Tendinopathy Model.* J Orthop Res, 2005. **23**(5): p. 1199-1205.

41. Leena N, King K, Abrahamsson S, Rempel D, *Effect of Repetition Rate on the Formation of Microtears in Tendon in an In Vivo Cyclical Loading Model.* J Orthop Res, 2007. **25(**9): p. 1176-1184.

42. Egger A, Berkowitz M, *Achilles Tendon Injuries.* Curr Rev Musculoskelet Med, 2017. **10**(1): p. 72-80.

43. Wren T, Lindsey D, Beaupre G, Carter D, *Effects of Creep and Cyclic Loading on the Mechanical Properties and Failure of Human Achilles Tendons.* Ann Biomed Eng, 2003. **31**(6): p. 710-717.

44. Chagnon G, Rebouah M, Favier D, *Hyperelastic Energy Densities for Soft Biological Tissues: A Review.* J Elast, 2015. **120(**2): p. 129-160.

45. G, Holzapfel, *Nonlinear Solid Mechanics*. 2000: Wiley.

46. R, Ogden, *Non-Linear Elastic Deformations*. 1997: Dover Publications.

47. M, Sacks, *Biaxial Mechanical Evaluation of Planar Biological Materials.* J Elast, 2000. **61**: p. 199-246.

48. Smith G, Rivlin R, *The Strain-Energy Function for Anisotropic Elastic Materials.* Trans Am Math Soc, 1956. **88**(1): p. 175-193.

49. Wulandana R, Robertson A, *An Inelastic Multi-Mechanism Constitutive Equation for Cerebral Arterial Tissue.* Biomech Model Mechanobiol, 2005. **4**(4): p. 235-248.

50. Canham P, Finlay H, Dixon J, Boughner D, Chen A, *Meaurements from Light and Polarized Light Microscopy of Human Coronary Arteries Fixed at Distending Pressure.* Cardiovasc Res, 1989. **23**(11): p. 973-982.

51. Schriefl A, Reinisch A, Sankaran S, Pierce D, Holzapfel G, *Quantitative Assessment of Collagen Fibre Orientations from Two-Dimensional Images of Soft Biological Tissues.* J R Soc Interface, 2012. **9**: p. 3081-3093.

52. Holzapfel G, Ogden R, Sherifova S, *On Fibre Dispersion Modelling of Soft Biological Tissues: A Review.* Proc R Soc, 2019. **475**: p. 1-22.

53. Holzapfel G, Niestrawska J, Ogden R, Reinisch A, Schriefl A, *Modelling Non-Symmetric Collagen Fibre Dispersion in Arterial Walls.* J R Soc Interface, 2015. **12**: p. 1-14.

54. Luenberger D, Ye Y, *Linear and Nonlinear Programming*. 4 ed. 2015: Springer.

55. Li, Wenguang, *Damage Models for Soft Tissues: A Survey.* J Med Biol Eng, 2016. **36**(3): p. 285-307.

56. Ogden R, Roxburgh D, *A Pseudo-Elastic Model for the Mullins Effect in Filled Rubber.* Proc Royal Soc Lond, 1999. **455**(1988): p. 2861-2877.

57. Dorfmann A, Pancheri F, *A Constitutive Model for the Mulllins Effect with Changes in Material Symmetery.* INT J NONLIN MECH, 2012. **47**(8): p. 874-887.

58. Dorfmann A, Ogden R, *A Constitutive Model for the Mullins Effect with Permanent Set in Particle-Reinforced Rubber.* Int J Solids Struct, 2004. **41**(13): p. 1855-1878.

59. Calvo B, Pena M, Doblare M, *An Uncoupled Directional Damage Model for Fibred Biological Soft Tissues. Formulation and Computational Aspects.* INT J NUMER METH ENG, 2006. **69**(10): p. 2036-2057.

60. Balzani D, Brinkhues S, Holzapfel G, *Constitutive Framework for the Modeling of Damage in Collagenous Soft Tissues with Application to Arterial Walls.* Comput Methods Appl Mech Eng, 2012. **213-216**: p. 139-151.

61. Weisbecker H, Pierce D, Regitnig P, Holzapfel G, *Layer-Specific Damage Experiments and Modeling of Human Thoracic and Abdominal Aortas with Non-Atherosclerotic Intimal Thickening.* J Mech Behav Biomed Mater, 2012. **12**: p. 93-106.

62. J, Simo, *On a Fully Three-Dimensional Finite-Strain Viscoelastic Damage Model: Formulation And Computational Aspects.* Comput Methods Appl Mech Eng, 1987. **60**(2): p. 153-173.

63. Natali A, Pavan P, Carniel E, Lucisano M, Taglialavoro G, *Anisotropic Elasto-Damage Constitutive Model for the Biomechanical Analysis of Tendons.* Med Eng Phys, 2005. **27**(3): p. 209-214.

64. Martin C, Sun W, *Modeling of Long-Term Fatigue Damage of Soft Tissue with Stress Softening and Permanent Set Effects.* Biomech Model Mechanobiol, 2013. **12**(4): p. 645-655.

65. Martin C, Sun W, *Comparison of Transcatheter Aortic Valve and Surgical Bioprosthetic Valve Durability: A Fatigue Simulation Study.* J Biomech, 2015. **48**(12): p. 3026-3034.

66. De Vita R, Slaughter W, *A Constitutive Law for the Failure Behavior of Medial Collateral Ligaments.* Biomechan Model Mechanobiol, 2007. **6**(3): p. 189-197.

67. Provenzano P, Lakes R, Keenan T, Vanderby R, *Nonlinear Ligament Viscoelasticity.* Ann Biomed Eng, 2001. **29**(10): p. 908-914.

68. Hingorani R, Provenzano P, Lakes R, *Nonlinear Viscoelasticity in Rabbit Medial Collateral Ligament.* Ann Biomed Eng, 2004. **32**(2): p. 306-312.

69. Castile R, Skelley N, Babaei B, Brophy R, Lake S, *Microstructural Properties and Mechanics Vary Between Bundles of the Human Anterior Cruciate Ligament during Stress-Relaxation.* J Biomech, 2016. **49**(1): p. 87-93.

70. Vena P, Gastaldi D, Contro R, *A Constituent-Based Model for the Nonlinear Viscoelastic Behavior of Ligaments.* J Bio Eng, 2006. **128**(3): p. 449-457.

71. Baer E, Cassidy J, Hitlner A, *Hierarchical Structure of Collagen Composite Systems: Lessons from Biology.* Pure Appl Chem, 1991. **63**(7): p. 961-973.

72. E, Pena, *Prediction of the Softening and Damage Effects with Permanent Set in Fibrous Biological Materials.* J Mech Phys Solids, 2011. **59**(9): p. 1808-1822.

73. D, Logan, *A First Course in the Finite Element Method*. 5 ed. 2011: CL Engineering.

74. Nam-Ho, Kim, *Introduction to Nonlinear Finite Element Analysis*. 2015.

75. Simulia, Abaqus, *Abaqus Users Subroutines Reference Guide*. 2016.

76. Weiss J, Maker B, Govindjee S, *Finite Element Implementation of Incompressible, Transversely Isotropic Hyperelasticity.* Comput Methods Appl Mech Engrg, 1996. **135**(1-2): p. 107-128.

77. C, Suchocki, *Finite Element Implementation of Slightly Compressible and Incompressible First Invariant-Based Hyperelasticity: Theory, Coding, Exemplary Problems.* J Theor App Mech, 2017. **55**(3): p. 787-800.

78. E, Pena, *Computational Aspects of the Numerical Modelling of Softening, Damage and Permanent Set in Soft Biological Tissues.* Comput Struct, 2014. **130**: p. 57-72.

79. Kiapour A, Kiapour AM, Kaul V, Quatman C, Wordeman S, Hewett T, *Finite Element Model of the Knee for Investigation of Injury Mechanisms: Development and Validation.* J Biomed Eng, 2014. **136**(1): p. 1-14.

80. Smith M, Castile R, Brophy R, Dewan A, Bernholt D, Lake S, *Mechanical properties and Microstructural Collagen Alignment of the Ulnar Collateral Ligament During Dynamic Loading.* J Sports Med, 2018. **47**(1): p. 151-157.

81. Safran M, Ahmad C, Elattrache N, *Ulnar Collateral Ligament of the Elbow.* Arthroscopy, 2005. **21**(11): p. 1381-1395.

82. Labott J, Aibinder W, Dines J, Camp C, *Understanding the Medial Ulnar Collateral Ligament of the Elbow: Review of Native Ligament Anatomy and Function.* World J Orthop, 2018. **9**(6): p. 78-84.

83. Dugas J, Ostrander R, Cain E, Kingsley D, Andrews J, *Anatomy of the Anterior Bundle of the Ulnar Collateral Ligament.* J Shoulder Elbow Surg, 2007. **16**: p. 657-660.

84. Triantafyllidi E, Paschos N, Goussia A, Barkoula N, Exarchos D, Matikas T, Malamou-Mitsi V, Georgoulis A, *The Shape and the Thickness of the Anterior Cruciate Ligament Along its Length in Relation to the Posterior Cruciate Ligament* Arthroscopy, 2013. **29**(12): p. 1963-1973.

85. Timmerman L, Andrews J, *Histology and Arthroscopic Anatomy of the Ulnar Collateral Ligament of the Elbow.* Am J Sports Med, 1993. **22**(5): p. 667-673.

86. Shukla M, Keller R, Marshall N, Ahmed H, Scher C, Moutzouros V, Holsbeeck M, *Ultrasound Evaluation of the Ulnar Collateral Ligament of the Elbow: Which Method is Most Reproducible?* Skeletal Radiol, 2017. **46**: p. 1081-1085.

87. Regan W, Korinek S, Morrey B, *Biomechanical Study of Ligaments Around the Elbow Joint.* Clin Orthop, 1991. **271**: p. 170-179.

88. Matthias F, Salzmann G, Bode G, Pestka J, Kuhle J, Sudkamp N, Niemeyer P, *Posterior Root Tears of the Lateral Meniscus.* Knee Surg Sports Traumatol Arthrosc, 2015. **23**: p. 119-125.

89. Koenig J, Ranawat A, Umans H, DiFelice G, *Meniscal Root Tears: Diagnosis and Treatment.* Arthroscopy, 2009. **25**(9): p. 1025-1032.

90. Brody J, Lin H, Hulstyn M, Tung G, *Lateral Meniscus Root Tear and Meniscus Extrusion with Anterior Cruciate Ligament Tear.* Radiology, 2015. **239**: p. 806-810.

91. Horgan C, Smayda M, *The Importance of the Second Strain Invariant in the Constitutive Modeling of Elastomers and Soft Biomaterials.* Mechanics of Materials, 2012. **51**: p. 43-52.

92. Hau M, Haussmann M, Greives T, Matlack C, Costantini D, Quetting M, Adelman J, Miranda A, Partecke J, *Repeated Stressors in Adulthood Increase the Rate of Biological Aging.* Frontiers in Zoology, 2015. **12**(4): p. 1-10.

93. Ghahfarokhi A, Dianat I, Feizi H, Asghari-Jafarabadi M, *Influence of Gender, Hand Dominance and Arthroscopic Characteristics on Different Types of Pitch Strength: A Partial Least Squares (PLS) Approach* Applied Ergonomics, 2019. **79**: p. 9-16.

94. DosSantos T, Bishop C, Thomas C, Comfort P, Jones P, *The Effect of Limb Dominace on Change of Direction Biomechanics: A Systematic Review of its Importance for Injry Risk.* Physical Therapy in Sport, 2019. **37**: p. 179-189.

95. Lizzio V, Gulledge C, Smith G, Meldau J, Borowsky P, Moutzouros V, Makhni E, *Predictors of Elbow Torque Among Professional Baseball Pitchers.* J Shoulder Elbow Surg, 2020. **29**: p. 316-320.

96. Camp C, Tubbs T, Fleisig G, Dines J, Dines D, Altchek D, Dowling B, *The Relationship Between Throwing Arm Mechanics and Varus Elbow Torque.* Am J Sports Med, 2017. **45**(13): p. 3030-3035.

97. Zec M, Thistlethwaite P, Frank C, Shrive N, *Characterization of the Fatigue Behavior of the Medial Collateral Ligament Utilizing Traditional and Novel Mechanical Variables for the Assessment of Damage Accumulation.* J Bio Eng, 2010. **132**: p. 1-8.

98. Pexa B, Ryan E, Myers J, , *Medial Elbow Joint Space Increases with Valgus Stress and Decreases when Cued to Perform a Maximal Grip Contraction.* Am J Sports Med, 2018. **46**(5): p. 1114-1119.

99. Jildeh T, Okoroha K, Tramer J, Chahla J, Nwachukwu B, Annin S, Moutzouros V, Bush-Joseph C, Verma N, *Effect of Fatigue Protocols on Upper Extremity Neuromuscular Function and Implications for Ulnar Collateral Ligament Injury Prevention.* Orthorp J Sports Med, 2019. **7**(12): p. 1-8.

100. Gilat A, Subramaniam V, *Numerical Methods for Engineers and Scientists*. 3 ed. 2014: John Wiley & Sons Inc.

101. Frangiamore S, Bigart K, Nagle T, Colbrunn R, Millis A, Schickendantz M, *Biomechanical Analysis of Elbow Medial Ulnar Collateral Ligament Tear Location and its Effect on Rotational Stability.* J Shoulder Elbow Surg, 2018. **27**: p. 2068-2076.

102. Hassan S, Parks B, Douoguih W, Osbahr D, *Effect of Distal Ulnar Collateral Ligament Tear Pattern on Contact Forces and Valgus Stability in the Posteromedial Compartment of the Elbow.* Am J Sports Med, 2014. **43**(2): p. 447-452.

103. Lee M, Hyman W, *Modeling of Failure Mode in Knee Ligaments Depending on the Strain Rate.* BMC Musculoskeletal Disorders, 2002. **3**(3).

104. Hariri S, Safran M, *Ulnar Collateral Ligament Injury in the Overhead Athlete.* Clin Sports Med, 2010. **29**: p. 619-644.

105. Kancherla V, Caggiano N, Matullo K, *Elbow Injuries in the Throwing Athlete.* Orthop Clin N Am, 2014. **45**: p. 571-585.

106. Gustas C, Lee K, *Multimodality Imaging of the Painful Elbow.* Radiol Clin N Am, 2016. **54**: p. 817-839.

107. Daruwalla J, Daly C, Seiler III J, *Medial Elbow Injuries in the Throwing Athlete.* Hand Clin, 2017. **33**: p. 47-62.

108. O'Brien D, O'Hagan T, Stewart R, Atanda Jr A, Hammoud S, Cohen S, Ciccotti M, *Outcomes for Ulnar Collateral Ligament Reconstruction: A Retrospective Review Using the KJOC Assessment Score with Two-Year Follow-Up in an Overhead Throwing Athlete.* J Shoulder Elbow Surg, 2015. **24**(6): p. 934-9940.

109. Ugural A, Fenster S, *Advanced Strength and Applied Elasticity*. 4 ed. 2010.

110. Neviaser A, Andarawis-Puri N, Flatow E, *Basic Mechanisms of Tendon Fatigue Damage.* J Shoulder Elbow Surg, 2012. **21**(2): p. 158-163.

111. Cottrell J, Turner J, Arinzeh T, O'Connor J, *The Biology of Bone and Ligament Healing.* Foot Ankle Clin N Am, 2016. **21**(4): p. 739-761.

112. Achari Y, Chin J, Heard B, Rattner J, Shrive N, Frank C, Hart D, *Molecular events surrounding collagen fibril assembly in the early healing rabbit medial collateral ligament—failure to recapitulate normal ligament development.* Connective Tissue Research, 2010. **52**(4): p. 301-312.

113. van der List J, Mintz D, DiFelice G, *The Location of Anterior Cruciate Ligament Tears.* Orthop J Sports Med, 2017. **5**(6): p. 1-9.

114. van der List J, Mintz D, DiFelice G, *The Locations of Anterior Cruciate Ligament Tears in Pediatric and Adolescent Patients: A Magnetic Resonance Study.* J Pediatr Orthop, 2019. **39**(9): p. 441-448.

115. Erickson B, Carr J, Chalmers P, Vellios E, Altcheck D, *Ulnar Collateral Ligament Tear Location May Affect Return-to-Sports Rate but Not Performance Upon Return to Sports After Ulnar Collateral Ligament Reconstruction Surgery in Professional Baseball Players.* Am J Sports Med, 2020. **48**(11): p. 2608-2612.

116. Duenwald S, Vanderby Jr R, Lakes R, *Stress relaxation and recovery in tendon and ligament: Experiment and modeling.* Biorheology, 2010. **47**(1): p. 1-14.

117. Pioletti D, Rakotomanana, *On the independence of time and strain e!ects in the stress relaxation of ligaments and tendons.* J Biomech, 2000. **33**(12): p. 1729-1732.

118. Moon D, Woo S, Takakura Y, Gabriel M, Abramowitch S, *The effects of refreezing on the viscoelastic and tensile properties of ligaments.* J Biomech, 2006. **39**(6): p. 1153-1157.

119. Lee A, Elliott D, *Freezing does not alter multiscale tendon mechanics and damage mechanisms in tension.* Ann N Y Acad Sci, 2018. **1409**(1): p. 85-94.

120. Hrapko M, van Dommelen J, Peters G, Wismans J, *The Influence of Test Conditions on Characterization of the Mechanical Properties of Brain Tissue.* J Bio Eng, 2008. **130**(3).

121. Tuman J, Diduch D, Rubino J, Baumfeld J, Nguyen H, Hart J, *Predictors for Hamstring Graft Diameter in Anterior Cruciate Ligament Reconstruction.* Am J Sports Med, 2007. **35**(11): p. 1945-1949.

122. Moghamis I, Abuodeh Y, Darwiche A, Ibrahim T, Dosari M, Ahmed G, *Anthropometric correlation with hamstring graft size in anterior cruciate ligament reconstruction among males.* Internation Orthopaedics, 2020. **44**: p. 577-584.